Year : 2021

Enhancing monoamine transporters expression in neuroendocrine tumors to improve radionuclide imaging and therapy

Grand-Guillaume-Perrenoud Silvestre Ferreira Joana

UNIL | Université de Lausanne

Faculté de biologie et de médecine

Département

Enhancing monoamine transporters expression in neuroendocrine tumors to improve radionuclide imaging and therapy

Thèse de doctorat ès sciences de la vie (PhD)

présentée à la

Faculté de biologie et de médecine
de l'Université de Lausanne

par

Joana Grand-Guillaume-Perrenoud Silvestre Ferreira

Master en Biochimie pour la santé de l'Université de Lisbonne, Portugal

Jury

Prof. Francis Verdun, Président
Dr. Eric Grouzmann, Directeur de thèse
Dr Karim Abid, Co-directeur
Prof. Margret Schottelius, expert
Prof. Valentina Garibotto, expert
Dr Haithem Chtioui, expert

Lausanne, 2021

Ecole Doctorale

Doctorat ès sciences de la vie

Imprimatur

Vu le rapport présenté par le jury d'examen, composé de

Président·e	Monsieur	Prof.	Francis	**Verdun**
Directeur·trice de thèse	Monsieur	Prof.	Eric	**Grouzmann**
Co-directeur·trice	Monsieur	Dr	Karim	**Abid**
Expert·e·s	Madame	Prof.	Margret	**Schottelius**
	Monsieur	Dr	Haithem	**Chtioui**
	Madame	Prof.	Valentina	**Garibotto**

le Conseil de Faculté autorise l'impression de la thèse de

Madame Joana Grand-Guillaume-Perrenoud Ferreira

Master - Biochemistry For Health, Universidade Nova de Lisboa, Portugal

intitulée

Enhancing monoamine transporters expression in neuroendocrine tumors to improve radionuclide imaging and therapy

Date de l'examen : 1 novembre 2021

Date d'émission de l'imprimatur : Lausanne, le 9 novembre 2021

pour le Doyen
de la Faculté de biologie et de médecine

Prof. Niko GELDNER
Directeur de l'Ecole Doctorale

2021

Enhancing monoamine transporters expression in neuroendocrine tumors to improve radionuclide imaging and therapy

Joana Grand-Guillaume-Perrenoud Silvestre Ferreira

Remerciements

Je souhaite tout d'abord remercier le Dr. Eric Grouzmann de m'avoir donné l'opportunité de travailler au sein de son laboratoire et le Dr. Karim Abid pour sa supervision. Je les remercie tous les deux pour leur confiance, soutien et aide essentiels au développement et aboutissement de ce projet. Je remercie également le Dr. Philippe Eugster pour toute son aide et disponibilité pour la partie analytique.

Je remercie la Prof. Melpomeni Fani, la Dr. Rosalba Mansi et la Prof. Annick Mühlethaler dont la collaboration a permis l'accomplissement de ce projet.

Je tiens également à remercier le Prof. Francis Verdun, la Prof. Margret Schottelius, la Prof. Valentina Garibotto et le Dr. Haithem Chtioui d'avoir accepté de faire partie des membres du jury et aussi pour tous leurs conseils et disponibilités.

Je tiens aussi à remercier mes collègues et anciens collègues, Caroline Seghezzi, Marielle Dunand, Céline Vocat, Catherine Centeno et Baptiste Grund pour tous les bons moments passés ensemble au travail ainsi que tous nos moments de fou rire.
Je remercie également Victor de Gautard et Jonathan Maurer pour leur jovialité, leurs conseils ainsi que nos discussions.
Je souhaite exprimer mon immense gratitude à la Dr. Gemma Reverter Branchat pour toutes nos conversations, ses encouragements, ses conseils ainsi que tout son enseignement à mon égard.

Je remercie de tout mon cœur ma famille, notamment mes parents, ma sœur, mes grands-mamans, qui m'ont toujours beaucoup soutenue tout au long de mes études.

Je tiens également à remercier tous mes amis, avec un merci spécial pour mon amie Raquel Sousa qui m'a toujours soutenue et donnée de la force dans les moments plus compliqués.

Enfin, ma plus grande gratitude va à mon conjoint Miguel, pour ses encouragements, son soutien, sa patience et tout ce qu'il fait pour me soutenir.

Abstract

Pheochromocytoma (PHEO), paraganglioma (PGL) and neuroblastoma (NB) are neoplasms that develop mainly from neuroendocrine cells. These tumors are characterized by an increased production of catecholamines (CATs) such as epinephrine (E), norepinephrine (NE) and dopamine (DA) which are reuptaken through monoamine transporters present on the membrane of chromaffin and tumor cells. Tumor imaging protocol is performed by scintigraphy after injection of a radio-iodinated NE analog, meta-iodobenzylguanidine (mIBG), which is uptaken by neuroendocrine tumors through monoamine transporters. mIBG is believed to be internalized by NE transporters (NET), however, our group and others have observed a lack of correlation between NET protein expression and mIBG internalization. Apart from NET, other transporters may also be involved in mIBG internalization including DA transporters (DAT), organic cation transporters (OCT1-3) and plasma membrane transporters (PMAT).

Throughout this project we had three main aims: 1. Identify which transporters are able to internalize mIBG; 2. Induce pharmacologically the expression of these transporters to improve mIBG internalization and consequently increase imaging resolution and radiotherapy efficiency; 3. Translate *in vivo* the results obtained *in vitro* using ^{123}I-mIBG for imaging and biodistribution studies on IGR-NB8 tumor xenografts mice.

Our *in vitro* studies have shown for the first time that not only NET but also DAT is able to internalize mIBG in HEK-293 cells transfected with hNET and hDAT. Through a screening of a large array of histone deacetylase inhibitors (HDACi) we found that CUDC-907 and sodium-4-P significantly increase mIBG internalization in IGR-NB8. Finally, our *in vivo* studies confirmed our *in vitro* experiments since we observed that CUDC-907 increased ^{123}I-mIBG internalization within the tumor of IGR-NB8 xenografts mice.

To conclude, this project contributed to identify a promising candidate, CUDC-907, for the improvement of mIBG imaging and therapy in NB, through the increase in mIBG internalization demonstrated in our *in vitro and in vivo* experiments. Additionally, our results contributed to better understand the mechanism of mIBG internalization and NET and DAT's roles. However more studies are needed to better understand this mechanism.

Résumé

Le phéochromocytome (PHEO), le paragangliome (PGL) et le neuroblastome (NB) sont des néoplasmes qui se développent principalement à partir de cellules neuroendocrines. Ces tumeurs sont caractérisées par une production accrue de catécholamines (CATs) telles que l'épinéphrine (E), la norépinéphrine (NE) et la dopamine (DA) qui sont réabsorbées par des transporteurs de monoamines présents sur la membrane des cellules chromaffines et tumorales. Le protocole d'imagerie tumorale est réalisé par scintigraphie après injection d'un analogue radio-iodé de la NE, le *meta*-iodobenzylguanidine (mIBG), qui est internalisée par les tumeurs neuroendocrines par l'intermédiaire des transporteurs de monoamines. Le mIBG est décrit comme étant internalisé par les transporteurs de NE (NET), cependant, notre groupe et d'autres ont observé un manque de corrélation entre l'expression de la protéine NET et l'internalisation du mIBG. D'autres transporteurs pourraient également être impliqués dans l'internalisation du mIBG, notamment les transporteurs de DA (DAT), les transporteurs de cations organiques (OCT1-3) et les transporteurs de la membrane plasmique (PMAT).

Tout au long de ce projet, nous avions trois objectifs principaux : 1. Identifier les transporteurs capables d'internaliser le mIBG ; 2. Induire pharmacologiquement l'expression de ces transporteurs pour améliorer l'internalisation du mIBG et par conséquent augmenter la résolution de l'imagerie et l'efficacité de la radiothérapie ; 3. Traduire *in vivo* les résultats obtenus *in vitro* en utilisant le ^{123}I-mIBG pour des études d'imagerie et de biodistribution sur des souris transplantées avec des tumeurs IGR-NB8.

Nos études *in vitro* ont démontré pour la première fois que non seulement NET mais aussi DAT est capable d'internaliser le mIBG dans des cellules HEK-293 transfectées avec hNET et hDAT. Grâce à un *screening* composé de divers HDACi, nous avons observé que le CUDC-907 et le sodium-4-P augmentent significativement l'internalisation du mIBG dans les cellules IGR-NB8. Finalement, nos études *in vivo* confirment nos expériences *in vitro*, vu que nous avons aussi observé que le CUDC-907 augmente l'internalisation du ^{123}I-mIBG dans les xénogreffes de tumeurs IGR-NB8 chez la souris.

En conclusion, ce projet a contribué à identifier un candidat prometteur, le CUDC-907, afin d'améliorer l'imagerie et la thérapie du mIBG dans les NB, grâce à l'augmentation de l'internalisation du mIBG démontrée dans nos expériences *in vitro* et *in vivo*. De plus, nos résultats ont contribué à mieux comprendre le mécanisme d'internalisation du mIBG et les rôles

de NET et DAT dans cette internalisation. Toutefois, d'autres études sont nécessaires pour nous aider à mieux comprendre ce mécanisme.

General contents

Index of Figures

Index of Tables

List of abbreviations

AKT protein kinase B

ALK Anaplastic lymphoma kinase

BCA Bicinchoninic acid

BSA Bovine serum albumin

Ca^{2+} Calcium

CATs Catecholamines

CNS Central nervous system

COMT Catechol-O-methyltransferase

Ct Cycle threshold

CT Computed tomography

DA Dopamine

DAT Dopamine transporter

DBH Dopamine b-hydroxylase

DHPG 3,4-dihydroxyphenylglycol

DMEM Dubbeco's modified Eagle's medium

DMI Desipramine

DMSO Dimethyl sulfoxide

DNA Deoxyribonucleic acid

DNMT DNA methyltransferase

DOPA 3,4-dihydroxyphenylalanine

DOPAC 3,4-dihydroxyphenylacetic acid

DOPET 3,4-dihydroxyphenylglycol

E Epinephrine

EEIF1A1 eukaryotic translation elongation factor 1 alpha 1

FBS Fetal bovine serum

FDG Fluorodeoxyglucose

GAPDH Glyceraldehyde 3-phosphate dehydrogenase

HAT Histone acetyltransferase

HDAC Histone deacetylase

HDACi HDAC inhibitor

HEK293 Human embryonic kidney 293

HIF Hypoxia-inducible factor

HIV Human immunodeficiency virus

HRP Horseradish peroxidase

HVA homovanillic acid

I Iodine

INRGSS International neuroblastoma risk group staging system

INSS International Neuroblastoma staging system

L-AADC L-aromatic amino acid decarboxylase

LC-MS/MS Liquid chromatography-mass spectrometry

LFQ Label-free quantification

MEN Multiple Endocrine Neoplasia

Mg^{2+} Magnesium

mABG *meta*- astatobenzylguanidine

MAOA monoamine oxidase

MHPG 3-methoxy-4-hydroxyphenylglycol

mIBG *meta*-iodobenzylguanidine

MN metanephrine

MNs metanephrines

MRI Magnetic resonance imaging

MT methoxytyramine

mTOR mechanistic target of rapamycin

NB Neuroblastoma

ND Not detected

NE Norepinephrine

NET Norepinephrine transporter

NF1 Neurofibromatosis type 1

NMN normetanephrine

NSS Neurotransmitter sodium symporters

OCT Organic cation transporter

PBS Phosphate buffered saline

PDX patient-derived xenografts

PET Positron emission tomography

PGL Paraganglioma

PHD Prolyl hydroxylase

PHEO Pheochromocytoma

PHOX Paired-like homeoblox

p.i. post injection

PIP3 Phosphatidylinositol-3,4,5-triphosphate

PI3K Phosphatidylinositol 3-kinase

PMAT Plasma membrane transporter

PNMT phenylethanolamine N-methyltransferase

P/S Penicillin/Streptomycin

PTEN Phosphatase and tensin homolog deleted chromosome 10

PVDF Polyvinylidene fluoride

QC Quality control

qRT-PCR quantitative real time-polimerase chain reaction

RET Rearranged during transfection gene

SD Standard deviation

SDH Succinate dehydrogenase

SDS Sodium-dodecyl-sulphate

SERT Serotonin transporter

SLC Solute carrier

Sodium-4-P Sodium-4-phenylbutyrate

SPE Solid-phase extraction

SPECT Single photon emission computed tomography

SULT sulfotransferase

TBP TATA box-binding protein

TBS Tris-buffered saline

TBS-T TBS-Tween 20

TH Tyrosine hydroxylase

TrK Tropomyosin receptor kinases

TSA Trichostatin A

VHL Von-Hippel-Lindau

VMA vanillylmandelic acid

VMAT Vesicular monoamine transporter

Wnt Wingless

5-HT 5-Hydroxytryptamine or serotonin

Introduction

Cancer

Cancer is one of the most important causes of mortality in the world. In 2020, according to estimates, 19.3 million new cancer cases and nearly 10 million cancer deaths were reported in the world. Following the current predictions, by 2040 the amount of new cases is expected to increase nearly by 50% compared to 2020.[1] Cancer research has greatly advanced in the last years that has allowed for a better understanding of the biology behind the processes that lead to tumorigenesis, the transformation of normal cells into tumor cells. This transformation is the result of the accumulation of random somatic mutations that provide a better capability for proliferation and survival of the altered cells. The chance for tumorigenesis to occur is greater when associated with certain risk factors that increase somatic mutation rates, such as radiation in form of ultraviolet light, smoke from tobacco and other chemicals.[2] There exist two main groups of genes that can, through loss-of-function or gain-of-function mutations, initiate tumorigenesis. Oncogenes generally lead to increased cancer cell proliferation and tumor growth while tumor suppressor genes are responsible for limiting cell growth and uncontrolled proliferation.[3] Recently, eight hallmarks for cancer have been established which define the acquired capabilities required for malignant tumor growth and progression (Figure 1).[3]

Figure 1 –Hallmarks of cancer.
Adapted from Hanahan and Weinberg, *Cell*, 2011.[3]

Neuroendocrine tumors

Neuroendocrine tumors are neoplasms originated from the hormone-producing cells of the endocrine and nervous systems. Neuroendocrine tumors can develop in organs such as adrenal glands, gastrointestinal tract, pancreas, lungs and others.[4] In most of the cases, these tumors overproduce and release hormones that can be useful as markers for their detection.

Over this work, we mainly focused on three types of neuroendocrine tumors: pheochromocytoma (PHEO), paraganglioma (PGL) and neuroblastoma (NB). These three types of neuroendocrine tumors arise from chromaffin cells derived from embryonic neural crest. Chromaffin cells are evolutionarily hybrid cells that possess characteristics both from neuronal and endocrine cells. They can be found in the adrenal glands and in the sympathetic nervous system, where neuronal signals are integrated and converted into the production and release of catecholamines (CATs) and other hormones and peptides.[5] PHEO, PGL and NB produce and secrete a large amount of CATs including epinephrine (E), norepinephrine (NE) and dopamine (DA). Upon neuroendocrine stimulation, CATs are released from secretory vesicles and part of these monoamines are reuptaken by chromaffin cells and tumor cells through monoamine transporters.[6]

Pheochromocytoma and paraganglioma

PHEO and PGL are rare types of neuroendocrine tumors with an incidence of 2-8 cases per million.[7] PHEO and PGL have a neural crest origin, the first develop from chromaffin cells in the adrenal medulla (Figure 2) and the later develop from chromaffin cells from extra adrenal location.[8] Both are mostly benign in nature, although approximately 15-20% of the cases develop metastatic disease.[9] These metastasis often develop in lymph nodes, bones, liver and lungs.[9, 10] Due to their high production and secretion of CATs, PHEO and PGL are responsible for a variety of symptoms: very often hypertension but also tachycardia, sudation, headaches, pallor and anxiety. Occasionally, in case of malignancy, other symptoms can appear caused by the metastatic growth of the tumor.[11-13] Diagnosis of PHEO and PGL is performed by analyzing the amount of CATs and especially their metabolites in plasma and in 24 h collected urine.[14] The first line of treatment for PHEO and PGL is usually surgery, however when the tumor is malignant and has already spread through multiple metastasis or it cannot be surgically removed, the options are usually chemotherapy and radiotherapy. PHEO patients with metastasis have a half-life of 50 to 60% at 5 years.[9, 13]

Most of the PHEO and PGL cases are considered sporadic tumors however some mutations in genes like von-Hippel-Lindau (*VHL*), succinate dehydrogenase subunits A, B, C and D (*SDH*),

multiple endocrine neoplasia type 2 (*MEN2*), neurofibromatosis type 1 (*NF1*), hypoxia-inducible factor-2α (*HIF-2α*) among others are responsible for more than 30% of tumors.[9, 12, 15]

VHL is a gene ubiquitously expressed in adult tissues and its protein product (pVHL) is commonly associated with the regulation of hypoxia-induced responses, namely, the ubiquitylation of hypoxia-inducible factor-1α. pVHL is also present in a number of different cellular processes such as cell cycle control and mRNA stability. There exist five different classes of pathologies associated with mutations in pVHL, from truncated protein forms which could cause retinal angiomas to several distinct missense variants which could cause PHEO. These *VHL* pathologies can either be hereditary (accounting for 80% of the cases via autosomal dominant genetics) or sporadic, which occur in cases with a spontaneous genetic alteration of *VHL*. Patients with PHEO caused by *VHL* mutations usually display an earlier beginning of the disease around 19 years of age, although chances of malignancy are reduced.[16, 17]

SDH is a mitochondrial protein complex which plays a role in aerobic respiration in cells. In normal physiological conditions, SDH is composed of four subunits: A, B, C and D that are involved in the Krebs cycle, with the oxidation of succinate in fumarate, and in the electron transfer chain, with the reduction of ubiquinone in ubiquinol.[18] This dual function of SDH underlies its importance in a tumor scenario. On one hand, SDHA mutations can induce necrotizing encephalopathy. On the other hand, SDH mutations on the remaining three subunits are associated with defects in the regulation of HIF and VHL, causing a greater risk of PHEO and PGL. SDH mutations on subunits B, C and D that lead to malfunctioning subunits are believed to lead to an increased accumulation of succinate and a decrease of fumarate in the cell. Some PHEO and PGL cases have already been seen with altered levels of subunits B and D and consequent increases of succinate levels. This then leads to a stabilization of HIF-2α, via the inhibition of its main regulator, prolyl hydroxylase (PHD). The stabilization of HIF then increases the activation of hypoxia-induced genes which increase survivability of tumors in hypoxic conditions.[19] Some studies reported that the appearance of metastasis in 40-50% of PHEO and PGL patients are related to germline mutation on SDH B.[9]

The MEN2 syndrome is associated with mutations in the rearranged during transfection (*RET*) gene which is classified as a proto-oncogene gene. RET mutations result in abnormal cellular proliferation and can lead to the formation of mostly benign PHEO. MEN2 can be further subdivided in two subtypes: MEN2A and MEN2B. MEN2A is the most frequent subtype leading to medullary thyroid carcinoma in nearly 100% of the cases and approximately 50% of cases lead to PHEO. Patients displaying MEN2A usually have higher life expectancies

compared to MEN2B, which is commonly the most aggressive subtype with higher risks of malignancy and is often lethal.[8, 20]

As briefly mentioned, HIF-2α is responsible for the activation of hypoxia-induced genes. In normoxic conditions, HIF-2α is quickly marked by pVHL and PHD and degraded by the proteasome. In that way, the incorrect stabilization of HIF-2α via gain-of-function mutations in the *HIF-2α* gene can lead to the generation of pseudohypoxic PHEO and PGL tumors. However, some studies have shown that there exist several groups of pseudohypoxic tumors and not all of them are related to *HIF-2α* gain of function. Indeed, PHEO and PGL tumors that develop via loss of function mutations in the *VHL* or *PHD* genes often show clinical differences such as neurofibromatosis and multiple neuroendocrine neoplasia 2B. Yet, the common point is the increase in levels of stable HIF-2α, which were found in all kinds of pseudohypoxic PHEO and PGL, and lead to the appearance of polycythemia and/or somatostatinomas, and even ocular abnormalities.[21]

PHEO and PGL hereditary cases were recently subdivided into three categories according to their molecular biology: when the mutated genes are related with oxygen regulation and responses to hypoxia such as the *VHL* and *HIF-1α* genes, they belong to the pseudohypoxia group; when genes such as *CSDE1* and *MAML1* these cases are related to the Wingless (Wnt) pathway, a pathway associated with organogenesis and often tumorigenesis as well; finally if genes such as *NF1*, *RET* and *TMEM127* are altered, these cases belong to the kinase signaling group. This separation of PHEO and PGL cases according to the molecular mechanisms that may lead to them is especially important for more personalized therapies directed towards the specific molecular pathways affected.[7]
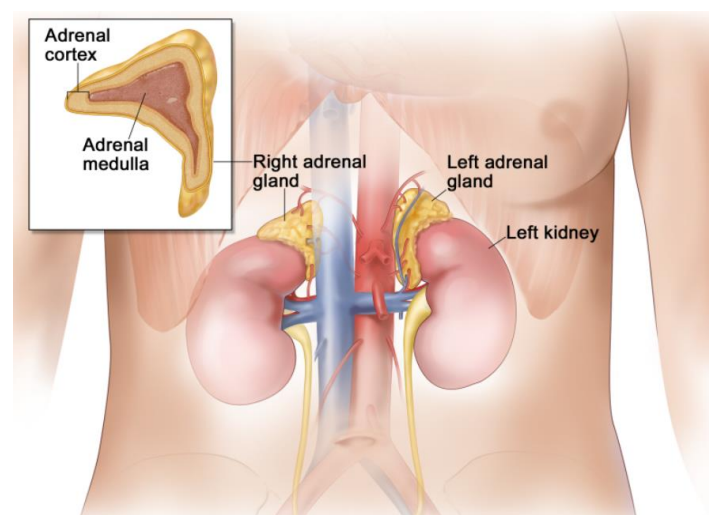
Figure 2 – Illustration of the adrenal glands' anatomical localization and structure.

Neuroblastoma

NB is a solid tumor first described by James Wright in 1910 and it has an embryological origin deriving from the neural crest, making it a sympathetic nervous system tumor. NB is the most common childhood extracranial tumor and has a very aggressive nature due to its high likeliness of appearance of metastasis representing 12% of all pediatric cancer fatalities, however some cases can regress spontaneously.[22-25] NB diagnosis is mainly performed before 5 years old with a better prognosis when it is diagnosed before one year of life. Essentially, NB develops in the sympathetic nervous system, including adrenal glands and sympathetic ganglia.[25, 26] The adrenal gland region is the most common site accounting for approximately 46% of the cases but it can also develop in the neck, thoracic region and pelvis. [22, 24, 26] Many NB patients are asymptomatic but depending on the place it develops, NB can lead to the appearance of different symptoms: when NB develops in the abdominal cavity, it can lead to constipation and painful abdominal distension, and, in some cases, hypertension, when the renal vessels are compressed. When it develops in the thoracic region, for example, NB can lead to cases of scoliosis and compression of the airways. The phenotypic variety found in NB cases further reinforces the idea of heterogeneous backgrounds. [24, 27] At diagnosis, approximately 50% of the NB patients present metastasis, which spread mainly to bone marrow, bone, lymph nodes, and less frequently to liver and skin.[28]

NB can be divided in two groups: familial and sporadic cases. The majority of NB cases is sporadic while 1-2% of total cases, those considered to be familial, are inherited in an autosomal dominant way. Various studies have been made for several decades concerning familial NB cases. Mutations in anaplastic lymphoma kinase (ALK) were found to be associated with 75% of all familial cases. ALK is a receptor tyrosine kinase associated with anaplastic large cell lymphoma and non-small cell lung carcinoma.[22] In malignant cases, such as some NB cases, ALK mutations are usually gain-of-function mutations associated with point mutations, translocation events or replication events. Interestingly, despite being most commonly associated with familial cases, ALK was also found in sporadic cases. In addition to ALK, the paired-like homeoblox 2b (*PHOX2B*) gene was also associated with NB. *PHOX2B* encodes a transcription factor required for the normal formation of the noradrenergic neurons from the neural crest. However, its exact role in diseases and particularly in NB is still uncertain, though 2% of sporadic NB cases have shown mutations in *PHOX2B*. Still, *PHOX2B* may not be the most adequate genetic marker for NB since positivity for mutations in this gene are not always

associated with the formation of tumors.[22] *MYCN* is also a gene which is detected in approximately 20% of the NB patients and is also correlated with high-risk disease.[29] *MYCN* is related to the induction of cellular proliferation as well as cell-cycle progression in quiescent fibroblasts.[25] Some studies have demonstrated that the amplification of *MYCN* in NB patients is correlated with poor prognosis and a metastatic profile. This is due to the involvement of *MYCN* in the adhesion, motility, invasion and degradation of surrounding matrices, characteristics of aggressive tumors. For these reasons, *MYCN* amplification can be used as a biomarker for the determination of risk, which translates into the probability of event-free survival rate.[25, 29]

The risk associated with the NB tumor can help in categorizing the different cases. When there is a 85-90% chance the tumor will respond to therapy and the patient can lead 5 years without events, it is said the tumor is low or intermediate risk. When this chance is lower than 50%, the case is said to be high-risk and when the tumor does not respond to therapy, it is said it is ultra-risk.[25] On the other hand, as mentioned before, NB also has a chance for spontaneous regression due to its genetic heterogeneity. This behavior has been seen in renal carcinoma, melanoma and choriocarcinoma cases, to name a few, though the exact mechanism that leads NB to regress spontaneously is still not well defined. One such pathway is related to the neurotrophins which are elements required for determining the cell fate of neural crest-derived cells. These have been found to be deprived in some regressing NB, including a member of the tropomyosin receptor kinases (Trk), TrkA, which has been associated with favorable outcomes from chemotherapy. Indeed, high levels of TrkA are associated with more tumor cell apoptosis. On the other hand, TrkB, another member of the Trk family, has been associated with unfavorable outcomes. Indeed, when there are high-levels of TrkB and its ligand, the outcome of the therapy is usually worse. This contradiction of responses in the same family has led to issues regarding the definition of Trk's role in NB spontaneous regression (Figure 3a).[23] Another mechanism of spontaneous regression is the loss of telomerase activity. Since telomeres are required for the stability of chromosomes during DNA replication, which happens much more frequently in a tumor situation, the activity of the telomerase is essential for the maintenance of the telomeres and consequently the integrity of the genetic material. Therefore, if the telomerase activity is reduced, the telomeres cannot be regenerated, triggering an apoptotic response that leads to the tumor cell's death, thus leading to the spontaneous regression of the NB tumor (Figure 3b). Additionally, it has been suggested that, in situations of acute infection, the overactivation of the immune system can lead to the generation of anti-tumor immune response. Indeed, the presence of tumor-infiltrating T-cells and antineural

antibodies in some NB patients have been described which might lead to immune-mediated tumor destruction (Figure 3c). Finally, methylation profiles, histone acetylation and chromatin remodeling can also be affected in NB patients leading to altered gene expression and consequently effects on tumor cell survival and/or malignancy (Figure 3d).[23]
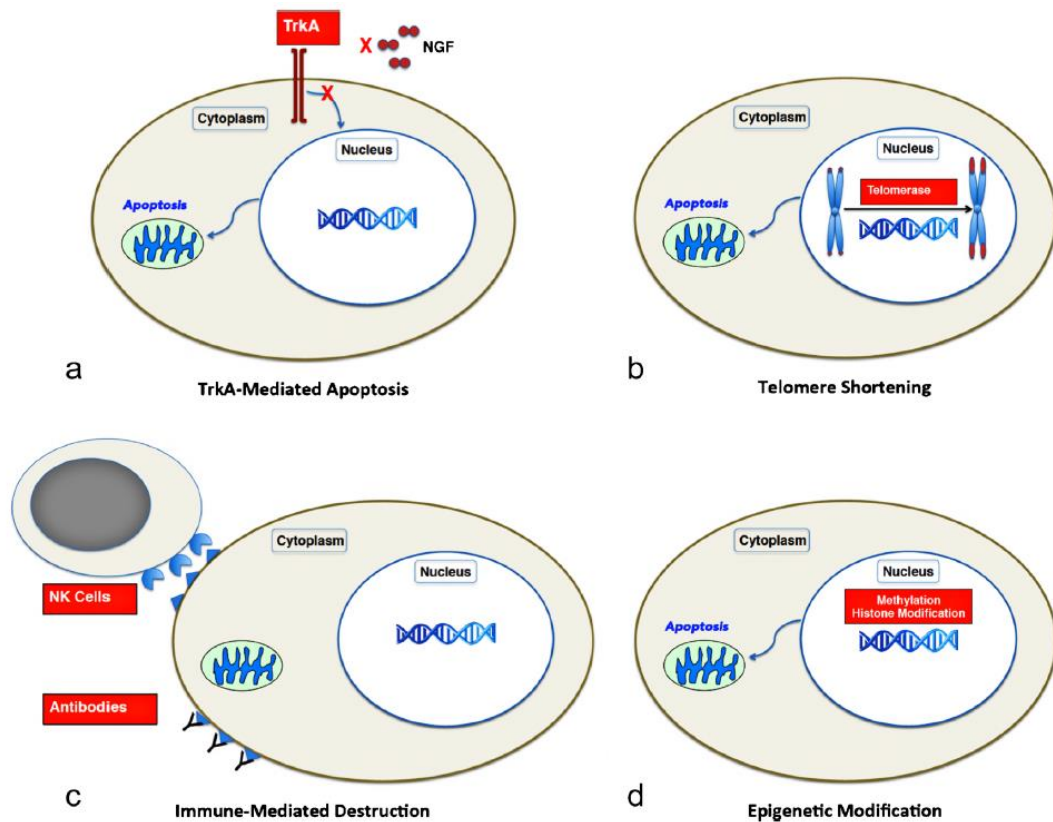
Figure 3 – Illustration of the NB spontaneous regression's mechanisms.
From Brodeur, *Cell Tissue Res.*, 2018.[23]

In 1988 the international NB staging system (INSS) was proposed for the different stages of the disease based on clinical, radiographic and surgical evaluation of the tumor: stage 1, stages 2A and 2B, stage 3, and stages 4 and 4S. NB tumors in stage 1 are restricted to the area of origin, allow for complete resection with or without remaining cancer cells, and present negative ipsilateral and contralateral lymph nodes. Stage 2A are unilateral tumors with incomplete resection and negative ipsilateral and contralateral lymph nodes. Stage 2B tumors are also unilateral tumors which can have complete or incomplete resection and presenting positive ipsilateral and negative contralateral lymph nodes. Stage 3 tumors can infiltrate across the midline with or without regional lymph nodes, but can also be unilateral with positive contralateral lymph nodes, or even midline tumors with positive bilateral regional lymph nodes. Stage 4 tumors present metastasis in distant lymph nodes, bone and bone marrow and also the

liver, among others. Finally, stage 4S patients present a localized primary tumor similar to stages 1, 2A and 2B with metastasis limited to liver, the skin and/or the bone marrow.[30]

In 2009, a new system, the international NB risk group staging system (INRGSS) was proposed for NB tumors for pretreatment classification based on imaging criteria and progression of the disease, as well as the age of the patient at diagnosis (Figure 4). This new system separates NB tumors into 16 risk groups using combinations of prognostic risk factors. In summary, L1 and L2 tumors is defined by localized tumors, M and MS include metastatic disease, being analogous to the above-mentioned stages 4 and 4S in the, respectively. Additional factors include the histological appearance of the tumor, the grade of differentiation, the amplification or not of the *MYCN* gene, 11q chromosomal aberration and the DNA ploidy of the tumor. Generally, the most unfavorable prognosis is reserved for older children presenting spread tumors. Younger patients with localized tumors present a better prognosis with a positive response to treatment and good chances to be cured.[31]

INRG Stage	Age (months)	Histologic Category	Grade of Tumor Differentiation	MYCN	11q Aberration	Ploidy	Pretreatment Risk Group
L1/L2		GN maturing, GNB intermixed					A (very low)
L1		Any, except GN maturing or GNB intermixed		NA			B (very low)
				Amplified			K (high)
L2	< 18	Any, except GN maturing or GNB intermixed		NA	No		D (low)
					Yes		G (intermediate)
	≥ 18	GNB nodular neuroblastoma	Differentiating	NA	No		E (low)
					Yes		H (intermediate)
			Poorly differentiated or undifferentiated	NA			H (intermediate)
				Amplified			N (high)
M	< 18			NA		Hyperdiploid	F (low)
	< 12			NA		Diploid	I (intermediate)
	12 to < 18			NA		Diploid	J (intermediate)
	< 18			Amplified			O (high)
	≥ 18						P (high)
MS	< 18			NA	No		C (very low)
					Yes		Q (high)
				Amplified			R (high)

Abbreviations: GN, ganglioneuroma; GNB, ganglioneuroblastoma; INRG, International Neuroblastoma Risk Group; NA, not amplified.

Figure 4 – International NB Risk Group staging system.
Adapted from Pinto *et al.*, *J. Clin. Oncol.*, 2015.[31]

The choice of NB treatment is dependent on the risk group. When a low risk NB is detected, the first choice of therapy is surgical resection to remove the tumor. Intermediate risk patients are submitted to chemotherapy to reduce the tumor mass and then surgical resection is performed to remove the tumor.[32] For high-risk NB patients, the treatment is divided in three phases: the induction, the consolidation and the maintenance phase. The whole treatment lasts around 18 months, with intensive chemotherapy, radiotherapy, immunotherapy and *cis*-retinoic acid treatment, in addition to surgical resection of the tumor after the first rounds of chemotherapy.[33]

Catecholamine synthesis and metabolism

CATs belong to a class of neurotransmitters and hormones involved in the regulation of many physiological processes and are involved in many diseases such as endocrine, psychiatric and neurological. These organic compounds are composed of an amine group and a benzene ring with two hydroxyl groups called catechol group and are mainly produced in adrenal chromaffin cells and sympathetic nerves (Figure 5).[34, 35]
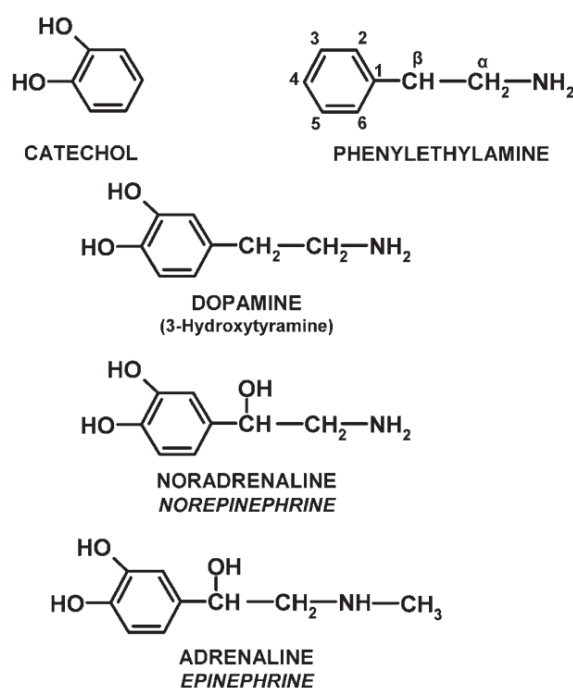
Figure 5 - Illustration of CATs' chemical structure.
From Kvetnansky *et al*., *Physiol. Rev*., 2009.[35]

CATs are known as the main *fight-or-flight* effectors, being responsible for the activation of a number of responses to various forms of stress. Stress is detected by viscero-somatosensors which then stimulate afferent nerves, culminating in the activation of the hypothalamus-pituitary-adrenal axis. Consequently, there is an increase in the production of cortisol in the cortex of the adrenal glands and also the activation of the preganglionic sympathetic neurons. These lead to the production and release of CATs in the synapses of sympathetic ganglia and also the adrenal medulla. At the physiological level, the effects of the activation of the *fight-or-flight* response are varied but include increased blood pressure with increased heart rate, faster breathing, decreased blood flow to the intestines and kidneys. Finally there is also an increase in the production of energy through gluconeogenesis and glycolysis in the liver and in addition increased fat catabolism in the adipocytes.[6]

The amino acid precursor for the synthesis of CATs is L-tyrosine which can be provided from the diet or from the hydroxylation of the amino acid phenylalanine in the liver. Synthesis of CATs is limited by the availability of the enzyme tyrosine hydroxylase (TH), responsible for converting L-tyrosine into 3,4-dihydroxyphenylalanine (DOPA). This enzyme is very abundant in dopaminergic and noradrenergic neurons, the neurons that produce, store and release DA and NE. However, some non-neuronal cells of the gastrointestinal tract and kidneys have also the presence of the enzyme TH. Synthesis of CATs involves several steps (Figure 6) and the first step consists in the conversion of L-tyrosine into DOPA by the enzyme TH. This step occurs in the cytoplasm of the chromaffin cells. L-aromatic amino acid decarboxylase will then convert DOPA to DA, and the latter is then translocated into storage vesicles by the vesicular monoamine transporters (VMAT). DA can then be converted to NE by dopamine β-hydroxylase, an enzyme present in the storage vesicles. Finally, NE is converted to E by the enzyme phenylethanolamine N-methyltransferase (PNMT), this step depends on the presence of PNMT. Therefore, chromaffin cells can be subdivided into noradrenergic and adrenergic cells, depending on the expression of PNMT.[36]
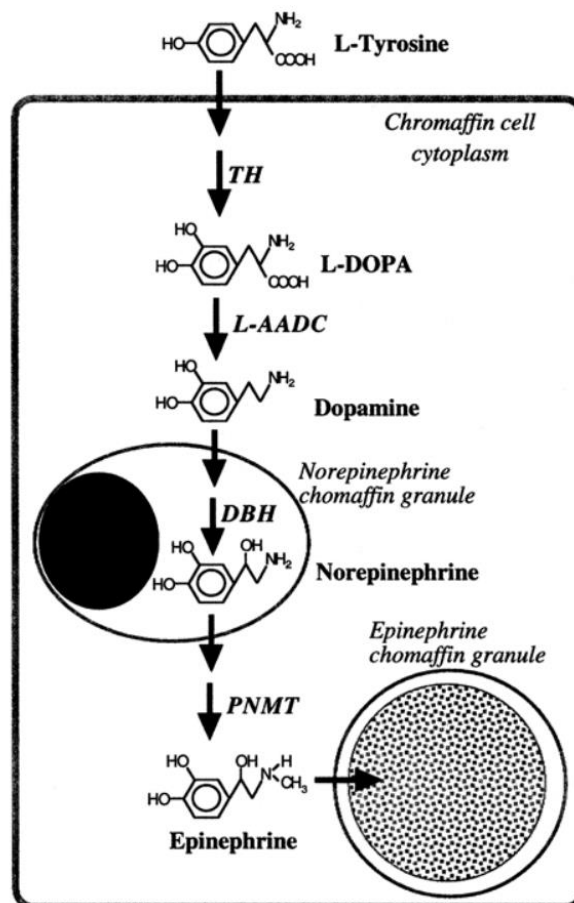
Figure 6 – Illustration of CAT biosynthesis in chromaffin cells.

The metabolism of CATs includes the activity of different enzymes such as monoamine oxidase (MAOA), catechol-O-methyltransferase (COMT) and sulfotransferase (SULT1A3). Following MAOA activity, aldehyde or aldose reductases and alcohol dehydrogenases catalyze the formation of glycol and acid deaminated metabolites, respectively, and finally alcohol dehydrogenases or COMT help the formation of the final catabolites, homovanillic acid (HVA) and vanillylmandelic acid (VMA), depending if the CAT being metabolized is either DA or NE and E, respectively. The metabolism of CATs does not follow a strict pathway and is redundant, therefore different intermediate metabolites can be formed before the final end products (Figure 7).[15, 36] Deamination of DA by MAOA and subsequent metabolization by alcohol dehydrogenases leads to the formation of 3,4-dihydroxyphenylacetic acid (DOPAC). Then, DOPAC is O-methylated by COMT to form HVA. In contrast, deamination of NE and E by the combination of MAOA and aldose or aldehyde reductases leads to the formation of 3,4-dihydroxyphenylglycol (DHPG). Then DHPG is O-methylated by COMT and leads to the formation of 3-methoxy-4-hydroxyphenylglycol (MHPG). Finally, MHPG is metabolized by both alcohol dehydrogenase and aldehyde dehydrogenase to form VMA. Additionally, CAT metabolism can follow alternative intermediate pathways. In the case of DA metabolism, COMT transforms L-DOPA into methoxytyramine (MT). Likewise NE and E are transformed by COMT into normetanephrine (NMN) and metanephrine (MN).[36] These three COMT-catalyzed products of CAT metabolism are known collectively as metanephrines (MNs). MNs can diffuse across the membrane of neuroendocrine cells and enter the bloodstream. HVA, VMA, sulfated and free forms of MNs can be used as markers for neuroendocrine tumor detection, such as NB, PHEO and PGL in urine (HVA and VMA) or plasma samples (MNs).[37-39]

Considering that neuroendocrine tumors arise from dysfunctional neuroendocrine cells it is important to understand the consequences in term of production, storage, release and metabolism of CATs.
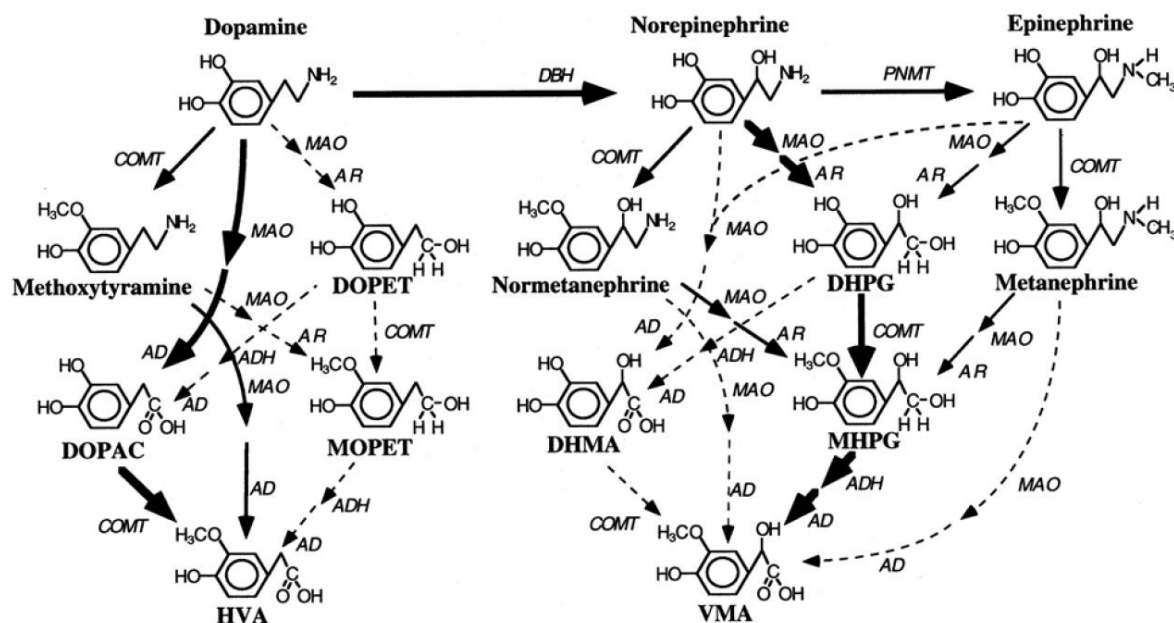
Figure 7 – CAT metabolism pathway.
Abbreviations: 3,4-dihydroxyphenylglycol (DOPET), 3-methoxy-4-hydroxyphenylethanol (MOPET), 3,4-dihydroxymandelic acid (DHMA).
From Eisenhofer *et al.*, *Reviews in Endocrine & Metabolic Disorders*, 2001.[36]

Monoamine transporters

Monoamine transporters belong to the human transporters family of solute carrier 6 (SLC6), which belongs to the neurotransmitter sodium symporters (NSS), a family of transporters that is greatly conserved, ranging from various kingdoms of life, from prokaryotes to human.[40] SLC6 is composed by approximately 350 transporters divided into 55 families. NE transporter (NET), DA transporter (DAT) and serotonin transporter (SERT) are three important members of the SLC6 responsible for the uptake of their respective cargo, namely, NE, DA and serotonin (5-hydroxytryptamine or 5-HT), respectively.[40-42] All three of these transporters are mostly expressed in the central nervous system (CNS) and peripheral nervous system.[41] They mediate the internalization of neurotransmitters from the synaptic cleft through the cotransport of sodium ions alongside the monoamines into the pre-synaptic neuronal terminals. The transport of the monoamines is dependent of their binding to a region of the transporters known as the S1 region. The S1 region is also the binding site for most drugs and psychostimulants specific for these transporters, inhibiting the monoamine transport competitively. Interestingly, the transporters are not exclusively specific to their cognate substrate, which means that, for example, NET is capable of internalizing DA and NE and SERT is also able to uptake DA aside from 5-HT. The therapeutic value of this observation is that a drug whose action is required on most monoamine transporters will likely be specific for not only one of the members of the

SLC6 family.[40] Once internalized into the cytoplasm, the monoamines will be stored in vesicles through the activity of VMATs which is a group of vesicular monoamine transporters part of the SLC18 family that comprise VMAT1 and VMAT2. The flow of small ions is crucial for the transport of monoamines. DAT and NET transport one monoamine alongside two sodium and one chloride ions, while, on the other hand, SERT is able to transport one monoamine alongside one sodium and one chloride ions in exchange for the exit of one potassium ion.[41] As the monoamine transporters mentioned before, VMATs also play an important role in the synaptic homeostasis regulation of NE, DA and 5-HT. The activity of these transporters is essential to release monoamines by exocytosis and to maintain the storage of synaptic monoamines.[42]

Monoamine transporters can be classified into two groups called uptake 1 and uptake 2. Uptake 1 transporters are sodium- and chloride-dependent with a low capacity and high affinity to substrate. This group includes NET, DAT and SERT. Uptake 2 transporters are sodium- and chloride-independent with high capacity but low affinity. This group contains organic cation transporters 1-3 (OCT1-3) and plasma membrane transporters (PMAT).[43, 44]

Monoamines play a part in the activation of neuronal activity which is modulated by the expression of monoamine transporters in the CNS. This makes it clear why the targeting of monoamine transporters is useful to treat certain psychological pathologies such as depression, anxiety and panic disorders. The development of pharmacological drugs specifically targeting NET, DAT and SERT has therefore represented a vast field of investigation for treating a variety of diseases.[41]

NET is localized on the plasma membrane and is required to reuptake NE and also DA into the cytoplasm. NET expression can be found in sympathetic neurons (those called noradrenergic), chromaffin cells in the adrenal medulla, and cells from the lung and the placenta. In peripheral and central sympathetic synapses, NET is essential to limit the time for NE remaining in the synapse, thus regulating its homeostasis. Poor regulation of this homeostasis can lead to dysregulated mood, sleep and alertness due to overactivation of the autonomous system. Additionally, NET can represent targets for various therapeutic drugs (antidepressants) and drugs of abuse (cocaine) which block NET activity thus leading to increased activity of NE in the synapse, although the exact mechanism of action of these drugs is still largely unknown.[45]

NET protein is encoded by the gene *SLC6A2* which is translated into a 69 kDa protein with twelve transmembrane domains, with both the N- and C-termini in the cytoplasm (Figure 8).[46] The expression of the *NET* gene has been extensively studied, which has been shown to present species-specific isoforms occurring after alternative RNA splicing. The bovine homolog

bNET1 is similar to hNET, however bNET2 is not, presenting a different C-terminal region. Similar discoveries were found in the rat brain and PC-12 cells, a rat PHEO cell line, with the cloning of the rNETa variant, homologous to bNET1 and hNET, and an additional variant, rNETb, which presented no homology in the C-terminal region.[47] The human *NET* gene can also produce splice variants, with major differences in the C-terminal region.[48] Regarding the mechanism of action, as mentioned before, NET monoamine transporter is dependent on sodium and chloride levels inside the cell, which have been shown to be crucial for substrate-binding. Therefore the use of drugs such as cyanide or ouabain that block the activity of transporters like NaK-ATPase, which maintain sodium and ATP levels inside the cell, can result in a decrease in the uptake of NE from the decreased activity of NET. Likewise, desipramine (DMI) also inhibits NET activity by binding to the substrate recognition site and possibly by interacting with another Na-dependent site of the transporter.[48, 49] Post-translational modifications are also important for the regulation of NET, such as glycosylation which is required for its localization to the membrane. Poor or incomplete glycosylation has been shown to lead to NET to remain in the cytoplasm. Additionally, the N- and the C-termini, as well as some intracellular loops, can be phosphorylated by protein kinase A, protein kinase C and also calcium (Ca^{2+})/calmodulin-dependent protein kinase II. These phosphorylation sites regulate the transporter's activity.[48]
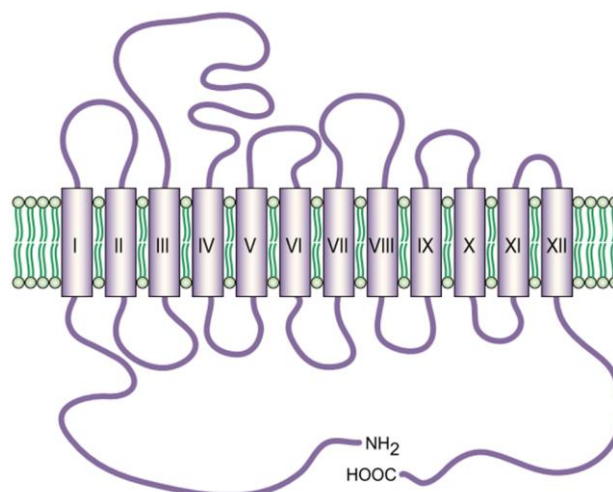
Figure 8 – Topology of the monoamine transporters NET.
From Torres *et al*., *Nat Rev Neurosci*, 2003.[46]

DAT is responsible for the homeostasis of DA. This homeostasis is found dysregulated in many disorders such as depression, Parkinson's disease and schizophrenia.[50] DAT expression is not ubiquitous, being localized in dopaminergic neurons in the CNS. The levels of DAT expression

20

can show variations depending on intensity of DA signaling and also in the case of disease such as human immunodeficiency virus (HIV) -associated dementia and the use of drugs such as cocaine and amphetamines.[51] The DAT gene, *DAT1*, produce no detectable splice variants and the protein coding region is highly conserved among species, although the homology between *DAT* loci of different species is not conserved. Regarding the genetic variation several single nucleotide polymorphisms and mutations has been detected which are related with disorders such as attention deficit hyperactivity disorder.[51] This transporter is termed SLC6A3 and is composed by twelve transmembrane domains including six extracellular loops and five intracellular loops and its molecular weight is nearly 80 kDa (Figure 9). Both N- and C-termini are localized in the cytoplasm for uptake regulation and substrate recognition. Additionally DAT displays multiple phosphorylation sites essential for a stable membrane expression and also for the maintenance of transport efficiency.[51] When DA is released to the synaptic cleft following an increase in intracellular calcium levels, DAT takes advantage of ionic gradients to reuptake DA for processing by VMAT2 into secretory vesicles. This ends neurotransmission and DA can be either degraded into DOPAC or MT or reused for another later release.[36, 52, 53] DAT allows the transport of DA through the cotransport of two sodium and one chloride ions and this mechanism is maintained by NaK-ATPase pumps which actively expel sodium into the extracellular space. This transporter does not exclusively import DA, it can also uptake NE.[51]
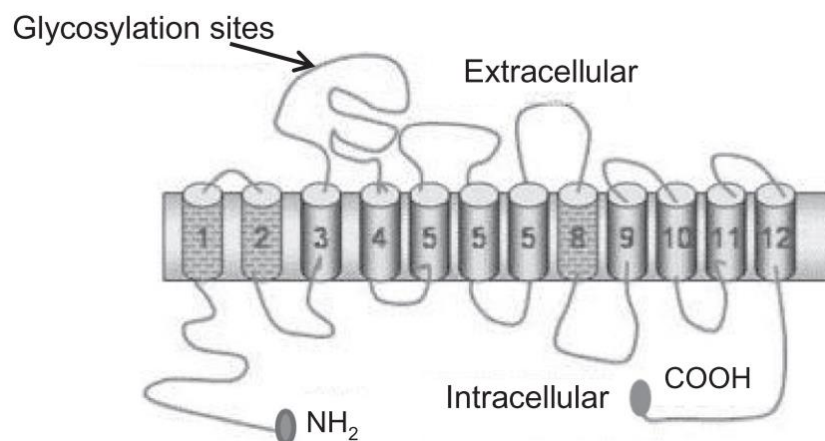
Figure 9 - Topology of the monoamine transporters DAT.
From McHugh *et al.*, *Vitam. Horm.*, 2015.[51]

OCTs, also named extraneuronal monoamine transporters, are polyspecific organic cation transporters due to the variety of different structural substrates that they are able to transport.

OCT is composed by 3 subtypes, OCT1, OCT2 and OCT3 also known as SLC22A1-3, which have different organ distribution and can also have different homologs in different species. In humans, OCT1 can be found in the liver and enterocytes, OCT2 is mainly expressed in kidney but also in the CNS and finally OCT3 is the most widely expressed subtype being expressed in the liver, CNS, heart, kidney, adrenal glands, among others.[54, 55] The genes encoding the proteins OCT1-3 are predicted to form a 12 transmembrane domain-containing protein with intracellular N- and C-termini regions, along with a glycosylation site on the extracellular loop between domains two and three, and phosphorylation sites between domains six and seven (Figure 10).[56] All three subtypes present varying specificity for the transport of monoamines such as DA, NE and E. OCT1 has a higher specificity for DA and E, OCT2 for DA and OCT3 for E.[55] It is suggested that OCTs are the main extraneuronal transporters responsible for reuptaking CATs that have not been uptaken by NET and DAT (uptake 1). At least four splice variants have been described for OCT1, none of them showing significant functional differences in activity in human embryonic kidney 293 (HEK293)-transfected cells. For OCT2, one alternative splice variant has been described, which lacks the last three C-terminal transmembrane domains. Contrarily to the OCT1 variants mentioned, the hOCT2-A splice variant displayed altered transport activity of some but not all compounds. Another issue to take into account are the genetic variations in OCT genes, which present high variability from one individual to another and a great number of polymorphisms that can even lead to amino acid substitutions.[57]
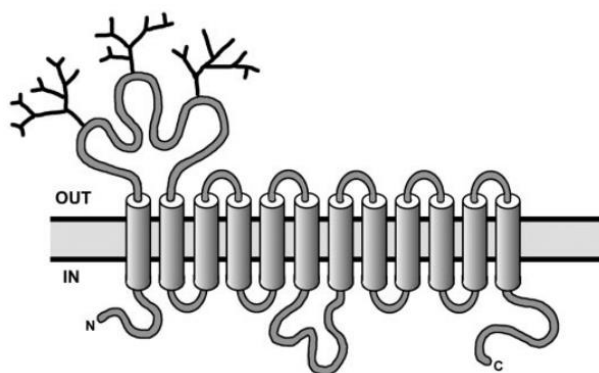
Figure 10 - Topology of the OCT 1.
From Jonker, *J. Pharmacol. Exp. Ther.*, 2004.[57]

PMAT is considered a polyspecific organic cation transporter due to the variety of biogenic amines and xenobiotic cations that it is able to transport. This transporter, also named ENT4, belongs to the fourth member of the mammalian solute carrier 29 (*SLC29A4*) gene family.

PMAT is able to transport some monoamine neurotransmitters like 5-HT and DA but also some organic cations (metformin and 1-methyl-4-phenylpyridinium). As the name suggests this transporter is located on the plasma membrane of the cell and its length is about 530 amino acids and its molecular mass about 58kDa. PMAT has a long intracellular N-terminal region and a short extracellular C-terminal region and, contrarily to the other monoamine transporters described above, PMAT presents 11 transmembrane domains (Figure 11). It is reported to be mainly expressed in neuronal cells in the brain but also in sympathetically innervated peripheral tissues such as the heart, intestine and kidney. PMAT shares most of its organic cation substrates with OCTs, although the transport kinetics between the two groups is variable.[43, 58] As described above, PHEO, PGL and NB are characterized by a production and secretion of large amounts of CATs, which are uptaken again through the monoamine transporters. Therefore, the modulation of monoamine transporter activity may prove essential to define new strategies towards the diagnosis and treatment of neuroendocrine tumors.
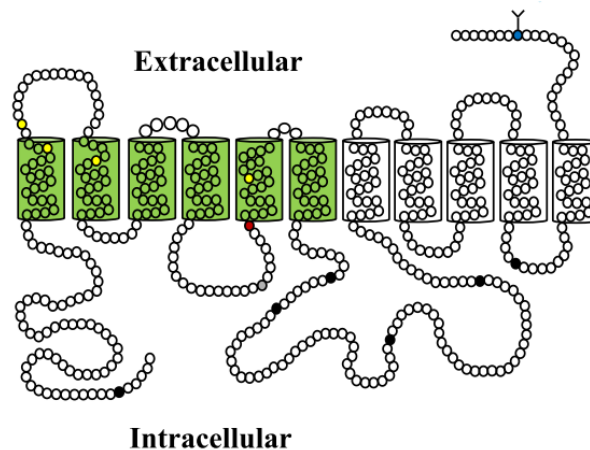
Figure 11 - Topology of the PMAT.
From Wang, *Clin. Pharmacol. Ther.*, 2016.[58]

Neuroendocrine tumors diagnosis and therapy

Neuroendocrine tumors present several particularities compared to other types of cancers: some patients often present non-cancer-specific symptoms, making early diagnosis hard to be established, or the tumor itself is too small to be correctly identified and localized using anatomic imaging techniques such as computed tomography (CT) and magnetic resonance imaging (MRI). Additionally, a subset of well-differentiated tumors do no present high glucose metabolism and therefore the use of fluorodeoxyglucose (FDG) through positron emission tomography (PET) for detection is unviable.[59] In the last decades, complementary therapies to chemotherapy and radiotherapy have been developed for the improved detection and

management of neuroendocrine tumors. One of those consists in molecular imaging therapies with the use of radiolabeled somatostatin analogs, such as octreotide coupled with radioactive indium 111, for diagnosis and imaging of neuroendocrine tumors. However, octreotide-based diagnosis has the disadvantages of providing poor image quality while exposing patients to relatively high radiation doses. Since octreotide was first used in 1989, other radiolabeled analogs were developed such as *meta*-iodobenzylguanidine (mIBG), mainly used in PHEO, PGL and NB tumors, and a number of other somatostatin analogs such as DOTATATE and DOTATOC, which provide a more advantageous therapy for patients compared to octreotide therapy.[60]

mIBG imaging and therapy

mIBG was developed by Wieland and colleagues in 1970 for imaging of the adrenal medulla. This molecule is a NE analog composed by a benzyl and a guanidine group (Figure 12 A). Due to its structural similarity to NE (Figure 12 B), mIBG can be uptaken by healthy sympathetic innervated tissues but to a lesser extent when compared to neuroendocrine tumors such as PHEO, PGL and NB. Initially, mIBG was established for imaging of adrenal medullary tissue, including PHEO, and later was extended to other tumors such as NB. The use of mIBG for NB imaging was shown to be very promising with over 90% of NB presenting visible mIBG internalization.[61] Two mechanisms have been proposed for mIBG internalization: the active, which takes place in cells that express NET, which is ATP-dependent, and occurs in tissues with sympathetic innervation, and the passive diffusion which is non-specific and ATP-independent, occurring in all cells. Once internalized, mIBG is stored in neurosecretory granules via VMAT 1 and 2. However, other studies have also shown that in NB mIBG can be stored in the cytoplasm and in mitochondria, since these cells display less secretory vesicles.[49, 62-64] mIBG can be labelled with different radioactive isotopes of iodine (I), either ^{123}I, for imaging, with emission of γ-radiation, or ^{131}I, with emission of both β- and γ-radiation, used for both imaging and radiotherapy of neuroendocrine tumors. This iodination takes place in the *meta* position of the benzyl ring making mIBG a very stable molecule resistant to the *in vivo* metabolism. In humans, the excretion of mIBG is mainly performed through kidneys, and, due to its stability, approximately 90% of the mIBG excreted in the urine is not metabolized. This mIBG excretion starts in the first 24 h but the majority is excreted within 96 h.[9, 63, 64] Both I isotopes, ^{123}I and ^{131}I, emit γ-radiation, which can be captured by a scintillation camera, also called gamma camera. Half-life of ^{123}I and ^{131}I are around 13 h and around 8 days, respectively.[9, 62] These two I isotopes when labelled with mIBG are used in different situations

depending on the purpose. For diagnosis, ^{123}I-mIBG is preferable due to its shorter half-life, lack of β-emission, and also it allows better imaging resolution and greater sensitivity.[9, 65] In NB cases, ^{123}I-mIBG allows for the effective detection of more than 90% of cases.[61] In PHEO and PGL cases, the sensitivity and specificity of ^{123}I-mIBG imaging is above 80%.[66] On the other hand, ^{131}I-mIBG is preferably used for therapy due to its longer half-life allowing a longer period of β-particle radioactive emission with cytotoxic effects.[9, 65] A number of different studies have been performed regarding the different uses of ^{131}I-mIBG. When used as the main therapeutic option, a mean response rate of around 36-38% was found in high-risk relapsed and refractory NB cases.[61] When multiple treatments of ^{131}I-mIBG are performed in refractory and relapsed NB, response rates of a maximum of 39% were reported.[61] ^{131}I-mIBG can also be used in combination therapies and also with autologous stem cell transplant, however the response rates were not as favorable with only around 10% of the cases tested responding to therapy.[61] Finally, ^{131}I-mIBG has also been reported in induction therapy, with some studies reporting up to 57% of overall response rate when ^{131}I-mIBG is used before subsequent chemotherapy and surgery.[61] In PHEO cases, ^{131}I-mIBG has been reported to be used in single or repeated therapy with objective response rates which varied from 0 to 63%, meaning that 0 to 63% of the patients responded, partially or completely, to the treatment.[65]

 mIBG imaging or therapy is initiated via slow intravenous injection of ^{131}I-mIBG or ^{123}I-mIBG, to avoid side-effects such as tachycardia and hypertensive crisis. Depending on the radioactive isotope used, the imaging is performed 24 h after ^{123}I-mIBG injection and 24 to 48 h after ^{131}I-mIBG injection. Additionally, due to the possibility of the occurrence of free radioiodine in the preparation or later released *in vivo*, the use of thyroid blockers is needed through the use of compounds such as potassium iodide, to prevent excess accumulation of radioactivity in the thyroid. Also, some drugs can interfere with mIBG internalization/retention such as anti-psychotics but also drugs of abuse like cocaine, among others, and their use should be stopped before mIBG imaging/therapy, to avoid possible false-negatives. Additionally, food containing vanillin and CATs as well as chocolate and blue-veined cheese must not be consumed to avoid interference with mIBG internalization.[63, 64] The most frequent toxicity-associated effects of mIBG administration can be seen within two or three days and signs of it include anorexia, nausea and vomiting, though severe acute toxicities are rare. The most serious side-effect is mIBG dose-dependent hematological toxicity, which appears a few weeks after mIBG administration and is most frequent in patients with bone marrow metastasis and patients who received higher doses of radiation. The major side-effect occurring at later stages following mIBG administration is hypothyroidism, regardless of the use of the potassium iodine to block

the thyroid.[67] More recently, a new positron emitting mIBG tracer was produced with a ^{124}I isotope radioactive labeling that provides a greater spatial resolution compared to the two other compounds mentioned. This tracer has a longer half-life of 4.2 days and can be used to allow for better and more appropriate dosage of ^{131}I-mIBG.[64] An additional tracer has also been designed recently for the treatment of neural crest tumors using ^{211}At *meta*-astatobenzylguanidine (mABG) in a PC-12 mouse PHEO model. This tracer has the particularity of emitting α-particles for increased cytotoxicity in a limited range of less than 100μm due to its high linear energy transfer. In addition, there have been no reports of severe side-effects of mABG therapy like weight loss and reduction of the number of myeloid cells in the bone marrow. However, this new tracer is still very recent and more research is required in a human tumor context.[64, 68]
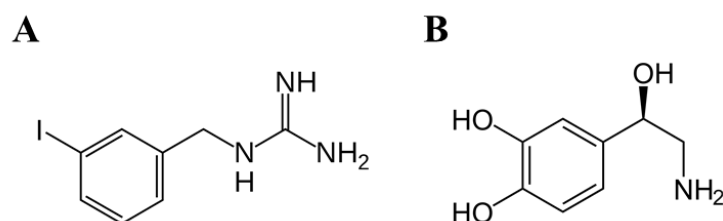
Figure 12 – Molecular structure of mIBG (A) compared to its biological analog, NE (B).

Pharmacological targeting of monoamine transporters to increase mIBG internalization

Since mIBG is a NE analog that is internalized by monoamine transporters present on the surface of neuroendocrine tumors, the pharmacological stimulation of the expression of these transporters could improve the existing imaging/therapy.[69] This pharmacological stimulation could be achieved via the use of different families of drugs, such as histone deacetylase (HDAC) inhibitors and DNA methyltransferase (DNMT) inhibitors against tumors such as PHEO, PGL and NB.[69, 70]

Histone deacetylase inhibitors and DNA methylation inhibitors

Epigenetics, such as histone acetylation and DNA methylation, represent reversible alterations of gene expression without permanent changes in single nucleotides. These reversible changes are regulated by specific enzymes, such as histone acetyltransferases (HAT) and HDAC responsible for histone acetylation and deacetylation, respectively (Figure 13).[71, 72]

Histones are central DNA scaffolding proteins, which regulate the conformation of the chromatin and consequently the accessibility of the DNA transcription machinery. Histones can be post-translationally modified to modulate the chromatin ultrastructure and therefore promote or repress DNA transcription. Typically, histones display a positive charge which makes these proteins interact with DNA and thus make transcription less probable. Histone acetylation on lysine residues by HAT allows for the neutralization of the positive charge which in turn leads to the "opening" of the chromatin, making it more accessible for gene transcription.[73, 74] On the other hand, HDAC are responsible for the removal of acetyl groups bound to histones in the chromatin. This deacetylation reduces spatial constraints that keep the chromatin uncoiled, and thus more accessible for transcription and replication machinery. In this way, HDAC are responsible for making the chromatin more coiled upon itself, inhibiting specific gene expression in certain regions. In humans, HDAC are composed by four classes of 18 enzymes classified according to their homology when compared to the yeast homologs.[74, 75] HDAC expression is not ubiquitous. Class I HDAC (HDAC 1-3 and 8) are mostly nuclear and ubiquitously expressed, class IIa (HDAC 4, 5, 7 and 9), IIb (HDAC 6 and 8) and class IV (HDAC11) HDAC are usually found shuttling between the cytoplasm and the nucleus and have been shown to have tissue-specific expression.[74-76] Additionally, HDAC can also interact with substrates other than histones such as tubulin, regulating cell migration.[76]
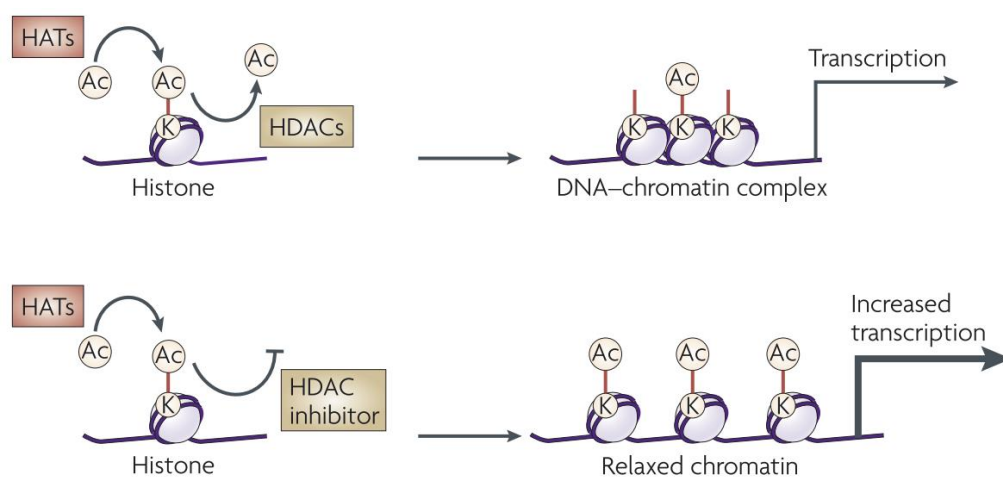
Figure 13 – HDACi effects on chromatin structure and transcription.
From Kazantsev *et al.*, *Nat Rev Drug Discov.,* 2008.[72]

HDACi (HDAC inhibitors) such as vorinostat, valproate acid, trichostatin A (TSA) and sodium-phenylbutyrate (sodium-4-P) have been found to pharmacologically induce the expression of monoamine transporters.[69, 77, 78] This makes HDACi a promising group of drugs for improvement of mIBG therapy/imaging through the increase of the expression of monoamine

transporters. On table 1 we list a number of different HDACi used in this study, their respective HDAC target(s) and the clinical trial phase and the related disease.

Table 1 – Selected HDACi and their targets. (https://clinicaltrials.gov)

HDACi	Target(s)	Clinical trial	Related disease
ACY-1215	HDAC 1, HDAC 2, HDAC 3, HDAC 6, HDAC 8	Phase I/Phase II	Lymphoma
CUDC-101	HDAC, HDAC 1, HDAC 2, HDAC 3, HDAC 4, HDAC 5, HDAC 6, HDAC 7, HDAC 8, HDAC 9, HDAC 10, EGFR, HER2	Phase I	Head and neck cancer
CUDC-907	HDAC 1, HDAC 2, HDAC 3, HDAC 6, HDAC 10, HDAC 11, PI3Kα, PI3Kδ, PI3Kβ	Phase I/Phase II	Lymphoma
Entinostat	HDAC 1, HDAC 3	Phase I/Phase II	Advanced solid tumors/pancreatic cancer
LMK-235	HDAC 4, HDAC 5	-	-
Mocetinostat	HDAC 1, HDAC 2, HDAC 3, HDAC 11	Phase I/Phase II	Advanced or metastatic solid tumor and non-small cell lung cancer
PCI-24781	HDAC 1, HDAC 2, HDAC 3, HDAC 6, HDAC 8, HDAC 10	Phase I/Phase II	Lymphoma/Hodgkin disease
Quisinostat	HDAC 1, HDAC 2, HDAC 3, HDAC 4, HDAC 5, HDAC 8, HDAC 10, HDAC 11	Phase I/Phase II	Advanced solid tumor/ovarian cancer
Romidepsin	HDAC 1, HDAC 2	Phase I/Phase II	Lymphoma, T-cell malignancies

Sodium-4-P	Class I, II and IV HDAC	Phase I/Phase II	Spinal muscular atrophy
Tacedinaline	HDAC 1, HDAC 2, HDAC 3, HDAC 8	Phase II/Phase III	Multiple myeloma/lung cancer
TSA	Class I, II and IV HDAC	Phase I	Relapsed or refractory hematologic malignancies
Tubacin	HDAC 6	-	-
Tucidinostat	HDAC 1,HDAC 2, HDAC 3, HDAC 10	Phase II/Phase III	Breast cancer/lymphoma
Valproic acid	Class I HDAC, GABA receptor, autophagy	Phase I/Phase II	Hemorrhagic shock/breast cancer
Vorinostat	HDAC 1,HDAC 2, HDAC 3, HDAC 6	Phase I/Phase II/Phase III	Sarcoma, Wilms tumor, NB, hepatoblastoma, germ cell tumor/non-small cell lung cancer

DNA methyltransferase inhibitors

DNA methylation is the best described epigenetic phenomenon. In the DNA sequence there exist regions with CpG dinucleotides where DNMT enzymes can bind a methyl group to the pyrimidine ring of cytosine. CpG islands are mainly located near or in the promoter regions and, upon methylation, these regions can no longer be recognized by transcription machinery and therefore gene expression is repressed.[79] DNMT members include DNMT1, DNMT3A, DNMT3B and DNMT3L, where DNMT1 is responsible for the maintenance of the methyltransferase activity, and DNMT3A and DNMT3B are responsible for *de novo* methylation of DNA.[80] Aberrant methylation patterns (hypermethylation and hypomethylation) can also indicate pathologies such as oncogenesis. On one hand, hypomethylation can lead to genomic instability especially in generally hypermethylated regions such as the centromere of chromosomes and on the other hand hypermethylation of promoter regions of tumor suppressor genes can promote the development of tumors.[79] Therefore abnormal activity of DNMT enzymes can promote oncogenesis. The inhibition of DNMT through the use of DNMT inhibitors is then attractive from a clinical point of view for cancer treatment. Inhibitors like decitabine and azacitidine have been shown to increase somatostatin receptor protein expression and thus improve internalization of ^{68}Ga-DOTATOC in human pancreatic neuroendocrine tumor cells (BON-1 cells).[81] Also *N*-phthalyl-L-

tryptophan (RG108) treatment of human NB cells (SK-N-AS cell line) increases DAT mRNA and protein expression through a possible inhibition of DNMT1.[70]

PTEN/PI3K/mTORC1 inhibitors

Another commonly dysregulated pathway in cancer which is well known is the PTEN/PI3K/AKT pathway. In brief, the phosphatase and tensin homolog deleted on chromosome 10 (PTEN) targets phosphatidylinositol-3,4,5-triphosphate (PIP3), which is in turn phosphorylated by the phosphatidylinositol 3 kinase (PI3K). The accumulation of PIP3 leads to the activation of the downstream members of the pathway, including protein kinase B (AKT), a serine-threonine kinase, which promote a number of different responses such as the regulation of cell survival, through inhibition of apoptosis, metabolism and cell cycle, among others (Figure 14). In addition, this pathway also regulates the mechanistic target of rapamycin (mTOR), a serine-threonine kinase, which is indirectly activated by AKT via the inhibition of TSC2. mTOR is essential for regulating translation initiation and the biogenesis of ribosomes.[82] mTOR is found forming two different complexes in mammalian cells: mTOR complex 1 (mTORC1) and mTOR complex 2 (mTORC2). These two complexes show differences in their sensitivity to rapamycin (mTORC1 is more sensitive than mTORC2), the proteins that form the mTOR complex itself are different, the downstream substrates that are phosphorylated by each complex, and consequently the cellular processes that each of the complexes regulates are distinct. mTORC1 is responsible for regulating protein translation and cell growth, while mTORC2 is responsible for cell survival and cytoskeleton rearrangement.[83] In various cancer situations, the PTEN/PI3K/AKT pathway is altered. For example, in a number of familial cancer predisposition syndromes, PTEN activity is lost via mutations, deletions or methylation of the promoter region, leading to overactivation of this pathway. Some PI3K mutations that increase its catalytic activity have also been shown to be implicated in oncogenesis through uncontrolled and constitutive AKT activation, leading to consequent activation of many of the pathway's target genes. [82] Finally, mTOR activity can also be aberrant in tumor cells. A recent study has reported that mTOR is overactivated in more than 70% of cancers, either through mutations that silence tumor suppressor genes, leading to uncontrolled regulation of mTOR activity, or through gain of function mutations in oncogenes that increase mTOR activity.[83]
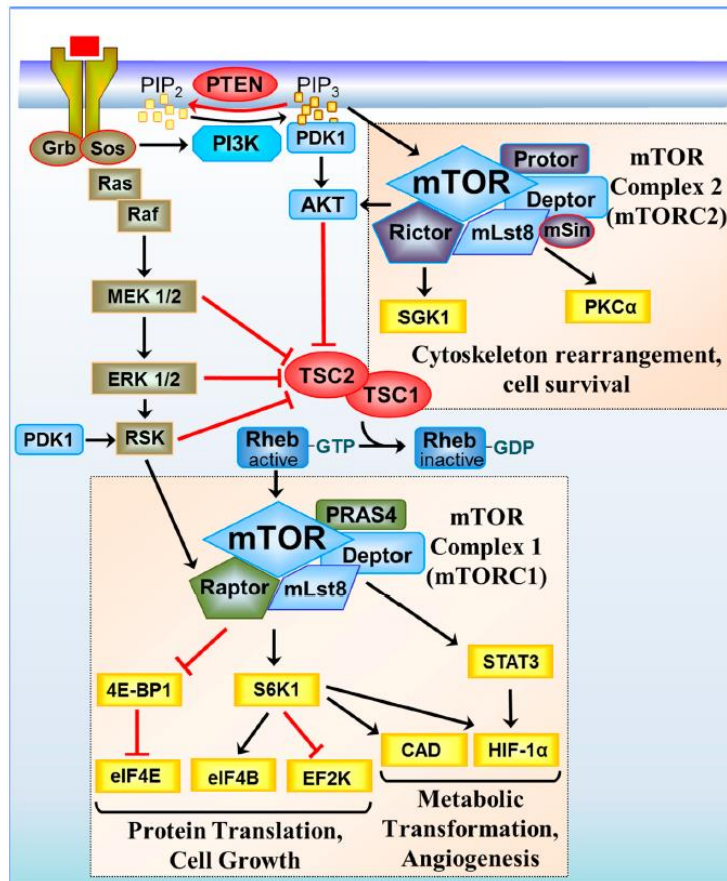
Figure 14 - General pathway of PTEN/PI3K/mTOR.
From Rad *et al.*, *Cancers*, 2018.[83]

Some groups have already started exploring the use of PI3K/AKT/mTOR inhibitors for the treatment of neuroendocrine tumors. VS-5584, a PI3K/mTOR dual inhibitor has been shown to have antitumor effects in NB, both *in vitro* and *in vivo*, via the simultaneous suppression of PI3K and mTORC1 and mTORC2.[84] Rapamycin has also been shown to inhibit proliferation and induces autophagy in NB cells *in vitro*. When used in combination with other inhibitors, such as MK2206, an AKT inhibitor, there is an induction of autophagy but also necroptosis through the simultaneous inhibition of mTOR and AKT *in vitro* and *in vivo*.[85, 86] BGT226 is also a PI3K inhibitor which has already been tested in Phase I/ Phase II clinical trials with patients with advanced solid tumors, such as breast, prostate, colon and bone tumors, among others.[87]

Aims

As mentioned before, mIBG labelled with ^{123}I and ^{131}I is used for therapy and/or imaging in the field of neuroendocrine tumors such as NB, PHEO and PGL. The main goal of this project is to improve treatment and imaging modalities by increasing mIBG internalization into these tumors cells.

Nowadays, mIBG is believed to be internalized exclusively by NET, however, our group and others have observed a lack of correlation between mIBG-positive internalization and NET protein expression in PHEO biopsies from patients. This observation was the starting point of this project. We hypothesized that other monoamine transporters can also be involved in mIBG internalization.

The specific aims of this main project were to:

- Identify which membrane transporters are involved in mIBG internalization.
- Pharmacologically induce the expression of the membrane transporters *in vitro* in order to increase mIBG internalization.
- "Translate" *in vivo* the results obtained *in vitro* using mIBG labelled with ^{123}I for imaging and biodistribution studies on xenograft mice model.

This main project is conducted in a collaboration with Prof. Fani (Division of Radiopharmaceutical Chemistry, University Hospital Basel) for the *in vivo* experiments.

A secondary project was performed with the group of Dr. Annick Mühlethaler who conducted all the *in vivo* experiments (Pediatric Hematology-Oncology Unit, Lausanne University Hospital and University of Lausanne, Switzerland).

The aim of the subproject was to establish, characterize and validate a murine NB xenograft model model to study the metabolism of CATs in NB. This mice model will allow us to mimic and study NB from patients.

Results

Part I

Enhancing monoamine transporters expression in neuroendocrine tumors to improve radionuclide imaging and therapy

Materials and methods

Cell culture and treatments

Along this project two main cell lines were used: HEK293 and IGR-NB8, a NB cell line. HEK293 cells stably transfected with plasmids encoding the human NET and DAT were kindly offered by Prof. M. Reith of the University of New York and HEK293 cells expressing OCT-1, OCT-2, OCT-3 and PMAT by Prof. J. Wang of the University of Washington. IGR-NB8 cells were kindly provided by Dr A. Mühlethaler-Mottet of the Centre Hospitalier Universitaire Vaudois. The IGR-NB8 cell line is derived from an abdominal stage 3 NB of a human xenotransplant.[88] Other cell lines also used in this project were the SH-SY-5Y NB cell line and the PC-12, a rat PHEO cell line. HEK-transfected cells were cultivated in Dubelco's modified Eagle's medium (DMEM) Glutamax (Gibco, Paisley, UK) supplemented with 10% fetal bovine serum (FBS) (Biowest, Nuaillé, France), 1% of penicillin/streptomycin (P/S) commercial antibiotic mixture (Sigma, St Louis, MO, USA) and 500 µg/mL geneticin (Gibco, Paisley, UK) or 150 µg/mL hygromycin B (Brunschwig, Basel, Switzerland). Non-transfected HEK cells and all the other cell lines were maintained in DMEM Glutamax supplemented with 10% FBS and 1% of P/S solution. All cell lines were grown at 37°C in a 5% CO_2 atmosphere. Before 90% confluency was reached cells, were washed with phosphate buffered saline (PBS) without Ca^{2+} and magnesium (Mg^{2+}) (Bichsel, Interlaken, Switzerland) and then detached by using trypsin (BioConcept, Allschwill, Switzerland). After 3 min of incubation at 37°C, fresh medium containing FBS was added to cells and they were split in new flasks. Different cell culture plates are used for cell seeding depending on the experiment. Stock solution of mIBG and the inhibitors was prepared in dimethyl sulfoxide (DMSO) (Merck, Billerica, MA, USA) and then diluted to working concentrations.

Protein extraction and immunoblotting

Tumor tissues were lysed in a lysis buffer containing 0.1% sodium-dodecyl-sulphate (SDS) (Sigma, Steinheim, Germany) in PBS and then sonicated. Samples were clarified by a centrifugation step of 2000xg for 30 sec and pellet was discarded. To detect NET expression proteins were deglycosylated. To this aim, proteins were denatured with β-mercaptoethanol 5 min at 95°C and then mixed with 5% NP40, 0.4 M NaPO4 pH 7.4, protease inhibitors (Roche, Mannheim, Germany) and N-glycosidase F (Roche, Mannheim, Germany) and incubated 4 h at 37°C. Samples were then boiled for 5 min at 100ºC and 10 min at 65ºC, for NET and DAT detection, respectively. Protein samples were loaded and run on 12% w/v SDS-polyacrylamide gel electrophoresis using precastgels (Bio-Rad, Reinach, Switzerland), transferred to a polyvinylidene fluoride (PVDF) membrane and non-specific binding sites were blocked for 1 h with Tris-buffered saline (TBS) containing 4% (w/v) of non-fat dry milk. Membranes were incubated overnight at 4°C with primary antibodies diluted (1:1000) in TBS containing 4% non-fat dry milk and washed three times with TBS containing 0.1% Tween 20 (Sigma-Aldrich, St. Louis, USA) (TBS-T) for 10 min. The primary antibodies used were the mouse monoclonal anti-NET antibody (mab Technologies, #NET17-1), the rabbit polyclonal anti-DAT (Sigma-Aldrich, ab1766) and the monoclonal anti-β-actin AC-15 antibody (Sigma-Aldrich, Buchs, Switzerland). Then membranes were incubated 2 h with horseradish peroxidase (HRP)-conjugated secondary antibody at room temperature, diluted (1:4000) in TBS-T and washed three times with TBS-T for 10 min. Secondary antibodies were anti-mouse (170-6516, Bio-rad, CA, USA) and anti-rabbit antibody (170-6515, Bio-rad, Kabelsketal, Germany). The bound antibodies were detected by SuperSignal West Femto chemiluminescent HRP substrate kit (ThermoScientific, Rockford, USA) and imaged in a LAS 4000 imaging system. All membranes were re-probed with anti-β-actin antibody as loading control.

Cellular uptake of mIBG in HEK cells

To determine which monoamine transporters are able to internalize mIBG, HEK-transfected cells were seeded in 48-well cell culture plates in cell culture medium 24h before the uptake studies and then incubated with 100 nM mIBG (Axon Medchem, Groningen, The Netherlands) at 37°C for 0, 1 and 4 h.

For testing NET and DAT specific inhibitors the procedure was the same as described above except that 30 min before mIBG incubation, cells were treated with the specific transporter inhibitors (DMI for NET and GBR12935 for DAT; references are found in Annex 1) at 1 μM.

To determine kinetic values of mIBG internalization through NET and DAT, the protocol was the same but in this case cells were incubated with mIBG at different concentrations at 37°C for 10 min.

To evaluate the specificity of DMI and GBR12935 to NET and DAT, respectively, we used increasing concentrations of DMI and GBR12935 for 10 min at 37°C.

For all the different protocols the uptake was blocked by rapid removal of the medium containing mIBG and by adding cold PBS. Three washings with cold PBS buffer were performed and cells were lysed with 200 µL of PBS 0.2% Tween 20. Intracellular concentrations of mIBG were normalized to the total protein in each well using bicinchoninic acid (BCA) protein assay (ThermoScientific, Rockford, USA).

For all the experiments described, mIBG was extracted and quantified (procedure described in the following sections).

Proteomic analysis

HEK-293 transfected cells were seeded in a 75cm^2 T-flask and grown until a confluence of 90% and lysed with a buffer containing 0.1% SDS. Total proteins fraction were then analyzed and quantified by liquid chromatography-mass spectrometry (LC-MS/MS) at the laboratory of Protein Analysis Facility at the University of Lausanne.

Cellular uptake of mIBG in NB and PHEO cell lines

The procedure for quantification of mIBG internalization on IGR-NB8 cells and PHEO cells (PC-12) after its treatment with the different inhibitors was similar to the one used in HEK cells. Briefly, IGR-NB8 and PC-12 cells were seeded in 48-well cell culture plates and, after their adherence, cells were treated with HDACi for 48 h at 37°C (references for all HDACi in Annex 1). Cells were then incubated with 10nM mIBG at 37°C for 10 min.

To study the role of NET and DAT in mIBG internalization, IGR-NB8 cells were treated with CUDC-907 0.1 µM for 48 h following DMI and/or GBR12935 treatment at different concentrations (0.01, 0.05, 0.1, 0.5 and 1 µM) for 30 min. Cells were then incubated with mIBG 10 nM for 10 min. After mIBG incubation, the uptake was blocked by adding cold PBS. Three washings with cold PBS buffer were performed and cells were lysed with 100 µL of PBS 0.2% Tween 20. Intracellular concentrations of mIBG were normalized to the total protein in each well using a BCA protein assay.

For the study of mIBG accumulation in IGR-NB8 cells, cells were incubated with CUDC-907 for 48 h. Then at specific time points (48 h, 24 h, 12 h, 6 h, 1 h and 5 min), 10 nM mIBG was

added to the cells for 10 min. Afterwards, cells were washed with PBS and medium with or without CUDC-907 was added to the cells.

siRNA

ON-TARGETplus SMARTpool siRNA mixtures targeting NET (L-007602-00), DAT (L-007603-00), non-targeting control siRNA (D-001810-10) and GAPDH control siRNA (D-001830-10) were obtained from Horizon (Cambridge, UK). NB8 cells were plated in a 24-well cell culture plate 24 h before the experiment. IGR-NB8 cells were transfected with 25 nM siRNA mixture by using DharmaFECT standard transfection protocol. Negative control for the siRNA treatment were cells transfected with non-targeting control siRNA and positive control with GAPDH control siRNA. After 24 h of transfection cells were treated with CUDC-907 0.1 µM or BGT226 0.05 µM for 48 h, then cells were incubated with 10 nM mIBG at 37°C for 10 min. mIBG was then extracted and quantified by LC-MS/MS and results were expressed as the average fold difference between targeting siRNA compared with non-treated cells.

mIBG extraction and LC-MS/MS

Intracellular and extracellular mIBG was extracted by solid-phase extraction (SPE) performed on Waters Oasis WCX µElution plates (Waters, Milford, MA, USA). The phase was conditioned with 200 µL of methanol (Biosolve, Dieuze, France) and equilibrated with 200 µL of PBS. Thirty microliters or 40 µL of an internal standard solution at 2 nM (labeled molecular formula: $C_7{}^{13}CH_{10}IN^{15}N_2$) (Alsachim, Illkirch, France) and 30 µL or 40 µL of each sample were loaded and washed three times, for HEK cells and IGR-NB8 cells experiments respectively. First wash with 200 µL of water, then with 200 µL of methanol and finally with 200 µL of 0.2% formic acid in acetonitrile (Biosolve, Dieuze, France). The analytes were then eluted with a solution containing 2% of formic acid in acetonitrile: water (95:5) in a 350 µL 96-well plates or in a conical 700 µL 96-well plates for HEK cells experiments and IGR-NB8 cells experiments, respectively. Separation was performed in HILIC mode on a Waters Acquity UPLC I-class system (Waters, Milford, MA, USA) where 2 µL (HEK cells experiments) or 10 µL (IGR-NB8 cells experiments) of sample were injected on a silica column (Interchim Uptisphere Strategy 100Å HILIC, 100 mm × 2.1 mm, 2.2 µm) (Alsachim, Montluçon, France). The mobile phases were composed of: 100% acetonitrile (A) and 100 mM ammonium formate (B) (Honeywell Fluka, Muskegon, MI, USA). Table 2 describes the gradient and flow rates. A solution of acetonitrile 50% was used as strong wash, whereas a solution of acetonitrile 95% was used as weak wash and solution of acetonitrile 5% was used as seal wash. The temperature

of the autosampler and the column were 10°C and 25°C, respectively. A Waters Xevo TQ-S triple quadrupole mass spectrometer equipped with an electrospray interface was coupled to the LC system and the analysis were performed in a positive ionization mode. The MRM transitions used for quantification were 275.97 (m/z) and 89.93 (m/z) for precursor ion and product ion, respectively, the cone voltage at 34 V and collision energy at 20V. The ESI conditions were set as follows: capillary voltage 0.60 kV, desolvation temperature 600°C, source temperature 150°C, desolvation gas flow 900 L/h, cone gas flow 150 L/h, nebulizer gas 7.0 bar, and collision gas flow 0.25 mL/min. At the beginning of each series, a calibration curve was injected and three quality controls (QC) samples (high, medium and low) were randomly placed in every 96-well plate. Data was processed using the TargetLynx module. The protocols and results of the validation of the method can be found in Annex 2.

Table 2 - Chromatographic gradient used for the separation of mIBG by LC-MS/MS.

Time (min)	Flow (mL/min)	% solution A	% solution B
Initial	0.350	5.0	95.0
4.00	0.350	30.0	70.0
6.00	0.350	30.0	70.0
6.10	0.350	5.0	95.0
9.00	0.350	5.0	95.0

Cellular viability

A trypan blue assay was used to measure the cell viability of the different inhibitors in IGR-NB8 cells. Cells were seeded in a 48-well cell culture plate and after their adherence incubated 48 h with vehicle control (DMSO) or the different inhibitors. After treatment, medium was discarded and cells were washed once with PBS. Then 50 μL of trypsin was added to each well for 5 min and cells were resuspended in 200 μL of medium. Cells were collected and 100 μL of cells were mixed with 100 μL of trypan blue solution 0.4% (Gibco, NY, USA). The percentage of viable cells was calculated allowing the following formula:

Cell viability $= 1 - (\frac{\text{number of dead cells}}{\text{total number of cells}})\ X\ 100$.

RNA extraction and qRT-PCR

The extraction of total RNA from cells was performed by using the Trizol Reagent (Ambion, Carlsbad, CA, USA) according to the manufacturer's protocol. RNA concentration was quantified using Nanodrop 2000 spectrophotometer and 1 μg of total RNA was used for cDNA

synthesis with the PrimeScript Reverse transcriptase kit (Takara Bio Inc, Japan) as per manufacturer instructions. The resulting cDNA was used as template for the quantitative real-time PCR (qRT-PCR) by using the SYBR Green Master Mix (Roche, Basel, Switzerland) for human NET, human DAT, human transporter glyceraldehyde 3-phosphate dehydrogenase (GAPDH) and human transporter eukaryotic translation elongation factor 1 alpha 1 (EEIF1A1). Primers are described in table 3 and were designed using the tool "Primer Blast" on the NCBI page and ordered from Microsynth (Balgach, Switzerland). Reactions were performed in a QuantStudio 6 Real-Time PCR System and amplification was carried out in a 384-well reaction plate as follows: 95°C for 10 min followed by 40 cycles of 95°C for 15 sec and 60°C for 1 min. Each sample was analyzed in duplicate and a negative control was prepared by using the same amount of total RNA but without adding the enzyme transcriptase reverse. Expression levels of NET and DAT transcripts were calculated relatively to the level of the housekeeping genes GAPDH and EEIF1A1 using the $\Delta\Delta$Ct method.[89]

Table 3 – Primers used for RT-qPCR of NB8 cells incubated or not with different HDACi.

Primers	Sequence
hNET Forward	5' TGA TGG GGT TCA GGC CGG GT 3'
hNET Reverse	5' TTG GGC CAG GGC GGG AAG AT 3'
hDAT Forward	5' CCA TAG ACG GCA TCA GAG CA 3'
hDAT Reverse	5' CCG CGT CAA TCC AAA CAG A 3'
hGAPDH Forward	5' CAT CCA TGA CAA CTT TGG TAT CGT 3'
hGAPDH Reverse	5' CCA TCA CGC CAC AGT TTC C 3'
hEEIF1A1 Forward	5' CTG AAC CAT CCA GGC CAA AT 3'
hEEIF1A1 Reverse	5' GCC GTG TGG CAA TCC AAT 3'

Immunofluorescence microscopy

Cells were seeded in coverslips coated with poly-L-lysine (Sigma, St-Louis, MO, USA) into a 24-well cell culture plate and treated or not with CUDC-907 for 48 h. Cells were fixed with 2% of paraformaldehyde in PBS (Sigma, Steinheim, Germany) for 20 min at room temperature and washed twice with PBS for 5 min. Cells were permeabilized with 0.2% Triton X-100 (PanReac Applichem, Darmstadt, Germany) in PBS for 10 min and then cells were washed twice with

PBS for 5 min. Cells were then blocked with 1% bovine serum albumin (BSA) (Sigma, St Louis, MO, USA) in PBS for 1 h. Cells were incubated 2 h at room temperature with the primary antibody diluted 1:300 with 0.1% BSA in PBS. Then cells were washed three times with PBS and incubated 2 h in dark at room temperature with the secondary antibody diluted 1:200 with 0.1% BSA in PBS. Afterwards cells were washed twice with PBS and for nuclear staining cells were incubated with DAPI diluted 1:300 in water for 10 min in the dark at room temperature. Cells were imaged using a fluorescence microscope (Leica DFC 345 FX) and then analyzed with the Image J software (Version 2.6.0, build 7266). Specificity was demonstrated by primary antibody omission.

In vivo studies

All the *in vivo* experiments were performed at the laboratory of Prof. Melpomeni Fani (Division of Radiopharmaceutical Chemistry, University Hospital Basel) by Dr. Rosalba Mansi. All animal experiments were carried out with female athymic nude-Foxn1^{nu}/Foxn1^{+} mice (Envigo, The Netherlands), approved by the Veterinary Office (Department of Health) of the Cantonal Basel-Stadt (approval no 32562) in accordance with the Swiss regulations for animal treatment.. Twenty-five mice (4-6 weeks old) were subcutaneously implanted with $2x10^6$ IGR-NB8 cells/mouse in DMEM/matrigel and monitored twice a week. One month later, the tumors reached the size of 120-200 mm^3 and the mice were ready to use for the experiments. Animals were randomly divided in three groups: group A (n=11), B (n=9) and C (n=5). The group A and B received respectively 10 mg/Kg and 5 mg/Kg of CUDC-907 while the group C received the vehicle (10% DMSO in corn oil). CUDC-907 was administered for 5 days, via oral gavage, at the doses indicated and after 2 days' drug free the mice were injected with ^{123}I-mIBG. Biodistribution studies were performed 4 h and 24 h after the injection of ^{123}I-mIBG (2-4 MBq/100 µL) for quantification of the radioactivity in all organs of interest. One mouse from each group, with a tumor size eligible for imaging, was injected with 13-17 MBq ^{123}I-mIBG and imaged supine, head first, using a SPECT/CT system dedicated to imaging small animals (Nano-SPECT/CT™ Bioscan Inc.) at 4 h post-injection (p.i.) and 24 h p.i. The SPECT/CT images after 4 h p.i. were acquired for 90 min with the mice being anesthetized (remained alive). The day after, the same mice were sacrificed and the SPECT/CT images after 24 h p.i. were acquired for 170 min. All mice were pretreated with Irenat (120 mg/kg) before ^{123}I-mIBG injection to reduce the uptake in I-avid organs. Results were described as percent of injected activity per gram of tissue (%IA/g).

SPECT images were reconstructed iteratively and filtered using the HiSPECT software package (version 1.4.1876, SciVis GmbH, Goettingen, Germany) and the manufacturer's algorithm (3 subsets, 9 iterations, 35% post-filtering, 128 × 128 matrix, zoom 1,30 x 20 mm transaxial field of view, resulting in a pixel size of 0.3 mm). CT images were reconstructed using CTReco (version r1.146), with a standard filtered back projection algorithm (exact cone beam) and post-filtered (RamLak, 100% frequency cut-off), resulting in a pixel size of 0.2 mm. Co-registered images were visualized in the three orthogonal planes using maximum intensity projection with InVivoScope (version 1.43, Bioscan Inc.).

Statistics

Data are presented as the mean ± standard deviation (SD) and statistical analyses were carried out using GraphPad Prism 4.0 (La Jolla, CA, USA). Statistical analysis were performed through either two-way ANOVA and unpaired t-test and p-value of less than 0.05 was considered statistically significant.

Results

Study of the correlation between NET and DAT protein expression and ^{123}I-mIBG internalization

The starting point of this thesis was to determine NET and DAT protein level in biopsies from patients that underwent I[131]-mIBG scintigraphy before surgery. Through immunoblotting, we assessed the correlation between mIBG-positive and -negative internalization in patients and NET and DAT protein expression (Figure 15). Twenty-one mIBG-positive and two -negative internalization (P75 and P94) samples were selected. The results showed that NET and DAT protein expression was highly variable among the different samples and that tumors presenting a mIBG-positive internalization through single-photon emission computed tomography (SPECT), did not necessarily present NET protein expression. Samples P12, P22, P35, P37 and P79, which did not show detectable levels of NET protein expression, displayed mIBG-positive internalization. Samples P12, P37 and P79 presented mIBG-positive internalization while showing only DAT protein expression and not NET. Samples P22 and P35, which did not present either NET and/or DAT protein expression, still showed mIBG-positive internalization. On the other hand, samples P75 and P94 with mIBG-negative internalization showed NET and DAT protein expression. These results demonstrate the lack of correlation between NET and/or DAT protein expression and mIBG-positive internalization.
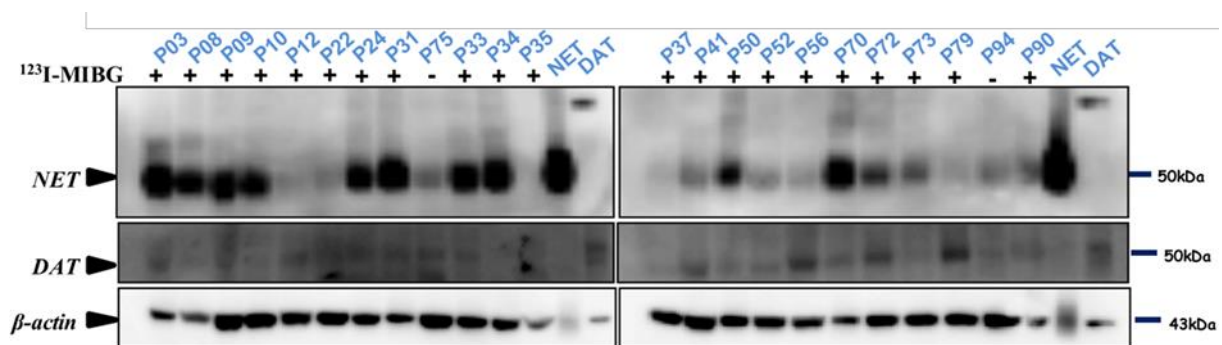
Figure 15 - Lack of correlation between NET and DAT protein expression and ^{123}I-mIBG internalization in PHEO tumor biopsies.
Immunoblotting analysis of NET and DAT protein expression in PHEO tumor biopsies from patients. P75 and P94 were used as negative control for mIBG internalization. HEK-NET and HEK-DAT protein extracts were used as positive controls for NET and DAT expression, respectively and β-actin was used as a loading control.

Identification of monoamine transporter(s) involved in mIBG internalization

In order to investigate the lack of correlation between positive mIBG imaging results and the expression of NET and DAT proteins on the surface of tumor cells taken from PHEO patients biopsies we first determined which monoamine transporters are able to internalize mIBG (Figure 16). To do so, we used stable HEK-293 transfected cells with plasmids encoding for

the monoamine transporters of interest (HEK-NET, HEK-DAT, HEK-OCT1, HEK-OCT2, HEK-OCT3 and HEK-PMAT) as our cell line models. Since mIBG is an analog of NE, these transporters were chosen due to their affinity for NE. mIBG internalization by NET was confirmed using HEK-NET (t1h = 177.873 ± 36.421 pmol/µg protein, fold change = 39.992 ± 8.189; p<0.0001; t4h = 257.432 ± 68.793 pmol/µg protein, fold change = 91.884 ± 24.554; p<0.0001) and internalization was significantly higher compared to the controls (t1h = 4.448 ± 1.567 pmol/µg protein; t4h = 2.802 ± 1.057 pmol/µg protein). Additionally, HEK-DAT showed a significant increase in mIBG internalization, demonstrating that mIBG is also internalized by DAT (t1h = 151.309 ± 27.505 pmol/µg protein, fold change = 34.020 ± 6.184; p<0.0001; t4h = 178.240 ± 96.300 pmol/µg protein, fold change = 63.618 ± 34.372; p<0.0001). Also, HEK-OCT1 (t1h = 13.189 ± 3.440 pmol/µg protein, fold change = 2.965 ± 0.774; t4h = 13.841 ± 2.772 pmol/µg protein, fold change = 4.940 ± 0.989), HEK-OCT2 (t1h = 23.611 ± 11.102 pmol/µg protein, fold change = 5.309 ± 2.496; t4h = 20.034 ± 3.660 pmol/µg protein, fold change = 7.151 ± 1.306), and HEK-OCT3 (t1h = 28.235 ± 5.870 pmol/µg protein, fold change = 6.348 ± 1.320; t4h = 31.920 ± 4.032 pmol/µg protein, fold change = 11.393 ± 1.439), were able to internalize mIBG but to a lesser extent, compared with HEK-NET and HEK-DAT. Finally, HEK-PMAT (t1h = 4.527 ± 3.424 pmol/µg protein, fold change = 1.018 ± 0.770; t4h = 4.652 ± 4.305 pmol/µg protein, fold change = 1.660 ± 1.537), showed no differences compared to controls. mIBG internalization in HEK-NET after 4h of incubation was significantly higher than after 1 h of incubation (t1h vs t4h: fold change = 1.447 ± 0.387, p = 0.0032). No other HEK-transfected cell line displayed significant differences between 1 h and 4 h of incubation (HEK-DAT t1h vs t4h: fold change = 1.178 ± 0636, p = 0.469).
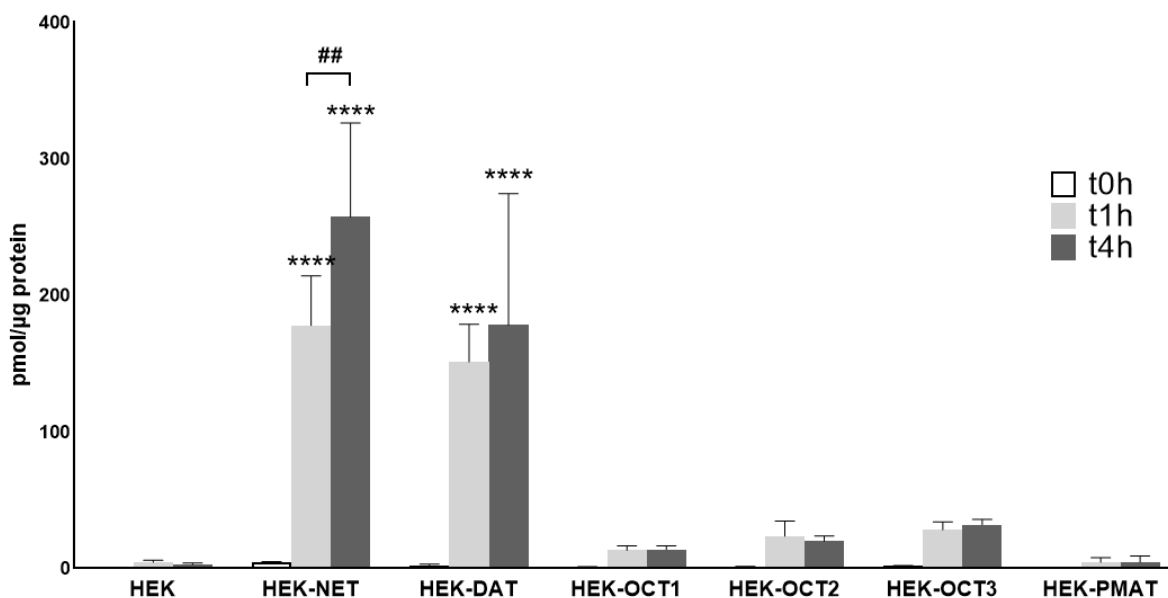
Figure 16 - mIBG is essentially internalized by NET and DAT in HEK-transfected cells.
HEK transfected cells were incubated with mIBG 100 nM for 0 h, 1 h and 4 h. Intracellular mIBG was then extracted through SPE plate and quantified by LC-MS/MS. Results were normalized with a BCA test and compared with the control (non-transfected HEK cells). Statistical analysis were performed through two-way ANOVA between the control (HEK) and each of the groups. ****, $p<0.0001$; ##, $p<0.01$. All the experiments were performed 3 times in triplicates.

The amount of transporter present in the membrane was assessed via a proteomics approach to prevent a possible bias when analyzing the results on Figure 16. Protein levels among different HEK-transfected cells was similar, thus excluding the influence of a possible distinct amount of transporters present in the cells surface between each cell line tested (Figure 17).
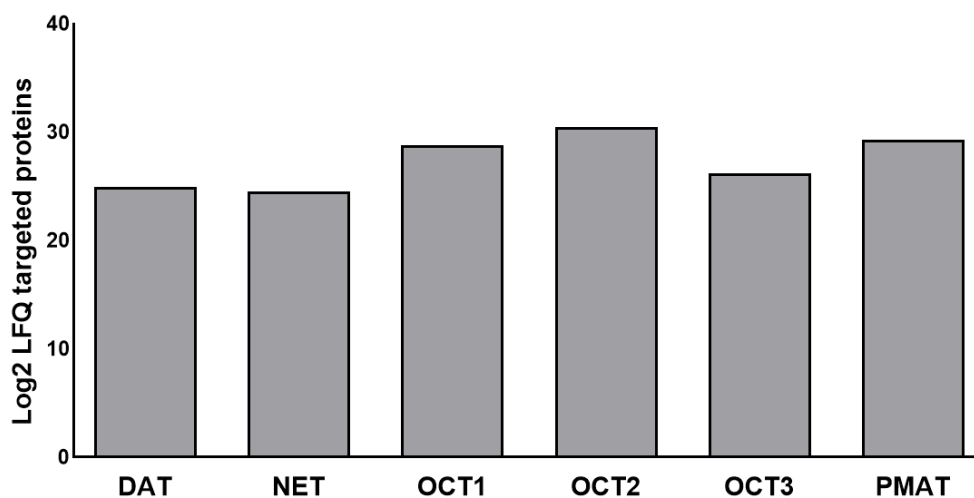
Figure 17 - The protein levels of the monoamine transporters are similar between each HEK-transfected cell line.
HEK-transfected cells were lysed and total proteins fraction were then analyzed and quantified by LC-MS/MS. LFQ, label-free quantification.

43

Determination of NET and DAT affinity to mIBG

Once we assessed that NET and DAT were able to internalize mIBG we proceeded to the determination of the kinetic values regarding the affinity (Km) and capacity (Vmax) for mIBG (Figure 18 and 19, respectively). We observed that HEK-NET showed higher affinity (Km = 995 nM) but lower capacity (Vmax=1135 pmole/min) to mIBG than HEK-DAT which showed lower affinity (Km = 2807 nM) but higher capacity (Vmax=2604 pmole/min).
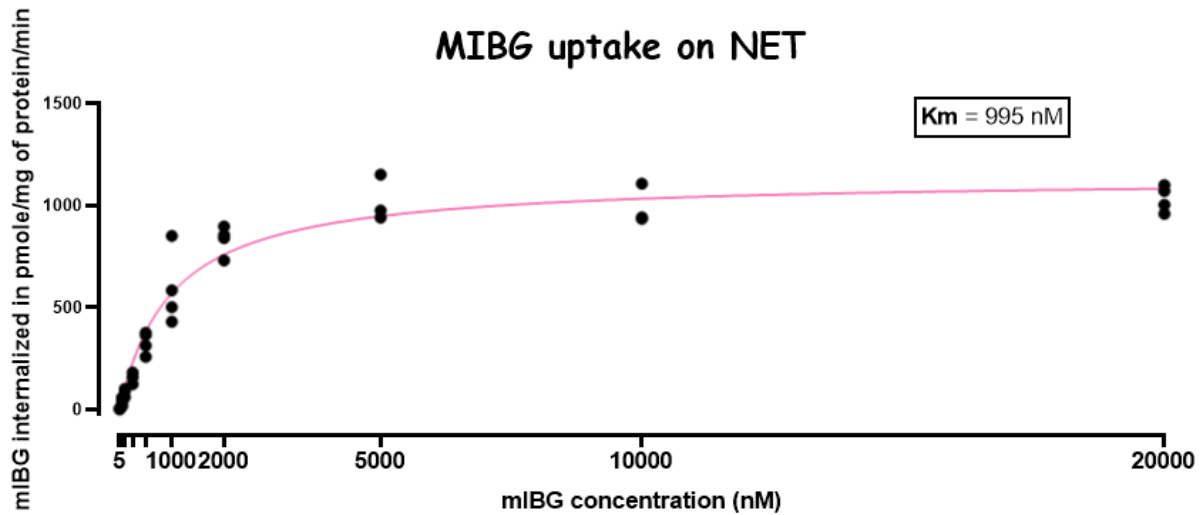
Figure 18 - NET presents high affinity to mIBG in HEK-NET cells.
HEK-NET transfected cells were incubated with mIBG at increasing concentrations for 10 min. Intracellular mIBG was then extracted through SPE plate and quantified by LC-MS/MS. Results were normalized with a BCA test. Non-linear regression was drawn using Graphpad Prism's Michaelis-Menten interpolation. All the experiments were performed at least 3 times in duplicates. Points in graph correspond to the mean of each duplicate.
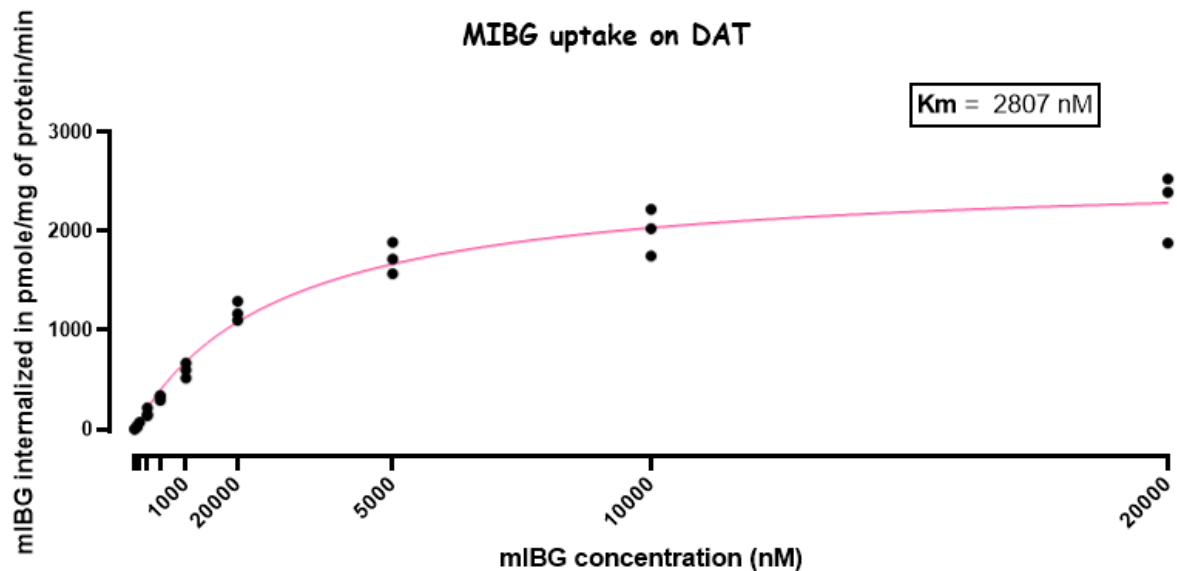
Figure 19 - DAT presents lower affinity to mIBG than NET in HEK-DAT cells.

44

HEK-DAT transfected cells were incubated with mIBG at increasing concentrations for 10 min. Intracellular mIBG was then extracted through SPE plate and quantified by LC-MS/MS. Results were normalized with a BCA test. Non-linear regression was drawn using Graphpad Prism's Michaelis-Menten interpolation. All the experiments were performed at least 3 times in duplicates. Points in graph correspond to the mean of each duplicate.

Determination of the specificity of DMI and GBR12935 on NET and DAT

As described in the literature, DMI is a NET-specific inhibitor and GBR12935 a DAT-specific inhibitor.[90, 91] The specificity of these inhibitors was assessed using each of the inhibitors at increasing concentrations on HEK-NET and HEK-DAT. DMI is a very specific inhibitor for NET (Figure 20 A) in HEK-NET (IC_{50} = 28.41 nM) and GBR12935 is a very specific inhibitor for DAT (Figure 20 C) in HEK-DAT (IC_{50} = 50.31 nM). No specificity was observed for DMI toward DAT (Figure 20 D), and GBR12935's inhibitory concentration of NET (Figure 20 B) was very high (IC_{50} = 3610 nM), meaning that GBR12935 has a very low activity on NET. These results show that both DMI and GBR12935 represent very specific inhibitors for respectively NET and DAT.
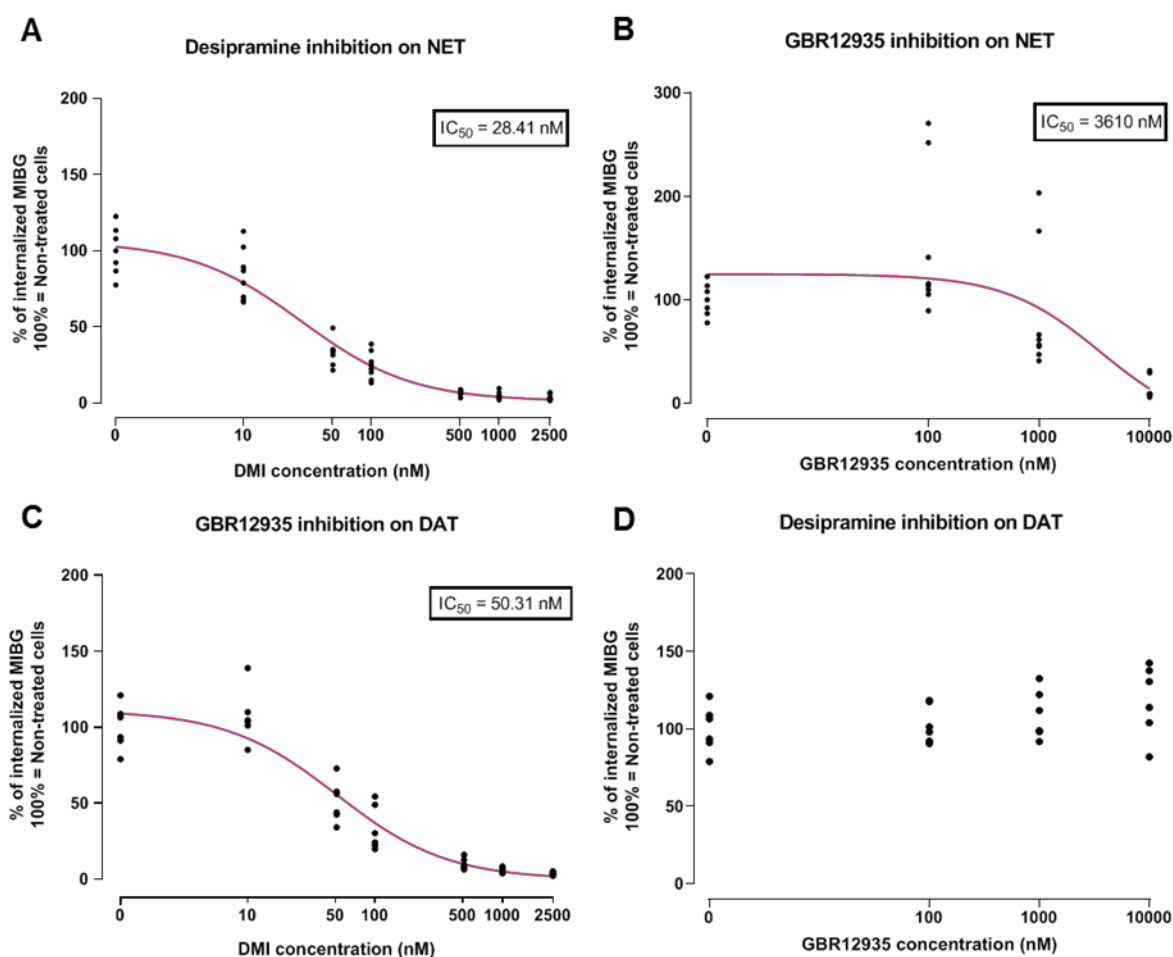
Figure 20 – DMI shows NET specific inhibition and GBR12935 shows DAT specific inhibition.
HEK transfected cells (HEK-NET and HEK-DAT) were treated with DMI or GBR12935 at increasing concentrations and then mIBG. Intracellular mIBG was then extracted through SPE plate and quantified by LC-

MS/MS. Results were normalized by a BCA test. Curves were obtained through nonlinear regression and fit function of Graphpad Prism 4.0. All the experiments were repeated at least 3 times in duplicates.

Selection of a NB cell line model

After determining which type of transporters has the ability to internalize mIBG, we explored several NB cell lines to find one that display expression of all type of transporter of interest to be used in the present study. Following qPCR analysis of the mRNA expression of monoamine transporter genes in different NB cell lines, we determined that IGR-NB8 cell line was the only one tested which expressed each type of monoamine transporters of interest including a high level of NET expression (Table 4).

Table 4 - Expression of the monoamine transporters in different NB cell lines.

	NET	DAT	OCT1	OCT2	OCT3	PMAT	TBP
Be2C	20.537	ND	30.298	ND	32.820	23.560	28.542
CA2E	ND	30.749	28.632	28.445	ND	27.410	ND
Gimen	ND	ND	32.608	ND	ND	31.551	ND
IMR32	25.017	30.266	31.409	ND	ND	24.676	ND
LAN-1	23.541	26.433	30.998	33.299	ND	21.800	ND
N91	19.479	ND	32.139	ND	ND	24.846	ND
IGR-NB8	20.901	28.456	27.791	26.830	28.991	25.878	ND
SH-SY-5Y	20.339	ND	30.261	30.261	ND	22.51	ND
SK-N-DZ	22.042	32.543	30.262	32.802	ND	23.376	ND

Values presented are shown as cycle threshold (Ct). ND, not detected. TATA box-binding protein (TBP) was used to normalize the results regarding the RNA amount among all cell lines.

Screening of HDACi and its effect on mIBG internalization in IGR-NB8 cells

Vorinostat, a HDACi, has been reported to increase the expression of NET and improve mIBG internalization in NB tumors.[69] To find other HDACi that may have a greater increase in NET and DAT expression and consequently an increase in mIBG internalization, we tested a library of HDACi (Figure 21). Mocetinostat 0.5 µM (mocetinostat vs DMSO fold change = 1.476 ± 0.339; $p<0.05$) and PCI-24781 0.2 µM (PCI-24781 vs DMSO fold change = 1.661 ± 0.268; $p<0.01$) were observed to slightly increase mIBG internalization compared to the control. Furthermore, CUDC-907 0.1 µM (CUDC-907 vs DMSO fold change = 2.159 ± 0.580; $p<0.0001$), and sodium-4-P 5 mM (Sodium-4-P vs DMSO fold change = 2.129 ± 0.309; $p<0.001$) both significantly increased mIBG internalization. Interestingly, vorinostat, a

compound which has been shown to increase NET expression and mIBG internalization in Kelly and SH-SY-5Y cells, did not induce significant changes in mIBG internalization in IGR-NB8 cells at 0.5 μM (vorinostat vs DMSO fold change = 0.906 ± 0.189).[69] These results demonstrate that CUDC-907 is the most potent drug to increase mIBG-internalization in IGR-NB8 cells.
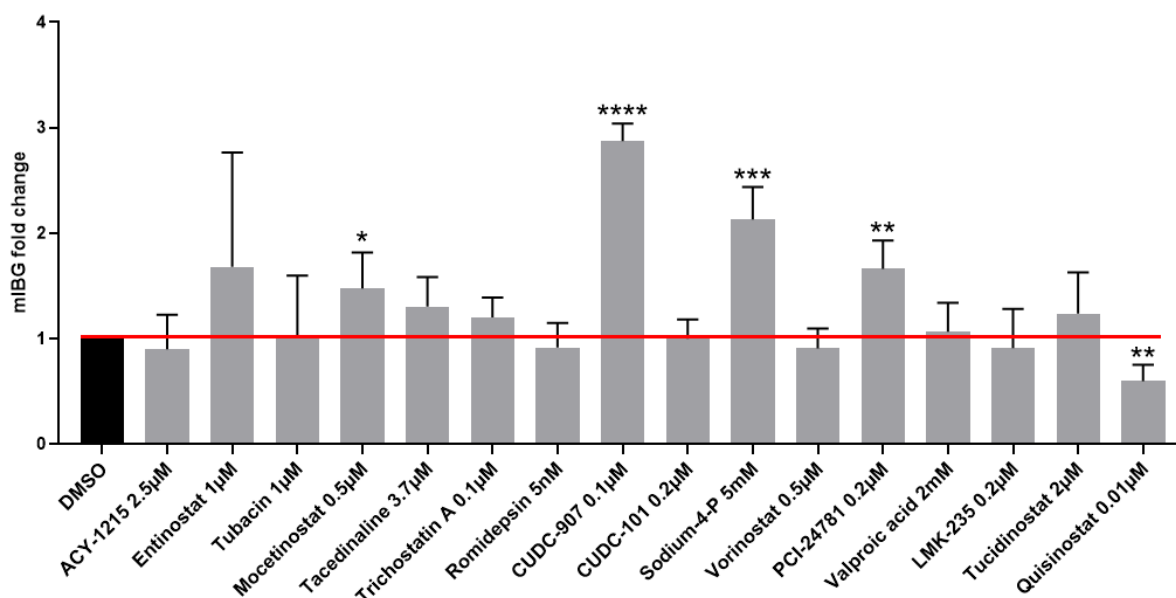
Figure 21 - CUDC-907 and sodium-4-P significantly increase mIBG internalization in IGR-NB8 cells. IGR-NB8 cells were incubated with different HDACi for 48 h and then with mIBG. Intracellular mIBG was then extracted through SPE and quantified by LC-MS/MS. Results were normalized by a BCA test and expressed as fold of increase in mIBG internalization compared with non-treated cells (DMSO). Statistical analysis was performed through unpaired t-test between the control and condition tested. *, $p<0.05$; **, $p<0.01$, ***, $p<0.001$, ****, $p<0.0001$. All the experiments were performed at least 3 times in duplicates.

The cell viability of the HDACi-treated cells was evaluated via Trypan blue assay to demonstrate that the presence of the HDACi was not toxic to the cells (Figure 22). Results showed no cell viability differences between the DMSO-treated cells and the HDACi-treated cells at the concentrations used.
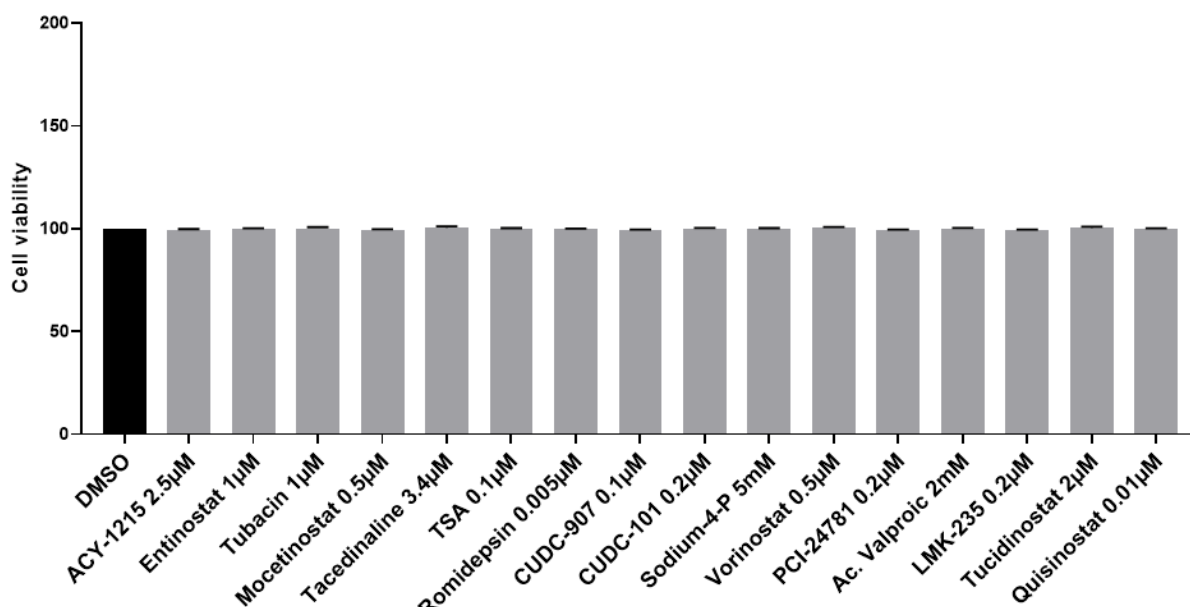
Figure 22 - The cell viability is not affected by the presence of the different HDACi in IGR-NB8 cells. IGR-NB8 cells were incubated with different HDACi for 48 h and then a trypan blue assay was performed. The experiment was performed once in triplicate.

Since CUDC-907 increases approximately 3 times the fold change of mIBG internalization, we proceeded with different combinations of two (Figure 23) and three (Figure 24) HDACi to find a combination that could further increase the mIBG internalization efficiency. Therefore, CUDC-907 0.05 μM was combined with mocetinostat 0.5 μM (fold change = 1.996 ± 0.564; p<0.01), with tacedinaline 2 μM (fold change = 1.890 ± 0.266; p<0.001), with entinostat 0.5 μM (fold change = 1.661 ± 0.420; p<0.01), with ACY-1215 1 μM (fold change = 1.551 ± 0.466; p<0.05). CUDC-907 0.1 μM was also combined with sodium-4-P 2 mM (fold change = 2.316 ± 0.899; p<0.05). Although some combinations were statistically different to the DMSO control, none had a higher effect than CUDC-907 alone. Additionally, other combinations were tested, including tacedinaline 1 μM with mocetinostat 0.25 μM (fold change = 1.278 ± 0.187; p<0.05) and tacedinaline 2 μM with entinostat 1μM (fold change = 1.352 ± 0.322; p<0.05). These results showed the combinations of two HDACi had no greater effect than CUDC-907 alone.
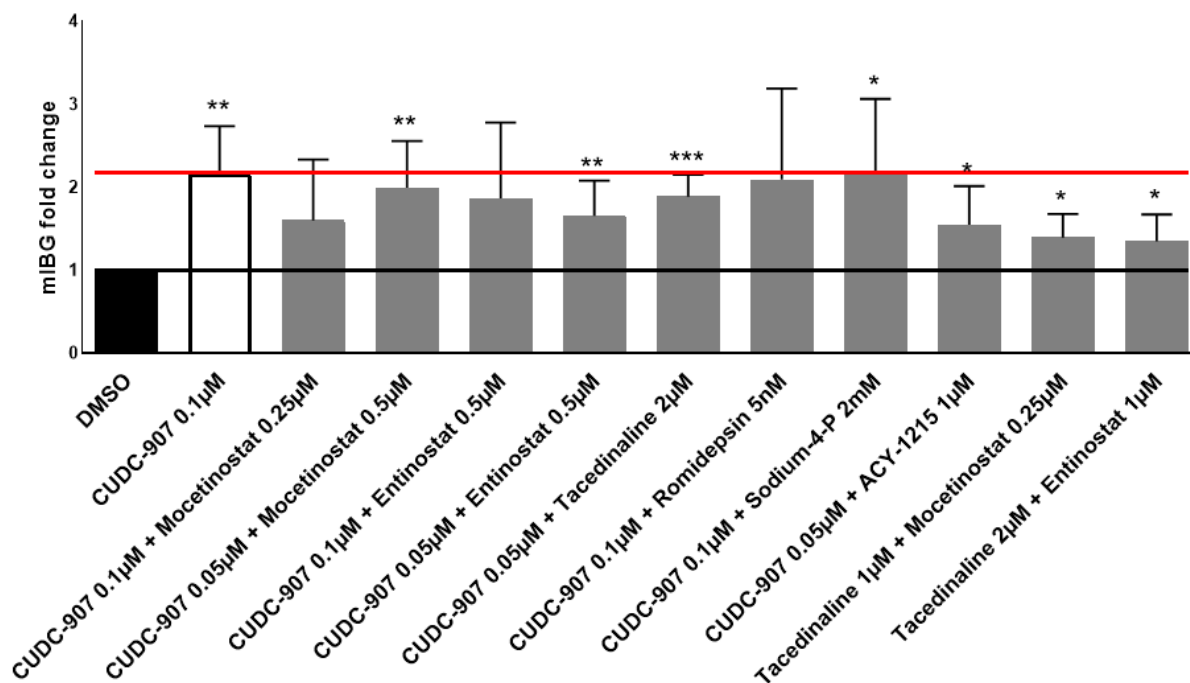
Figure 23 - Combination of two HDACi has no additional effects compared to CUDC-907 0.1 μM alone.
IGR-NB8 cells were incubated with different HDACi for 48 h. Then mIBG 10 nM was added to cells for 10 min. Intracellular mIBG was then extracted through SPE plate and quantified by LC-MS/MS. Results were normalized by a BCA test and expressed as fold of increase in mIBG internalization compared with non-treated cells (DMSO). The experiments were repeated 3 times in duplicates. The black line corresponds to the control mIBG internalization and the red line corresponds to the CUDC-907 0.1 μM mIBG internalization. Statistical analysis was performed through unpaired t-test between the control and condition tested. *, $p < 0.05$; **, $p < 0.01$; ***, $p < 0.001$.

For the combination of three candidates, we used CUDC-907 combined with tacedinaline, entinostat and mocetinostat in different combinations and concentrations (Figure 24). CUDC-907 0.05 μM combined with tacedinaline 1 μM and entinostat 0.5 μM (fold change = 1.845 ± 0.230; $p < 0.01$), combined with tacedinaline 0.5 μM and mocetinostat 0.1 μM (fold change = 1.575 ± 0.156; $p < 0.01$) and combined with tacedinaline 0.5 μM and mocetinostat 0.25 μM (fold change = 1.707 ± 0.141; $p < 0.001$) showed significantly higher mIBG internalization than the control. However, the first three combinations were not greater than CUDC-907 alone. CUDC-907 0.1 μM combined with entinostat 0.5 μM and mocetinostat 0.1 μM (fold change = 2.773 ± 0.824; $p < 0.05$) showed a higher mIBG internalization than CUDC-907 alone. However, since this effect requires the use of three different inhibitors and was not significantly higher than CUDC-907's effect, we continued our tests only with CUDC-907.
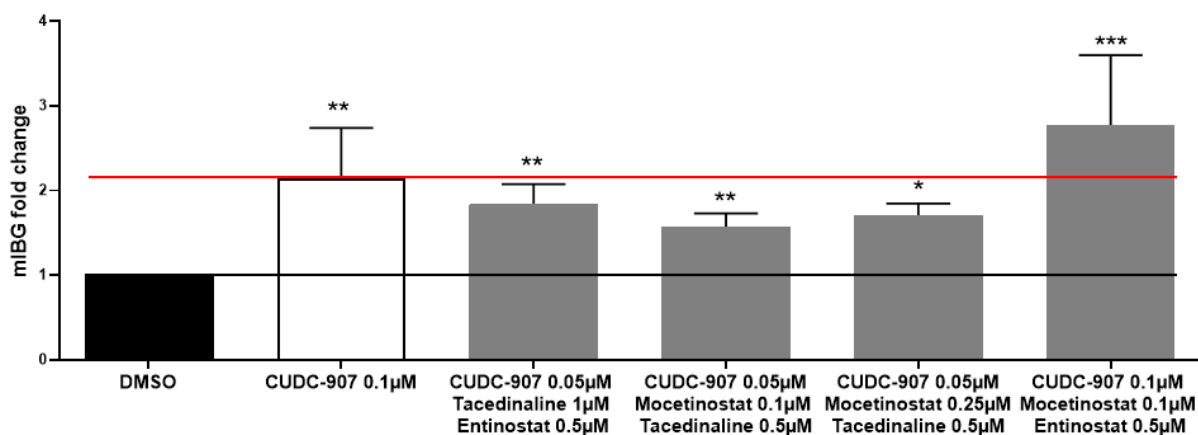
Figure 24 - Combination of 3 HDACi has no additional effects compared to CUDC-907 0.1 µM alone.
IGR-NB8 cells were incubated with different HDACi for 48 h. Then mIBG 10nM was added to cells for 10 min. Intracellular mIBG was then extracted through SPE plate and quantified by LC-MS/MS. Results were normalized by a BCA test and expressed as fold of increase in mIBG internalization compared with non-treated cells (DMSO). The experiments were repeated 3 times in duplicates. The black line corresponds to the control mIBG internalization and the red line corresponds to the CUDC-907 0.1 µM mIBG internalization. Statistical analysis was performed through unpaired t-test between the control and condition tested. *, $p<0.05$; **, $p<0.01$; ***, $p<0.001$.

Study of the effect of CUDC-907 on mIBG internalization in IGR-NB8 cells

CUDC-907 being the most efficient HDACi tested for mIBG internalization we decided to further study its effects. We first tested different concentrations of CUDC-907 and we observed that CUDC-907 presents a dose-dependent increase in mIBG internalization (fold change: 0.01 µM = 1.403 ± 0.075; 0.05 µM = 2.415 ± 0.530; 0.1 µM = 2.874 ± 0.165) (Figure 25).
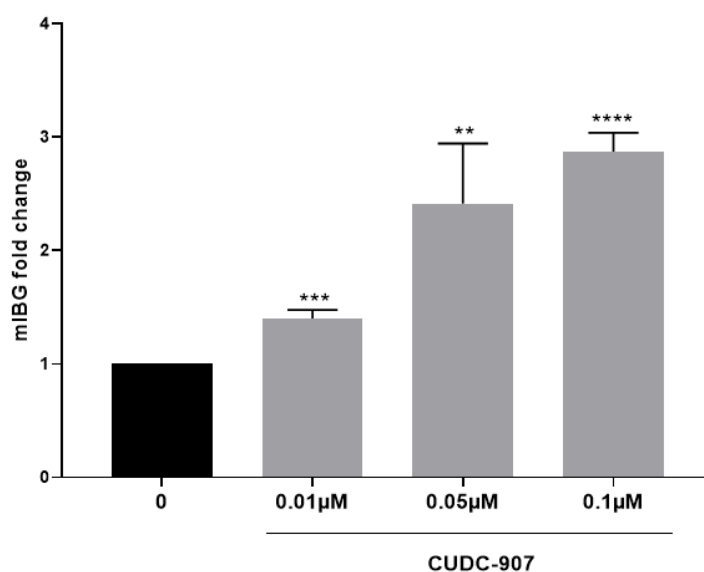
Figure 25 - CUDC-907 increases mIBG internalization in IGR-NB8 cells in a dose-dependent manner.
IGR-NB8 cells were incubated with CUDC-907 at increasing concentrations for 48 h and then with mIBG. Results were normalized by a BCA test and expressed as fold of increase in mIBG internalization compared with non-

treated cells (DMSO). Statistical analysis was performed through unpaired t-test between the control and condition tested. **, p<0.01; ***, p<0.001; ****p<0.0001.

Then we decided to analyze the affinity of IGR-NB8 cells toward mIBG in the presence and absence of CUDC-907 by determining the kinetic values (Km and Vmax) (Figure 26). IGR-NB8 cells treated with CUDC-907 showed higher affinity to mIBG (Km = 347.8 nM) compared to non-treated cells (Km = 3684 nM). The capacity of mIBG transport remained relatively unchanged, independently of CUDC-907 treatment (Vmax = 231.3 pmol/min and Vmax = 232.8 pmol/min, for IGR-NB8 non-treated and treated cells, respectively).These results indicate that CUDC-907 decreases the amount of mIBG needed to reach the maximum velocity of transport.
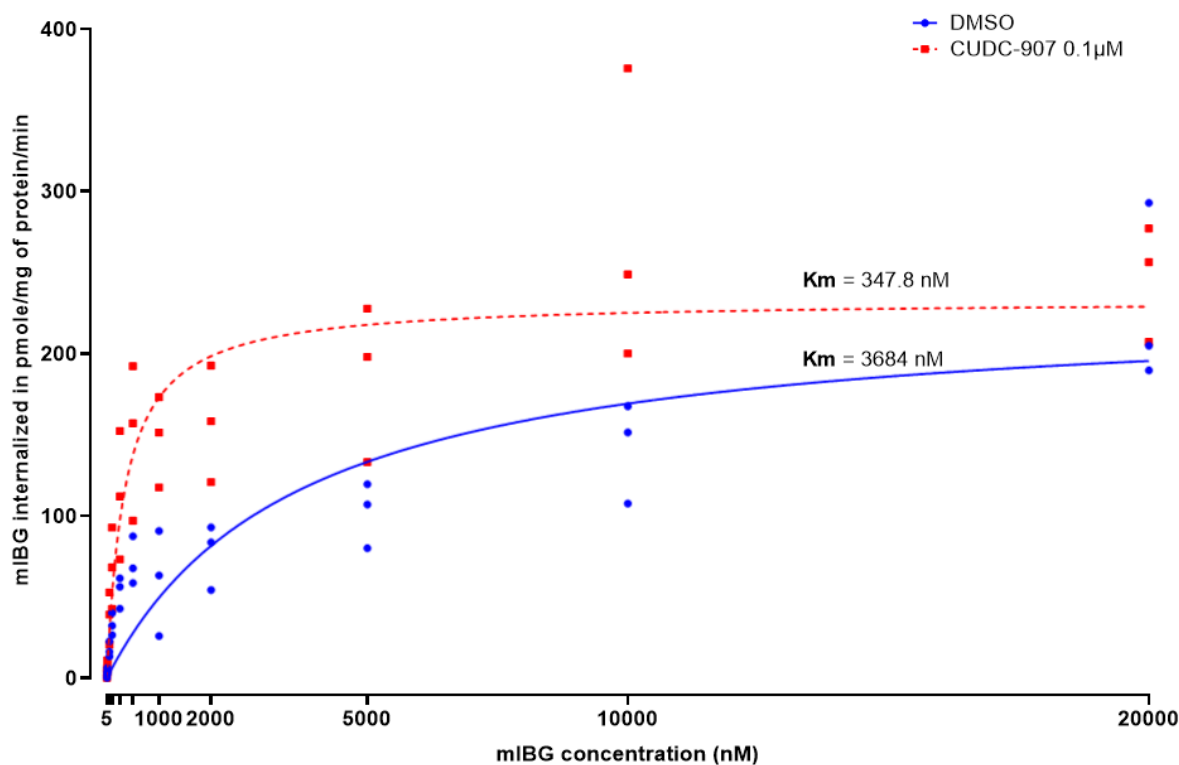
Figure 26 – CUDC907 increases the affinity of IGR-NB8 cells to mIBG.
IGR-NB8 cells were treated or not with CUDC-907 0.1 μM for 48 h. Then cells were incubated with mIBG at increasing concentrations for 10 min. Intracellular mIBG was then extracted through SPE plate and quantified by LC-MS/MS. Results were normalized with a BCA test. Non-linear regression was drawn using Graphpad Prism's Michaelis-Menten interpolation. All the experiments were performed 3 times in duplicates. Points in graph correspond to the mean of each duplicate.

Finally, we studied the ability of IGR-NB8 cells to keep mIBG internalized after CUDC-907 incubation. Intra- and extracellular mIBG was collected at different time points (5 min, 1 h, 6 h, 12 h, 24 h and 48 h) and quantified to assess whether mIBG is secreted or diffused by IGR-NB8 cells through time (Figure 27). Results showed that intracellular mIBG content remains unchanged up to 12 h, regardless of CUDC-907 treatment during the incubation time considered. After 24 h, intracellular mIBG content was higher in constantly CUDC-907 treated

51

cells. The extracellular content remains very low and relatively unchanged up to 6 h and after 24 h of incubation we observed a significant decrease of extracellular mIBG in CUDC-907 treated cells compared to non-treated cells, meaning that mIBG is efficiently stored in the cells. This result demonstrated that mIBG is efficiently stored in the cytoplasm for at least 48 h after initial incubation.
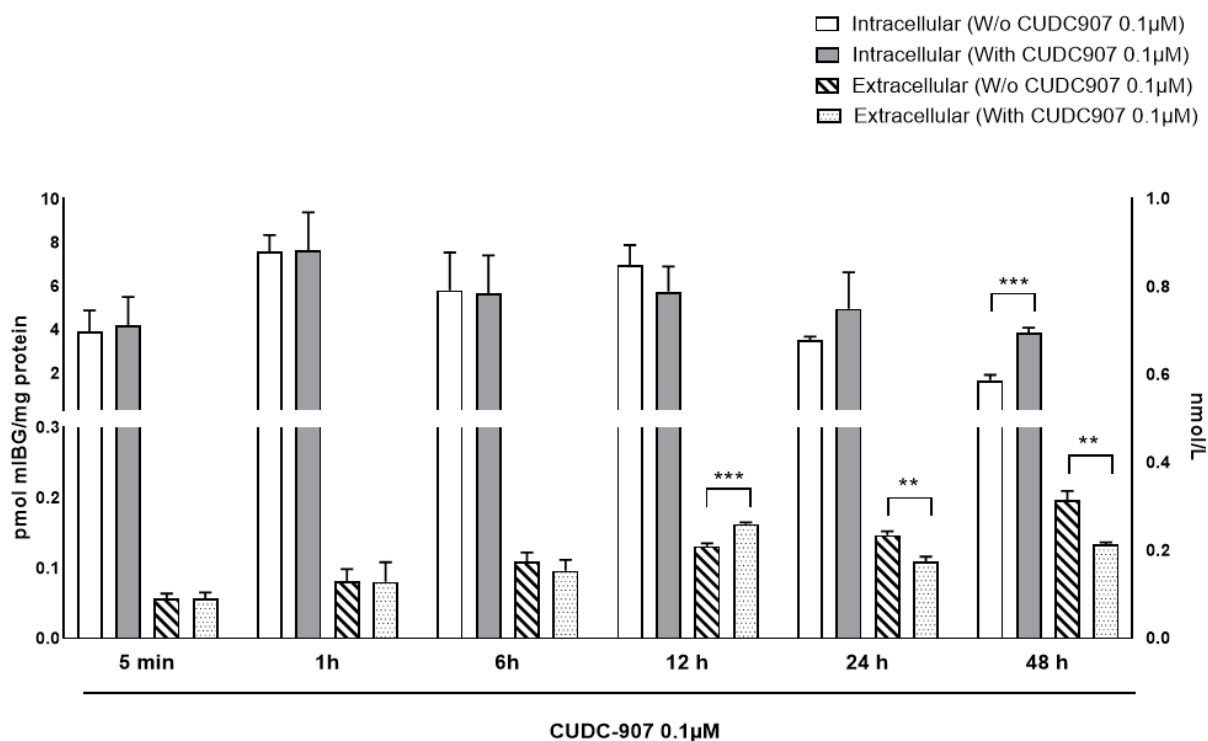
Figure 27 - mIBG stays in IGR-NB8 cells after 12 h of its internalization.
IGR-NB8 cells were incubated with CUDC-907 0.1 µM for 48 h. mIBG 10nM was added to cells for 10 min and then the medium containing the mIBG was removed and replaced by fresh-medium. After 5 min, 1 h, 6 h, 12 h, 24 h and 48 h the medium and the cells were collected separately. Extra- and intracellular mIBG was then extracted through SPE plate and quantified by LC-MS/MS. Results were normalized by a BCA test. The experiments were performed 3 times in duplicates.

Effect of CUDC-907 treatment on the monoamine transporters NET and DAT in IGR-NB8 cells

We then investigated the molecular effect of CUDC-907 in NET and DAT expression. To do so, we analyzed mRNA expression of NET and DAT in IGR-NB8 cells after treatment with CUDC-907 0.1 µM (Figure 28). The results showed that NET mRNA expression is significantly increased compared with non-treated cells (fold change $= 1.763 \pm 0.359$, $p<0.01$). DAT mRNA expression levels were very close to the upper threshold and difficult to dissociate from background, however we still detected a nearly significant increase in DAT mRNA expression (fold change $= 1.608 \pm 0.505$, $p=0.053$) (Figure 29).

NET mRNA expression
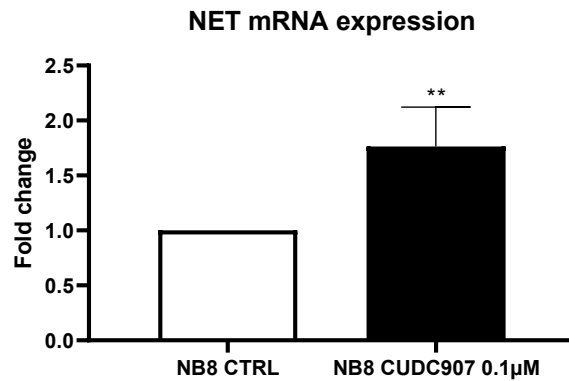
Figure 28 – CUDC-907 increases NET mRNA expression in IGR-NB8 cells.
NET mRNA expression levels in IGR-NB8 cells treated 48 h with CUDC-907 0.1 µM. Results were expressed as fold change compared to the control (non-treated cells). Statistical analysis was performed through unpaired t-test between the control and condition tested. **, $p<0.01$. The experiments were repeated 2 times in duplicates.


DAT mRNA expression
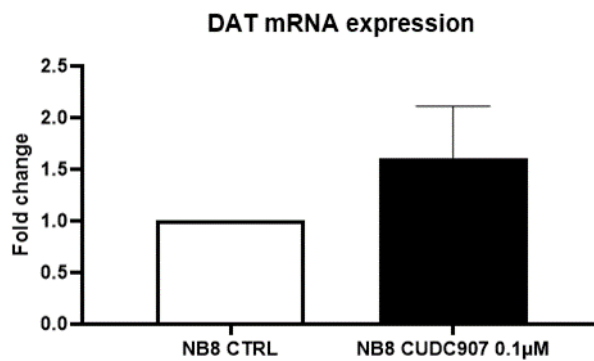
Figure 29 –CUDC-907 increases DAT mRNA expression in IGR-NB8 cells.
DAT mRNA expression levels in IGR-NB8 cells treated 48 h with CUDC-907 0.1 µM. Results were expressed as fold change compared to the control (non-treated cells). Statistical analysis was performed through unpaired t-test between the control and condition tested. The experiments were repeated 2 times in duplicates.

Effect of CUDC-907 on NET and DAT at the protein level was evaluated through immunofluorescence on IGR-NB8 cells (Figure 30 and 31, respectively). Following CUDC-907 treatment we observed an increase in NET and DAT protein expression in IGR-NB8 cells compared to the non-treated cells. Protein expression levels were not analyzed through

immunoblotting because NET protein expression was too low to be detected with a specific antibody.
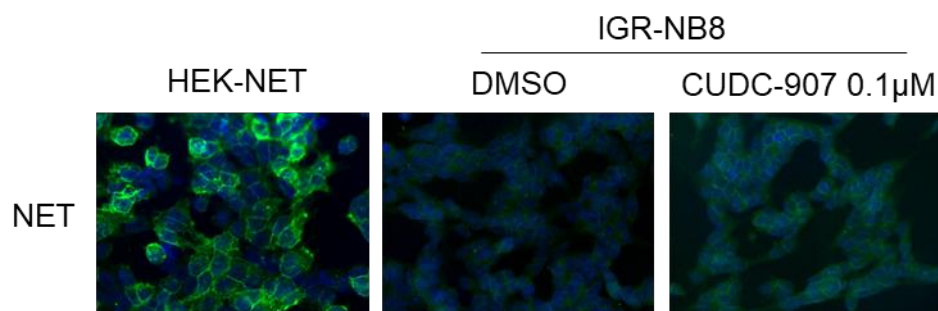
Figure 30 – CUDC-907 increases NET protein levels on IGR-NB8 cells.
IGR-NB8 cells were incubated with CUDC-907 0.1 μM or DMSO for 48 h. Anti-NET antibody staining is revealed in green and DAPI staining is in blue. Pictures were taken by using a Leica DFC 345 FX fluorescence microscope.
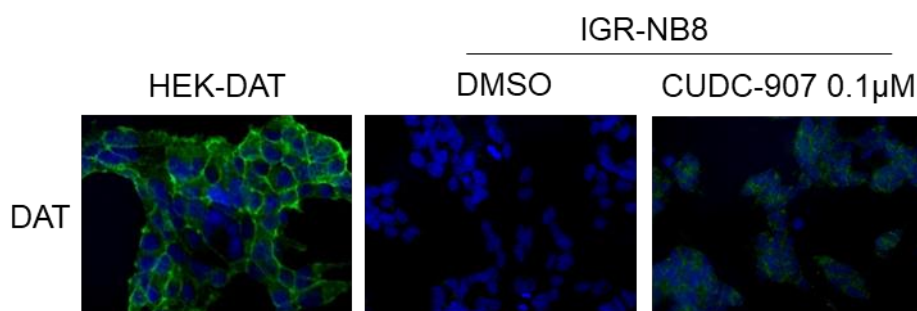
Figure 31 - CUDC-907 increases DAT protein levels on IGR-NB8 cells.
IGR-NB8 cells were incubated with CUDC-907 0.1 μM or DMSO for 48 h. Anti-DAT antibody staining is revealed in green and DAPI staining is in blue Pictures were taken by using a Leica DFC 345 FX fluorescence microscope.

To determine NET and DAT respective contribution to mIBG internalization in IGR-NB8 cells following incubation with CUDC-907, specific inhibitors were used (Figure 32). The inhibitors were applied on the cells at increasing concentrations to determine which concentration achieved complete inhibition of the transporters. The addition of DMI 1 μM, without CUDC-907, nearly completely abolished mIBG internalization (fold change = 0.130 ± 0.060; p = 0.0073). When GBR12935 was added to the cells at the highest concentration used (1 μM), inhibition was around 50% of mIBG internalization, but the change is not significant (fold change = 0.536 ± 0.165; p = 0.5809). When both inhibitors were added at the same time at high concentrations (0.5 μM: fold change = 0.190 ± 0.043; p = 0.0468 and 1 μM: fold change = 0.127 ± 0.064; p = 0.0070), we observed a profile of inhibition similar to DMI-alone treated cells. In the presence of CUDC-907 0.1 μM, DMI reduced by nearly 60% mIBG internalization with the lowest concentration (fold change = 0.421 ± 0.200; p<0.0001), as observed in the absence of CUDC-907. As DMI concentration increases up to 1 μM, mIBG uptake is nearly

completely inhibited (fold change = 0.046 ± 0.019; p<0.0001). When GBR12935 0.5 μM was added to the cells with CUDC-907 0.1 μM, it inhibited 50% of mIBG internalization (fold change = 0.543 ± 0.166; p<0.0001) and at 1 μM it inhibited around 70% (fold change = 0.310 ± 0.142; p<0.0001). The effect of the combination of DMI 0.01 μM and GBR12935 0.01 μM in the presence of CUDC-907 0.1 μM (fold change = 0.484 ± 0.244; p<0.0001) once again looks similar to the profile of inhibition seen with DMI alone, as the combination of DMI 1 μM and GBR12935 1 μM (fold change = 0.028 ± 0.016; p<0.0001). These results suggest that the internalization of mIBG is mainly performed by NET in IGR-NB8 cells.
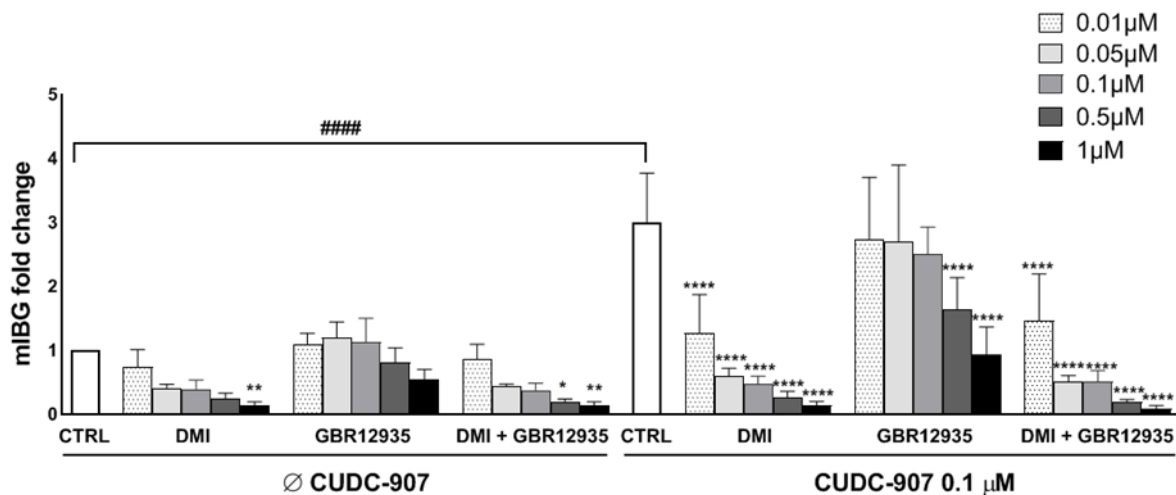
Figure 32 - mIBG seems to be internalized mainly by NET transporters in IGR-NB8.
IGR-NB8 cells were incubated with CUDC-907 0.1 μM for 48 h, DMI, GBR12935 or a combination of both inhibitors with different concentrations (0.01, 0.05, 0.1, 0.5 and 1 μM) and finally mIBG was added. Results were normalized by a BCA test and expressed as fold of increase in mIBG internalization compared with non-treated cells (DMSO). The experiments were repeated 3 times in duplicates. Statistical analysis was performed through two-way ANOVA between the respective control (without CUDC-907 or with CUDC-907 0.1 μM) and each condition tested. *, p<0.05; **, p<0.01; ****, p<0.0001. Statistical analysis between controls with and without CUDC-907 were performed through unpaired t-test. ####, p<0.0001.

To further confirm that NET is the main transporter responsible for mIBG internalization in IGR-NB8 cells treated with CUDC-907 we used siRNA technology to knockdown NET and/or DAT (Figure 33). When we knocked down NET in the presence of CUDC-907 we observed a near 40% decrease in mIBG internalization (fold change = 0.578 ± 0.177; p<0.05) showing a reversal of the effect of CUDC-907 treatment, similar to the treatment with DMI. On the other hand, when we knocked down DAT we obtained no visible effect on mIBG internalization following treatment with CUDC-907 (fold change = 0.961 ± 0.194, p=0.798), suggesting that DAT has no effect on mIBG internalization in IGR-NB8 cells, similar to the treatment to the GBR12935 treatment. Finally, when we knocked down both NET and DAT we observed nearly the same effect as when we only knocked down NET, with a near 30% decrease in

internalization, although this decrease was not significant (fold change = 0.692 ± 0.228; p=0.096).
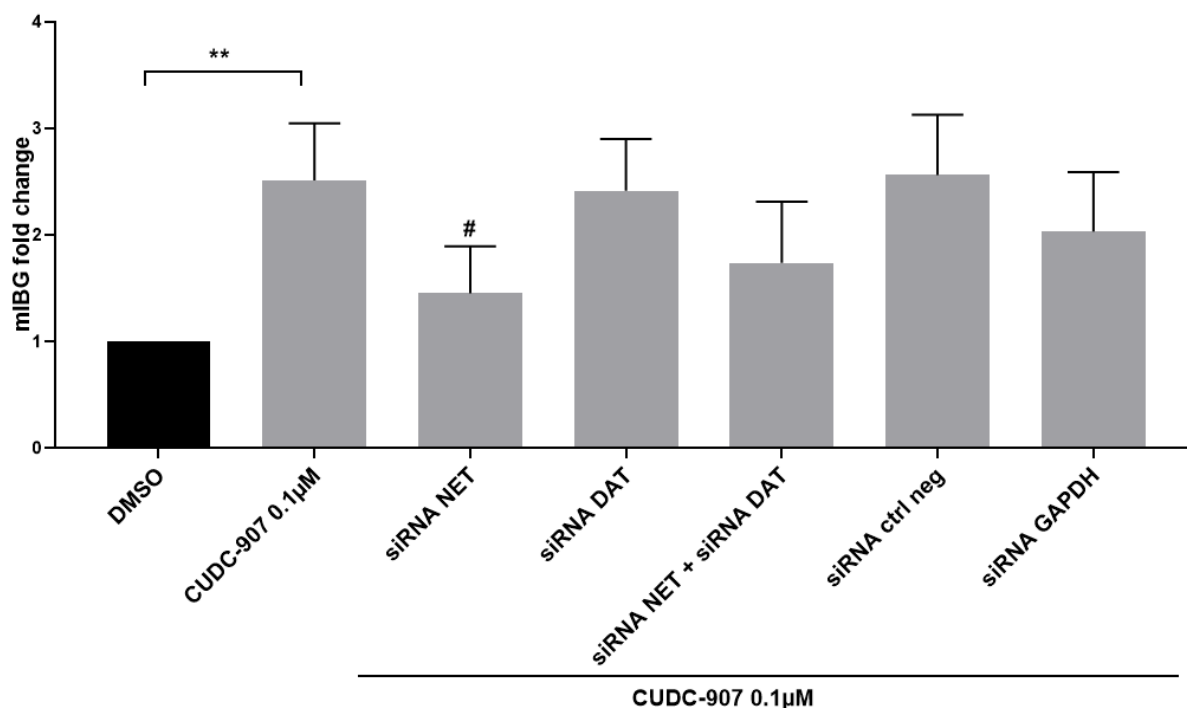
Figure 33 – Knockdown of NET expression decreases mIBG internalization in IGR-NB8 cells treated with CUDC-907 0.1 μM.
mIBG internalization after knockdown of NET and/or DAT in IGR-NB8 cells treated with CUDC-907 0.1 μM. mIBG internalization following NET and/or DAT knockdown and CUDC-907 treatment. Results were normalized by a BCA test. Statistical analysis was performed through unpaired t-test using either DMSO (*) or CUDC-907 (#) as control and comparing with each of the conditions tested. **, p<0.01; #, p<0.05. The experiments were repeated 3 times in duplicates.

Effect of CUDC-907 treatment on mIBG internalization in PC-12 cells

In order to assess that our observation were not specific for only a given cell line, we also tested the effect of CUDC-907 on mIBG internalization in a PHEO cell line, PC-12 cells (Figure 34). PC-12 cells were incubated with DMSO or CUDC-907 0.5 μM for 48 h. CUDC-907 0.5 μM (fold change = 1.153 ± 0.088, p<0.05) slightly but significantly increased mIBG internalization compared to the control.
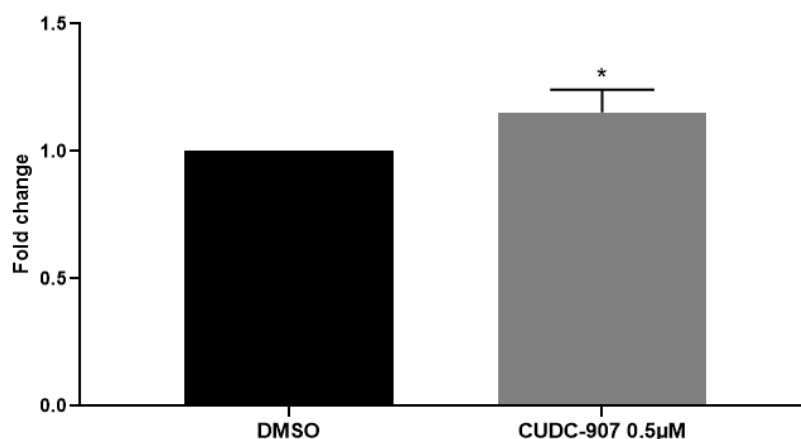
Figure 34 - CUDC-907 0.5 μM increases mIBG internalization in PC-12 cells.
PC-12 cells were incubated with CUDC-907 0.5 μM for 48 h and then with mIBG. Intracellular mIBG was then extracted through SPE and quantified by LC-MS/MS. Results were normalized by a BCA test and expressed as fold-change in mIBG internalization compared with non-treated cells (DMSO). Statistical analysis was performed through unpaired t-test between the control and condition tested. *, $p < 0.05$. The experiment was performed at least 3 times in duplicates.

The cell viability of the PC-12 cells treated with CUDC-907 was evaluated via trypan blue assay to demonstrate that the presence of the CUDC-907 0.5 μM was not toxic to the cells (Figure 35). Results showed no cell viability differences between the DMSO-treated cells and the CUDC-907-treated cells at 0.5 μM.
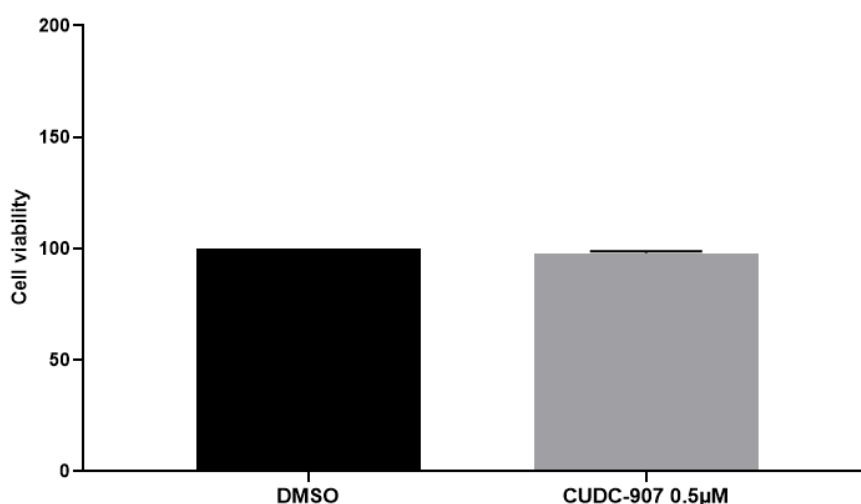
Figure 35 – The cell viability is not affected by the presence of CUDC-907 0.5 μM in PC-12 cells.
PC-12 cells were incubated with CUDC-907 0.5 μM for 48 h and then a trypan blue assay was performed. The experiment was performed once in triplicate.

Effect of decitabine, DNMT inhibitor on mIBG internalization in a NB cell line

Taelman *et al*. found that two DNMT inhibitors, including decitabine, are able to increase the somatostatin receptor agonist ^{68}Ga-DOTATOC uptake in human pancreatic neuroendocrine

57

tumor cells (BON-1).[81] In the same way, we tested decitabine in IGR-NB8 cells to evaluate its effect in mIBG internalization (Figure 36). Our results demonstrated that decitabine had no effect on mIBG internalization when compared with control (fold change: 0.2 μM = 1.066 ± 0.255; 1 μM = 0.928 ± 0.137; 2 μM = 0.801 ± 0.353).
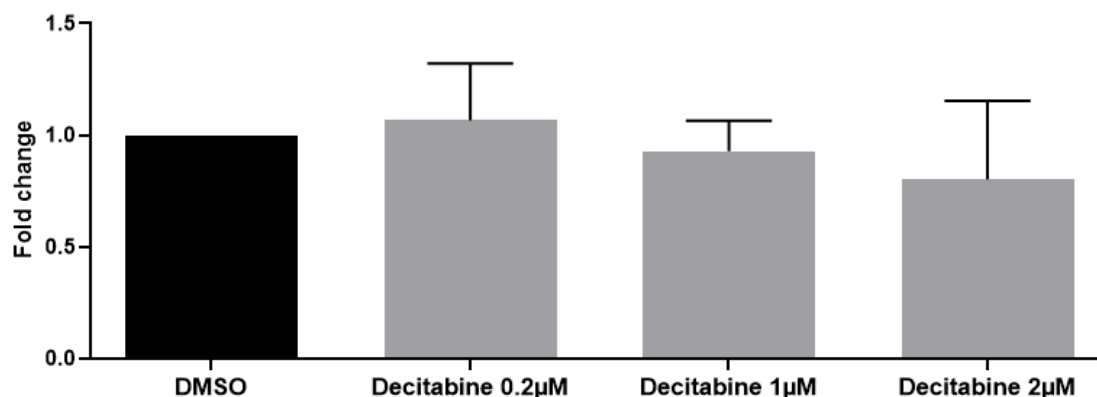
Figure 36 – Decitabine has no effect on mIBG internalization in IGR-NB8 cells.
IGR-NB8 cells were incubated with decitabine at different concentrations for 48 h and then with mIBG. Intracellular mIBG was then extracted through SPE and quantified by LC-MS/MS. Results were normalized by a BCA test and expressed as fold change in mIBG internalization compared with non-treated cells (DMSO). Statistical analysis was performed through unpaired t-test between the control and condition tested. All the experiments were performed at least 3 times in duplicates.

Effect of BGT226 on mIBG internalization in IGR-NB8 cells

CUDC-907 is a dual inhibitor, acting both on HDAC and the PI3K pathway. For that reason, we investigated whether the increase of mIBG was due to the HDAC inhibition or due to the PI3K inhibition. To do this, we selected a specific PI3K inhibitor, BGT226, and we compared the effect of CUDC-907 and BGT226 on mIBG internalization. After BGT226 treatment, we observed an increase of mIBG internalization in a dose-dependent manner and also that BGT226 50 nM increases mIBG internalization by approximately 2.5 times when compared with non-treated cells (fold change = 2.481 ± 0.468, p<0.01) (Figure 37).
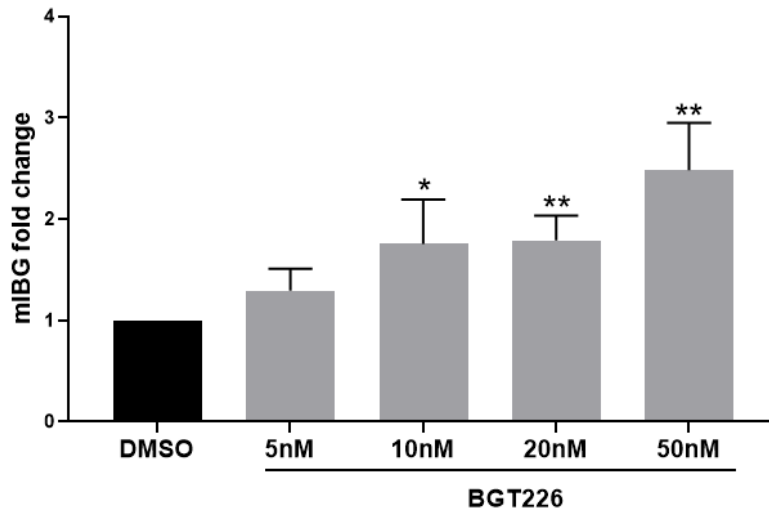
Figure 37 – BGT226 increases mIBG internalization in IGR-NB8 cells in a dose-dependent manner.
IGR-NB8 cells were incubated with BGT226 at increasing concentrations for 48 h and then with mIBG. Results were normalized by a BCA test and expressed as fold of increase in mIBG internalization compared with non-treated cells (DMSO). Statistical analysis was performed through unpaired t-test between the control and condition tested. *, $p<0.05$; **, $p<0.01$.

We also compared CUDC-907- and BGT226-treated IGR-NB8 cells and we found that the difference between both inhibitor activity on mIBG internalization was not significant (fold change: CUDC-907 vs BGT226 = 0.807 ± 0.311), suggesting that CUDC-907 effects on mIBG internalization might be mostly due to PI3K inhibition (Figure 38).
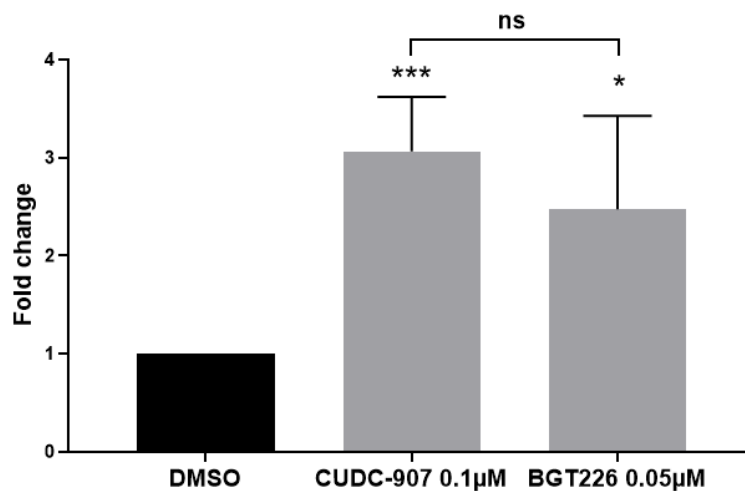
Figure 38 – Difference between IGR-NB8 cells treated with CUDC-907 and BGT226 on mIBG internalization is not significant.
IGR-NB8 cells were incubated with either CUDC-907 or BGT226 for 48 h and then with mIBG. Results were normalized by a BCA test and expressed as fold of increase in mIBG internalization compared with non-treated cells (DMSO). Statistical analysis was performed through unpaired t-test between CUDC-907- and BGT226-treated cells. *, $p<0.05$; ***, $p<0.001$.

59

Effect of BGT226 treatment on the monoamine transporters NET and DAT in IGR-NB8 cells

Finally we evaluated the effect of BGT226 on NET and DAT in IGR-NB8 cells. Using siRNA, we performed the knockdown of NET and/or DAT (Figure 39). The knockdown of NET showed a 50% decrease in mIBG internalization after BGT226 treatment (fold change = 0.542 ± 0.132; p<0.01). Inversely, when we knocked down DAT we observed no visible effect on mIBG internalization (fold change = 1.003 ± 0.075). Lastly, when we knocked down both NET and DAT we observed the same effect as with NET knockdown (fold change = 0.502 ± 0.093; p<0.01). These results suggest that BGT226 has an effect on NET and consequently mIBG internalization and no effect on DAT mIBG internalization.
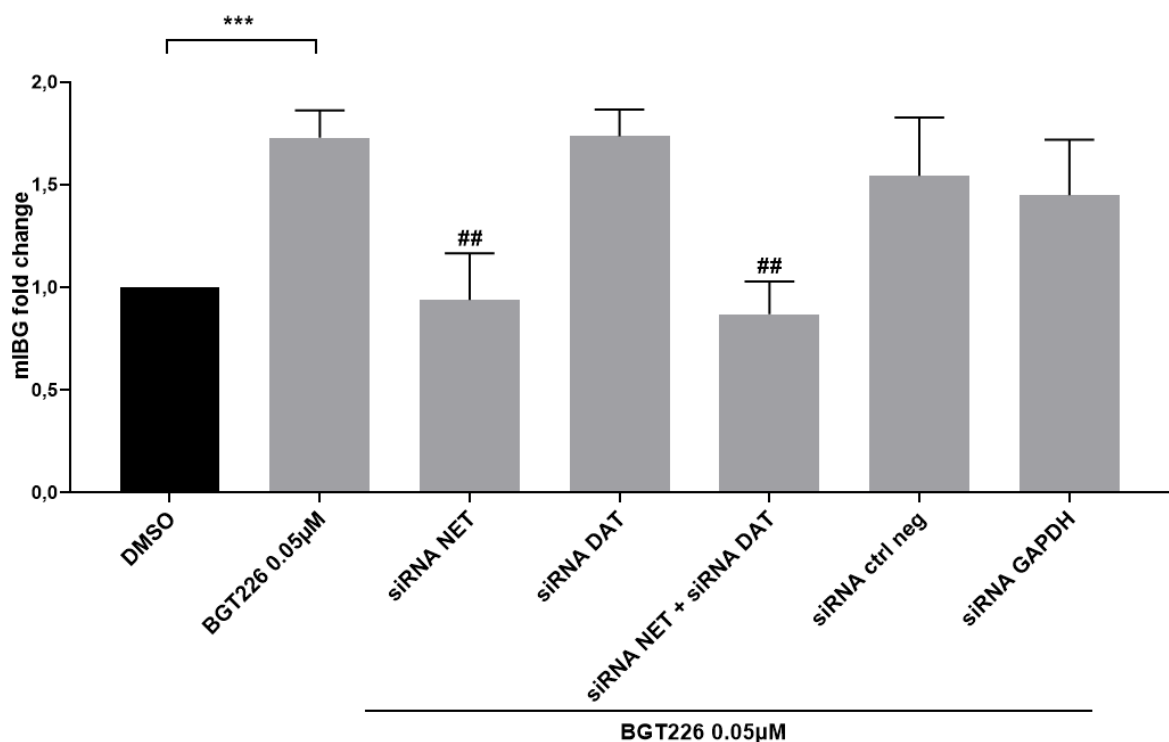

Figure 39 - Knockdown of NET expression decreases mIBG internalization in IGR-NB8 cells treated with BGT226 0.05 μM.
mIBG internalization following NET and/or DAT knockdown and BGT226 treatment. Results were normalized by a BCA test. Statistical analysis was performed through unpaired t-test using either DMSO (*) or BGT226 (#) as control and comparing with each of the conditions tested. ***, p<0.001; ##, p<0.01. The experiments were repeated 3 times in duplicates.

VS-5584 and rapamycin treatment increase mIBG internalization in a neuroblastoma cell line

PI3K, Akt and mTOR inhibitors and their effect on mIBG internalization were tested on IGR-NB8 cells (Figure 40). IGR-NB8 cells were incubated with different inhibitors for 48 h. VS-

5584, a PI3K/mTOR inhibitor, (VS-5584 vs DMSO fold change = 1.506 ± 0.109, $p<0.001$) and rapamycin, a mTOR inhibitor, (rapamycin vs DMSO fold change = 1.338 ± 0.098, $p<0.001$) significantly increased mIBG internalization compared to the control. On the other hand, MK2206, an Akt inhibitor, (MK2206 vs DMSO fold change = 0.723 ± 0.126, $p<0.01$) significantly decreased mIBG internalization compared to the control.
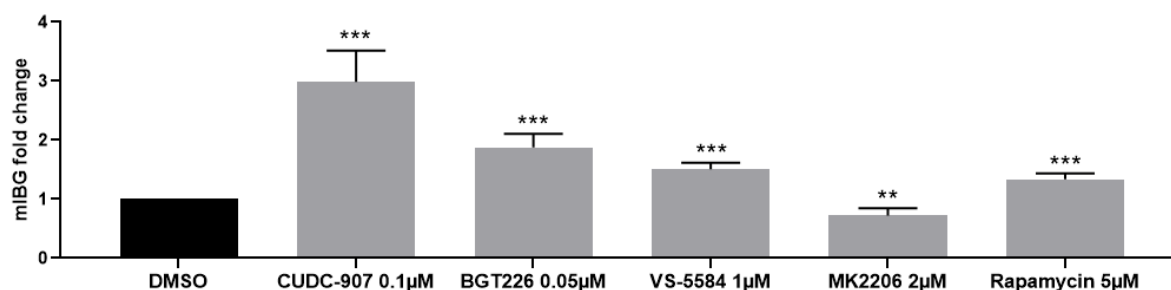
Figure 40 – VS-5584 and rapamycin increase mIBG internalization in IGR-NB8 cells.
IGR-NB8 cells were incubated with PI3K, Akt and mTOR inhibitors for 48 h and then with mIBG. Results were normalized by a BCA test and expressed as fold of increase in mIBG internalization compared with non-treated cells (DMSO). Statistical analysis was performed through unpaired t-test between control and condition tested. **, $p<0.01$; ***, $p<0.001$.

To demonstrate that the presence of the different inhibitors was not toxic to the cells we evaluated the cell viability through a trypan blue assay (Figure 41). Results showed no cell viability differences between the DMSO-treated cells and the inhibitor-treated cells at the concentrations used.
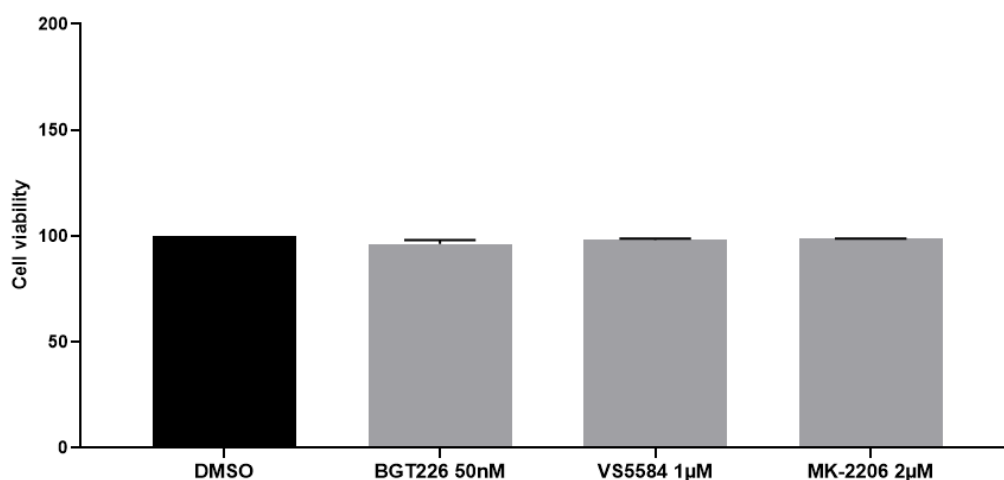
Figure 41 – The cell viability is not affected by the presence of the different inhibitors in IGR-NB8 cells.
IGR-NB8 cells were incubated with PI3K, Akt and mTOR inhibitors for 48 h and then a trypan blue assay was performed. The experiment was performed once in triplicate.

Effect of CUDC-907 on the ^{123}I-mIBG internalization *in vivo*

Effect of CUDC-907 on the ^{123}I-mIBG internalization *in vivo*

To evaluate the *in vivo* effects of CUDC-907, Dr. Rosalba Mansi (Laboratory of Prof. Melpomeni Fani) used female athymic nude-Foxn1^{nu}/Foxn1^{+} mice subcutaneously implanted with IGR-NB8 cells. After one month, with a tumor size ranging between 120-200 mm^3, the experiments started dividing the mice in three groups. The group A was treated with CUDC-907 at 10 mg/Kg, the group B with 5 mg/Kg and the group C with vehicle (10% DMSO in corn oil), given orally for 5 days (Figure 42).
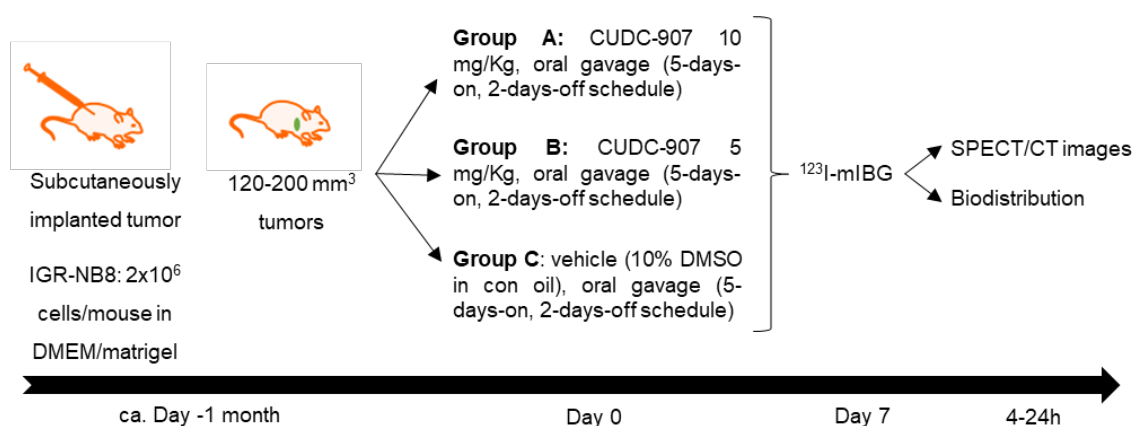
Figure 42 – Scheme of the experimental design for the *in vivo* studies.

The body distribution of ^{123}I-mIBG was evaluated both at 4 h p.i. (Table 5) and 24 h p.i. (Table 6). After 4 h, the group A and group B showed no significant differences in the accumulation of ^{123}I-mIBG in most of the organs and tumor except for the gallbladder (18.22 ± 5.49 vs 8.37 ± 2.19 %IA/g for the group A and B, respectively, $p<0.01$). The gallbladder is the organ with highest internalization of ^{123}I-mIBG at 4 h p.i. due to the physiological excretion pathway. Moreover, the administration of the two different doses of CUDC-907 in group A and B do not significantly impact the tumor uptake of ^{123}I-mIBG (3.19 ± 1.20 vs 2.24 ± 0.40 %IA/g for the group A and B, respectively, $p=0.1$). This result indicated that the 5 mg/Kg treatment, under the experimental conditions used in this study, is to be preferred as it demonstrated that the 2-fold lower dose of CUDC-907 has the same impact in the upregulation of the monoamine transporter leading to similar accumulation of ^{123}I-mIBG. For both treated, groups the tumor internalization of ^{123}I-mIBG is higher compared to the vehicle (3.19 ± 1.20 vs 2.24 ± 0.40 vs 0.98 ± 0.35, for the group A, B and C, respectively, $p<0.01$). At the 24 h p.i., the highest accumulation of ^{123}I-mIBG was in the adrenal glands (5.62 ± 0.94 vs 6.60 ± 1.18 %IA/g for the group A and B, respectively) followed by the tumors (3.06 ± 0.68 vs 2.71 ± 0.64 %IA/g for the

group A and B, respectively, p=0.5). Additionally, a background clearance was observed in most organs when compared to the 4 h p.i. profile. These results correlate with our previous *in vitro* results where we demonstrated an increase of mIBG internalization after CUDC-907 treatment in IGR-NB8 cells.

Table 5 – Biodistribution data of ^{123}I-mIBG in IGR-NB8 xenografts at 4 h p.i.

	^{123}I-mIBG (IGR-NB8 xenografts)		
	4 h p.i.		
	CUDC-907 10 mg/Kg° (n=8)	**CUDC-907 5 mg/Kg* (n=5)**	**Vehicle[§] (n=3)**
Blood	0.76 ± 0.14	0.64 ± 0.06	0.55 ± 0.22
Heart	6.27 ± 1.76	6.65 ± 0.80	4.12 ± 0.96
Lung	3.43 ± 0.52	3.08 ± 0.38	3.19 ± 0.84
Liver	4.02 ± 0.42	3.67 ± 0.54	3.42 ± 0.51
Pancreas	2.81 ± 0.47	2.40 ± 0.23	2.07 ± 0.39
Spleen	2.80 ± 0.43	2.11 ± 0.56	2.64 ± 0.92
Stomach	3.32 ± 0.44	2.94 ± 0.25	4.56 ± 2.03
Intestine	5.55 ± 0.96	4.55 ± 0.40	3.56 ± 0.45
Adrenal	7.49 ± 1.30	7.40 ± 0.77	6.97 ± 0.92
Kidney	2.21 ± 0.47	1.76 ± 0.26	1.47 ± 0.22
Muscle	1.21 ± 0.27	1.10 ± 0.15	1.28 ± 0.27
Bone	1.02 ± 0.17	0.98 ± 0.16	0.89 ± 0.11
IGR-NB8 tumor	**3.19 ± 1.20 (p=0.1)**	**2.24 ± 0.40**	**0.98 ± 0.35 (p<0.01)**
Salivary gland	9.28 ± 1.70	8.52 ± 0.58	7.27 ± 1.19
Gall bladder	18.22 ± 5.49 (p<0.01)	8.37 ± 2.19	

* 10% DMSO in corn oil; °sum of the two treatments with the same dose (10 mg/kg in 30% Polyethylene glycol or in 10% DMSO in corn oil); [§] 30% Polyethylene glycol. For all mice: oral gavage, 100-200 μL, 5 days + 2 days drug free. ^{123}I-MIBG: 2-4 MBq/100 μL.

Table 6 - Biodistribution data of ^{123}I-mIBG in IGR-NB8 xenografts at 24 h p.i.

	^{123}I-mIBG (IGR-NB8 xenografts)		
	24 h p.i.		
	CUDC-907 10 mg/Kg* (n=4)	**CUDC-907 5 mg/Kg* (n=4)**	**Vehicle[§] (n=2)**
Blood	0.12 ± 0.03	0.11 ± 0.04	0.30
Heart	1.20±0.39	1.09 ± 0.37	0.67 ± 0.16
Lung	0.45±0.09	0.44 ± 0.09	0.28 ± 0.04

Liver	0.58±0.16	0.57 ± 0.14	0.33 ± 0.03
Pancreas	0.42±0.09	0.36 ± 0.04	0.30 ± 0.06
Spleen	0.71±0.19	0.57 ± 0.24	0.56 ± 0.18
Stomach	1.63±0.19	1.56 ± 0.29	1.02 ± 0.20
Intestine	1.47±0.40	1.23 ± 0.37	0.63 ± 0.28
Adrenal	5.62±0.94	6.60 ± 1.18	8.07 ± 2.82
Kidney	0.40±0.08	0.42 ± 0.09	0.27 ± 0.03
Muscle	0.21±0.05	0.18 ± 0.02	0.15 ± 0.00
Bone	0.25±0.09	0.19 ± 0.03	0.16 ± 0.04
IGR-NB8 tumor	**3.06±0.68 (p=0.5)**	**2.71 ± 0.64**	**1.66 ± 0.05 (p=0.09)**
Salivary gland	1.69±0.61	1.74 ± 0.42	0.94 ± 0.25
Gall bladder	1.26±0.25	1.12 ± 0.54	0.78

* 10% DMSO in corn oil; § 30% Polyethylene glycol, the mouse was injected with 18 MBq and imaging was acquired at 4 h and 24 h p.i. Biodistribution was performed at 24 h p.i. + mouse used for imaging at 24 h p.i. without any treatment. P-values are calculated compared to the 5 mg/kg group.

A representative SPECT/CT images for a mouse of each group (group A, group B and C) were acquired 4 h (Figure 43) and 24 h (Figure 44) after injection of ^{123}I-mIBG (13-17 MBq/100 μL). The same could be imaged at 4 h and 24 h allowing a clear visualization of the radiotracer uptake over time. At 4 h p.i. an intense ^{123}I-mIBG accumulation in the gallbladder, but also in the intestine was observed, independently of CUDC-907 treatment regimen (10 mg/Kg or 5 mg/Kg) compared to the vehicle (Figure 43). After 24 h p.i there is a complete background clearance, except for the adrenal glands, as well as the tumors, confirming the biodistribution data. Finally, the tumor ^{123}I-mIBG accumulation stays high and constant after 24 h resulting in a great tumor to background ratio (Figure 44).
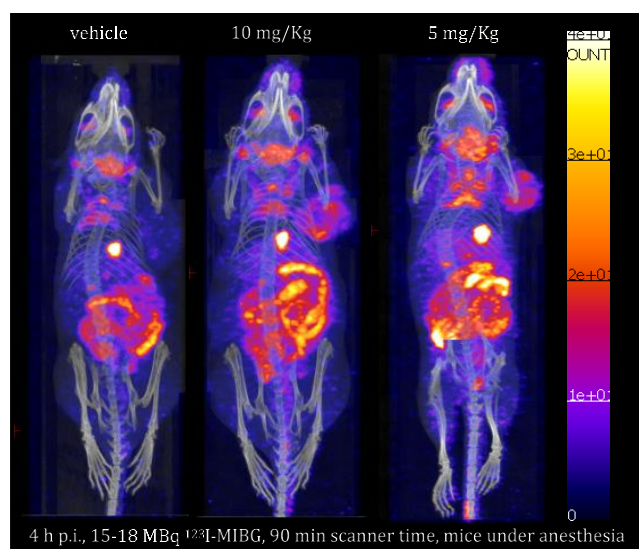
Figure 43 - SPECT/CT images after 4 h p.i. of ^{123}I-MIBG, using different doses of CUDC-907.

Female athymic nude-Foxn1^{nu}/Foxn1^{+} mice injected with IGR-NB8 cells were treated with vehicle (10% DMSO in corn oil) or CUDC-907 (10 mg/Kg or 5 mg/Kg) for 5 consecutive days and then 2 days off. Then mice were treated with Irenat (120 mg/Kg) before ^{123}I-mIBG injection. After 4 h p.i. SPECT/CT images were taken on anesthetized mice. The intensity of ^{123}I-mIBG accumulation was measured and intensity was determined from least intense (blue shades) to most intense (yellow shades).
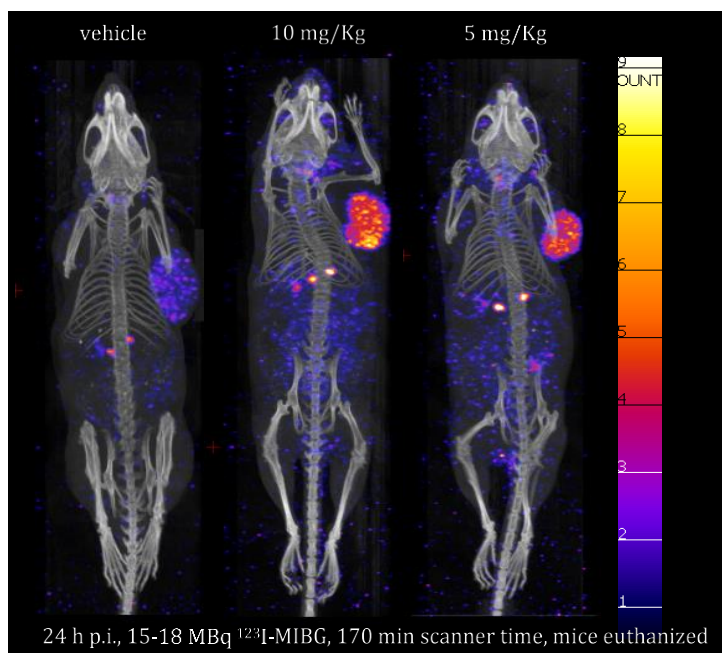
Figure 44 - SPECT/CT images after 24 h p.i. of ^{123}I-MIBG, using different doses of CUDC-907.
Female athymic nude-Foxn1^{nu}/Foxn1^{+} mice injected with IGR-NB8 cells were treated with vehicle (10% DMSO in corn oil) or CUDC-907 (10 mg/Kg or 5 mg/Kg) for 5 consecutive days and then 2 days off. Then mice were treated with Irenat (120 mg/Kg) before ^{123}I-mIBG injection. After 24 h p.i. SPECT/CT images were taken on euthanized mice. The intensity of ^{123}I-mIBG accumulation was measured and intensity was determined from least intense (blue shades) to most intense (yellow shades).

Discussion

Metastatic neuroendocrine tumors require difficult therapies and PHEO and NB are no exception. Indeed, the available methods used to treat metastatic PHEO and NB ideally involve the surgical resection of the tumor mass, however, the tumor and/or the metastasis require to be reduced through chemotherapy and/or radiotherapy previously. In addition, if the tumor is especially aggressive, higher doses of chemicals and/or radiation are needed.[11, 92] Radiolabeled analogs such as mIBG have been in use for at least 40 years as alternatives to the classical methods described.[93] mIBG has long been believed to be internalized exclusively by NET. However, the molecular mechanism behind the internalization of mIBG is still controversial. Here we demonstrated, using PHEO tumor samples from patients of a sporadic origin, there is a clear lack of correlation between NET protein expression and positive-mIBG internalization (Figure 15). For this reason, we found relevant to explore the possibility that other monoamine transporters, such as DAT, OCT1-3 and PMAT might play a part in mIBG internalization, instead of exclusively NET. In this line, our group and others, such as van Berkel *et al.*, have made efforts to better understand the process of mIBG internalization.[94] Glowniak *et al.* showed mIBG was not internalized by neither DAT nor SERT in green monkey kidney cells, CV-1 cells. However, Glowniak and colleagues employed DAT and SERT from bovine and rat origin respectively.[90]

As shown, HEK-DAT cells showed very promising results, with a great increase in mIBG internalization (Figure 16). For the first time, we demonstrated that human DAT was also able to internalize mIBG in a similar extent to NET, although with a lower affinity (Figure 18 and 19). On the other hand, HEK cells stably transfected with OCT1-3 and PMAT did not present significant mIBG internalization. In our studies, SERT was not considered for its low affinity for NE, demonstrated by Eshleman *et al.*, and possibly mIBG, since mIBG is an analog of NE.[95] Streby and colleagues suggested that, for most mIBG internalization and best therapy outcome, the use of a combination therapy to increase NET expression is essential. This increase could be induced pharmacologically by the regulation of epigenetic modifications that modulate gene expression, using HDACi, for example.[49] Regarding this approach, More *et al.* described that 5 μM of vorinostat is able to increase NET mRNA and protein levels in two different NB cell lines, Kelly and SH-SY-5Y.[69] Furthermore, they demonstrated an increase by 4 and 2.5 times in mIBG internalization following the addition of 5 μM of vorinostat in Kelly and SH-SY-5Y, respectively. Additionally, *in vivo* studies were also done to prove that

66

NET protein levels and mIBG internalization were enhanced in nude mice with NB xenografts treated with vorinostat compared to untreated mice.[69] Other HDACi that we used in this project were also tested previously by other groups. Valproate at 5 mM was tested by Wang *et al.* in SK-N-AS cells, a NB cell line, and they found an increase in DAT mRNA and protein expression after 24 h of treatment.[96] Green *et al.* also tested valproate and butyrate, both at 5 mM during 24 h, in SK-N-AS and they observed an increase in both DAT mRNA and protein levels.[70] Green *et al.* also tested valproate at 1 mM, butyrate at 1 mM and TSA at 600 nM in rat dopaminergic cells (N27) and promisingly they found an increase of 3 to 10 times of DAT mRNA expression. They also observed an increase of 50% of DAT protein levels through the increase of H3 acetylation after the treatment of N27 cells with valproate at 1 mM.[77] However, the latter study by Green *et al.* was not done in neuroendocrine tumor cells and in addition the study was performed in rat cells. Additionally, Taelman *et al.* showed, using HDACi, an increase in somatostatin receptor 2 mRNA expression and protein levels and correlated this with an increase of ^{68}Ga-DOTATOC uptake in a pancreatic neuroendocrine tumor cell line (BON-1).[81] In this way, we explored the use of HDACi to increase the expression of the monoamine transporters involved in mIBG internalization and consequently improve mIBG imagery and therapy in NB. The novelty of our study stems from the use of a library of HDACi in IGR-NB8 cells, a human NB cell line. From this screening, we found some promising candidates (mocetinostat, PCI-24781, CUDC-907 and sodium-4-P) that could be further explored in future studies to increase NET and/or DAT expression as a means to further improve mIBG cell internalization. Interestingly, in our experimental conditions, vorinostat did not induce an increase in mIBG internalization. However, this may be the result of the use of a different cell line than the one used in More *et al.*'s studies.[69] Indeed, this group used Kelly and SH-SY-5Y cells, two different NB cell lines, whereas we used IGR-NB8, a different NB cell line. This discrepancy might originate from the heterogeneous nature of neuroendocrine tumors, as reported in the introduction. Additionally in our experimental conditions, valproate, sodium-4-P and TSA did not have an effect on mIBG internalization. This may be due to DAT's low expression compared to NET in IGR-NB8 cells and therefore the effect of the HDACi on DAT upregulation might not be enough to produce a measurable change in mIBG internalization.

We then focused our attention on CUDC-907, a PI3K and HDAC dual-inhibitor, both *in vitro* and *in vivo*, and observed the positive effects on both monoamine transporter expression and also, and most importantly, mIBG internalization. CUDC-907 is already being used in clinic as

an anticancer agent, inhibiting proliferation of cancer cells, inducing DNA damage, cell cycle arrest and apoptosis in breast cancer cells, and also working synergistically with other anticancer agents for the treatment of leukemia, as shown in some very recent studies.[97, 98] Additionally, CUDC-907's HDACi effects are seen in both class I and class II HDACs and have already been demonstrated to downregulate known deregulated human oncogenes, such as *Myc*, as shown by Sun and colleagues.[99] Our *in vitro* results demonstrated that treatment of IGR-NB8 cells with CUDC-907 significantly increased mIBG internalization (Figure 21). Also, we observed that CUDC-907 treatment also increased NET and DAT, both at the mRNA (Figures 28 and 29) and protein levels (Figure 30 and 31). To extend this unexpected finding to other cell lines, we also tested CUDC-907 in the PC-12 PHEO cell line. We found that CUDC-907 treatment also significantly increased mIBG internalization in PC-12 cells, although this increase was more modest (Figure 34). These results suggest that the combination of CUDC-907 with mIBG can be very useful to improve the imagery and therapy used for NB and PHEO. In future experiments, we will further explore the effects of this increase in mIBG internalization in PC-12 cells and attempt to determine if they are due to an increase in NET and/or DAT expression.

The role of NET and DAT in mIBG internalization is not clearly established. Indeed, our own results were conflicting. Our *in vitro* studies using NET- and DAT-specific inhibitors (Figure 32) and the inhibition of the expression of NET and/or DAT via the use of siRNA (Figure 33) suggest that NET is the main player in the internalization of mIBG in IGR-NB8 cells. Our results favor a minor role in mIBG internalization for DAT with IGR-NB8 cells, although this might be explained by the low levels of DAT expression in these cells, as seen upon qPCR analysis (Table 4). Still, the heterogeneity of tumors might include NB or PHEO tumors that present higher expression of DAT and therefore, in those cases, mIBG internalization could be performed via DAT, as we showed in our DAT-transfected HEK cells. Among the NB cell lines that we screened, LAN-1 cells might also be an interesting cell line to study since it is the one that presented the highest levels of DAT mRNA expression among those we tested and also presented high levels of NET (Table 4). This cell line and others might be further explored regarding the role of DAT in mIBG internalization. Additionally, the fact that there are no human PHEO cell lines is also an obstacle in our studies. At present, two possibilities to study PHEO cells *in vitro* are possible, the use of primary PHEO tumor cultures or other species' cell lines, such as the rat PC-12, with the problem of translation of the results from rat to human. However, using primary cultures has its own problems since PHEO tumor samples are quite

rare and their amount is limited when available, and cell amplification is impossible since there are not growing when cultured.

Another point we explored was the storage of mIBG after its internalization by IGR-NB8 cells. In the literature, two main hypothesis exist, one suggesting that mIBG is stored in neurosecretory granules through VMAT1 and VMAT2, mainly in PHEO tumors that present many vesicles, and the other suggesting that mIBG is kept in the cytoplasm or in mitochondria upon internalization, mainly in NB tumors that present a low amount of vesicles. This difference in storage is also believed to be distinct depending on the type of transport through which mIBG is internalized, either active or passive, as described before. The different transports occur in different types of cells, depending if the cells are able to synthesize NE or not.[49, 62, 64] PC-12 cells have since long been shown to present intracellular vesicles, therefore indicating the presence of these neurosecretory granules in PHEO cells.[100] Still, in our study, we did not focus on the intracellular localization of mIBG but we explored the duration of mIBG sequestration, with or without the presence of our main candidate, CUDC-907 (Figure 27). With our studies, we observed that mIBG intracellular content remains unchanged in IGR-NB8 cells up to 12 h after incubation with mIBG and 48 h of CUDC-907 pre-treatment. In addition we noticed that when cells were constantly treated with CUDC-907 after mIBG incubation displayed a higher intracellular mIBG content than non-CUDC-907-treated cells between 24 h and 48 h. This suggests that CUDC-907 may have a positive effect on mIBG accumulation even after mIBG incubation. In the case of the conditions 5 min, 1 h and 6 h the difference was less pronounced perhaps due to degradation of CUDC-907. This suggests that in case of hypothetical clinical trial for radionuclide therapy, patients should be constantly treated concomitantly with I^{131}-mIBG and CUDC-907.

Aside from the HDACi, in the literature we find the use of a different class of epigenetic regulating-inhibitors, the DNMT inhibitors. DNMT inhibitors, such as decitabine and azacitidine, act on DNMT enzymes and inhibit methylation of specific promoter regions, thus enhancing gene expression. Taelman *et al.* described the use of these inhibitors to induce somatostatin receptor subtype 2 expression and thus improve ^{68}Ga-DOTATOC imaging and therapy in human pancreatic neuroendocrine tumor cells, BON-1 cells.[81] In the present study, we explored the use of decitabine to improve mIBG internalization in IGR-NB8 cells. In our experimental conditions, we observed no significant changes in mIBG internalization, despite having tested different concentrations (Figure 36). Still, we only tested decitabine's effect on a single NB cell line, and therefore, in the future, we could test different DNMT inhibitors, such

as azacitidine, and explore its effects on mIBG internalization on multiple cell lines, such as LAN-1 and PC-12 for example.

Since CUDC-907 is a PI3K inhibitor in addition to being a HDACi, we considered the option of investigating PI3K/Akt/mTOR inhibitors and their effect on mIBG internalization, to better understand the mechanism through which CUDC-907 increases mIBG internalization. PI3K/Akt/mTOR inhibitors or drugs targeting the PI3K pathway have been studied in the context of different types of cancer, including studies in NB cells.[84, 86, 101, 102] An *in vivo* study has also been published regarding the use of a dual PI3K/mTOR inhibitor for its antitumoral activity in PHEO.[103] Among the studies on NB, rapamycin and VS-5584, a mTOR inhibitor and a PI3K inhibitor, respectively, were shown to inhibit proliferation and induce either autophagy or cell cycle arrest in NB cells, *in vitro* and both *in vitro* and *in vivo*, respectively for rapamycin and VS-5584.[84, 86] Despite this, no studies have been performed regarding the use of these inhibitors and the increase of mIBG internalization in NB tumors. However, Figlewicz *et al.* and Apparsundaram *et al.* have shown that NET is regulated by insulin. In their study, Apparsundaram *et al.* showed that NE transport is stimulated by acute insulin treatments in SK-N-SH, a NB cell line.[104, 105] Additionally, Robertson *et al.* reported that NET regulation by insulin was shown to be dependent on Akt, where the inhibition or stimulation of Akt is capable of altering NET availability on the cell surface.[106] Another additional finding by the same group indicated that the inhibition of mTORC2 leads to NET upregulation *in vivo*.[107] These findings reveal that the regulation of members of the PI3K/Akt/mTOR pathways may be of particular interest to increase NET expression and consequently mIBG internalization. We showed in this study, for the first time, that the use of PI3K and/or mTOR inhibitors (CUDC-907, BGT226, VS-5584 and rapamycin) significantly increase mIBG internalization (Figure 40), without affecting cell viability in IGR-NB8 cells (Figure 41). In addition, BGT226 seems to mediate mIBG internalization via NET, as shown upon siRNA inhibition of NET expression, much like what was observed in the case of CUDC-907 treatment (Figure 39). These results indicate that it might be interesting to explore the PI3K/mTOR pathway to improve mIBG imaging and therapy in NB tumors. In the future, more studies regarding the effect of BGT226, VS-5584 and rapamycin on NET and DAT mRNA expression and protein levels will be done to further clarify how mIBG internalization is improved.

Vorinostat has very recently been shown to increase by 2.3 times the response rate in refractory or relapsed NB patients in a Phase II clinical trial when used as a radiosensitizer.[108] These

findings indicate the large potential of exploring HDACis' use to improve mIBG therapy *in vivo* and more importantly in high-risk NB patients, in whom the therapy used nowadays involves several rounds of very intensive therapies.[33] Therefore the need for more available drugs that could improve the outcome of therapy in high-risk NB patients is an urgent need. CUDC-907's therapeutic use has been extensively studied by other groups *in vivo* in xenograft models.[109, 110] Different treatments have been investigated for different types of tumors using CUDC-907 with varying concentrations and duration of treatment showing this inhibitor's varied antitumor potential.[99] The final part of this project consisted in the proof-of-concept experiment with CUDC-907's radiosensitizer effect *in vivo* in IGR-NB8 xenografts in mice. Basing our experimental design on the work of Mondello *et al.*, we performed 5 mg/kg and 10 mg/kg CUDC-907 treatments for 5 consecutive days with two extra days without treatment.[111] Following these experimental conditions, we observed an increase in tumoral ^{123}I-mIBG internalization after CUDC-907 treatment at 4 h p.i. (Table 5 and Figure 43). Additionally, when using either 5 or 10 mg/kg we observed no statistical differences, meaning that a lower dose of CUDC-907 could be used to produce the same results. We also observed a considerable accumulation in the gallbladder, the intestine and the adrenal glands, where we find more ^{123}I-mIBG than in the tumor tissue, our intended target. However, this increase is only temporary and might be explained by the physiological excretion pathway. Indeed at 24 h p.i. we observed a large decrease in the background accumulation of the tracer in most organs and a greater accumulation in the tumor compared to 4 h p.i. (Table 6 and Figure 44). The only healthy organ that still internalizes high amounts of ^{123}I-mIBG after 24 h is the adrenal gland. This issue has been shown by other groups where the adrenal glands are organs with high ^{123}I-mIBG internalization.[60, 112] This occurs since the adrenal tissue physiologically expresses large amounts of NET and therefore is susceptible to internalize mIBG.[55] Still, the increased ^{123}I-mIBG internalization in the tumor tissue in the presence of CUDC-907 shows very promising application for clinical trials, much like vorinostat as described above.[108]

These results and the knowledge obtained in this work are very useful for facilitation of a more specific targeting with pharmacological agents to increase transporter expression and consequently therapy/imaging success rate in NB and PHEO tumors.

Part II

Publication

The noradrenergic profile of plasma metanephrine in neuroblastoma patients is reproduced in xenograft mice models and arise from PNMT downregulation

The early detection of tumors remains to this day one of the main issues in the diagnosis of NB.[59] The absence of cancer-specific symptoms, the lack of available NB biopsies, and the suboptimal sensitivity of the analysis of the common metabolites, HVA and VMA, has led to the search for more adequate biomarkers. The analysis of plasma free MNs and urine MNs has been shown to be much more specific and sensitive than HVA and VMA, being more easily correlated with positive NB diagnosis.[37, 113, 114] Unlike with PHEO, which has been thoroughly described before,[34, 115] the nature of CATs metabolism has not been fully explored in NB tumors and the low availability of biopsies for research aims has slowed progress in this field.

In this project, we aimed to establish, characterize and validate a novel murine NB xenograft models which could be used to improve our understanding of CATs metabolism in NB.

We developed patient-derived xenografts (PDX) from NB cells obtained from either a primary tumor (NB1-T) or from bone marrow of NB patients (from patients NB11, NB13 and NB14). Histologically, the PDX tumors displayed a human primary phenotype with similar genomic profiles as the primary tumors from which they originated. Then, the total plasma MNs levels were evaluated, and we measured free and conjugated MNs (sulfonated and glucuronidated), since the conjugation of MNs is very important in CAT and MNs inactivation and clearance.[116] The comparison of the MNs' concentration in plasma between NB patients and the novel PDX models showed that murine MNs profile is mostly glucuronidated whereas the human MNs profile is mostly sulfonated.

We then explored the similarities between NB patients and our murine NB-PDX models by measuring plasma MNs concentration and profile, considering that NB are characterized by greater amounts of plasma MT and NMN. As seen in NB patients, the murine models showed great levels of the two metabolites compared with healthy mice. Additionally, MN levels was much lower than MT and NMN in mice model, as it is observed in NB-affected patients.

Then the CAT and MNs intratumoral levels were compared between PDX mice and NB patients. We observed no significant differences between the two and also that intratumoral metabolite levels were low and close to the limit of quantification. In addition, when comparing to murine adrenal controls, we observed a preferential noradrenergic nature in the tumors, due to a great reduction of E and MN synthesis in NB tissue.

Finally, the main genes in CAT metabolism were studied in NB-PDX and NB samples by RT-qPCR. We observed a great reduction in PNMT, the enzyme responsible for the conversion of NE into E, which clarified the noradrenergic profile in plasma and NB tumor tissues.

In summary, these findings showed that these novel murine NB-PDX models are reliable tools for the study of CAT metabolism and possibly for the screening of drugs *in vivo*, reducing the need for NB biopsy samples from affected children.

Research Paper

The noradrenergic profile of plasma metanephrine in neuroblastoma patients is reproduced in xenograft mice models and arise from PNMT downregulation

Karim Abid[1], Maja Beck Popovic[2], Katia Balmas Bourloud[3], Jacqueline Schoumans[4], Joana Grand-Guillaume[1], Eric Grouzmann[1] and Annick Mühlethaler-Mottet[3]

[1]Catecholamine and Peptides Laboratory, Service of Clinical Pharmacology and Toxicology, Lausanne University Hospital and University of Lausanne, Switzerland

[2]Pediatric Hematology-Oncology Unit, Woman-Mother-Child Department, Lausanne University Hospital and University of Lausanne, Switzerland

[3]Pediatric Hematology-Oncology Research Laboratory, Woman-Mother-Child Department, Lausanne University Hospital and University of Lausanne, Switzerland

[4]Oncogenomics Laboratory, Hematology Service, Laboratory Medicine and Pathology Department, Lausanne University Hospital and University of Lausanne, Switzerland

Correspondence to: *Annick Mühlethaler-Mottet, **email**: Annick.Muhlethaler@chuv.ch*
*Karim Abid, **email**: Karim-Alexandre.Abid@chuv.ch*

ABSTRACT

Metanephrines (MNs; normetanephrine (NMN), metanephrine (MN) and methoxytyramine (MT)) detected in urine or plasma represent the best biomarker for neuroblastoma (NB) diagnosis, however the metabolism of both catecholamine (CAT) and MNs remains enigmatic in NB. Using patient-derived xenograft (PDX) models derived from primary NB cells, we observed that the plasma levels of MNs in NB-PDX-bearing mice were comparable as in patients. Interestingly, murine plasma displayed an elevated fraction of glucuronidated forms of MNs relative to human plasma where sulfonated forms prevail. In tumors, the concentration ranges of MNs and CAT and the expression levels of the main genes involved in catecholamine metabolism were similar between NB-PDX and human NB tissues. Likewise, plasma and intratumoral profiles of individual MNs, with increased levels of MT and NMN relative to MN, were also conserved in mouse models as in patients. We further demonstrated the downregulation of the Phenylethanolamine N-Methyltransferase gene in NB biopsies and in NB-PDX explaining this biochemical phenotype, and giving a rational to the low levels of epinephrine and MN measured in NB affected patients. Thus, our subcutaneous murine NB-PDX models not only reproduce the phenotype of primary NB tumors, but also the metabolism of catecholamine as observed in patients. This may potentially open new avenues in preclinical studies for the follow up of novel therapeutic options for NB through the quantification of plasma MNs.

INTRODUCTION

NB is an embryonic tumor of the sympathetic nervous system, that can arise at any site of the sympathetic chain but most frequently in the abdominal region [1, 2]. NB represents approximately 5% of all childhood malignancies, but accounts for 12% of childhood cancer-related mortality [3]. Metastases frequently occur in NB

with an incidence of around 70% of cases [4] and 50 to 60% of high-risk NB will display relapse [2].

Catecholamine (CAT; E: epinephrine, NE: norepinephrine and DA: dopamine) production takes mainly place in adrenal chromaffin cells and sympathetic nerves. CAT are synthesized from L-tyrosine, which originates from diet and from hydroxylation of phenylalanine in the liver. L-tyrosine is transformed into dihydroxyphenylalanine

(DOPA) by the cytoplasmic enzyme tyrosine hydroxylase (TH). DOPA is then transformed in the cytoplasm into DA by the enzyme aromatic L-amino acid decarboxylase (AADC) [5]. In chromaffin cells, DA is internalized into neurosecretory vesicles by the vesicular monoamine transporters (VMAT1, and VMAT2, respectively SLC18A1 and SLC18A2) where it is converted into NE by dopamine beta-hydroxylase (DBH) and NE could be further converted into E in neurosecretory vesicles containing Phenylethanolamine N-Methyltransferase (PNMT) [5]. Following sympathetic stimulation, CAT stored in vesicles are exocyted in the blood stream to reach their target receptors and initiate the classically described "fight or flight response" [6]. A small proportion of CAT that leak from neurosecretory vesicles is transformed into metanephrines (MNs; normetanephrine (NMN), metanephrine (MN) and methoxytyramine (MT)) by the enzyme COMT (catechol O-methyltransferase) [5]. MNs diffuse freely across the membrane and are released in the bloodstream. A large amount of MNs is transformed through multiple steps involving other intermediate products into vanillylmandelic acid (VMA, from MN and NMN) and homovanillic acid (HVA from MT). These two end-stage are then filtered by kidneys to be secreted in urine [5, 7, 8]. Studies involving the enzymes responsible for CAT synthesis in NB compared with healthy adrenal medulla have been scarce, with the majority of studies focusing on pheochromocytoma and paraganglioma (PHEO/PGL) two other neuroendocrine tumors secreting MNs. CAT metabolism in PHEO/PGL has been extensively reviewed elsewhere [5, 8]. The large amount of CAT found in tumors and in plasma has been shown to be a consequence of the over-expression of several enzymes involved in CAT synthesis [9, 10].

The biological bases of CAT and MNs metabolism remain enigmatic in patients affected by NB. NMN and especially MT have recently been described as new biomarker of NB in plasma and urine [11, 12] with better sensibility and sensitivity compared with CAT and VMA and HVA, the classical metabolites used for NB screening in urine of suspected patient. High MNs concentration in plasma arise from a high synthesis of CAT [5, 8] and are suspected to directly arise from NB, as extensively described for PHEO/PGL. However, NB biopsy availability is a limitation, precluding large-scale molecular studies to decipher CAT metabolism in these tumors. In this study, we validated the use of murine NB patient-derived xenografts (PDX) as a pertinent model to mimic NB from patients and we demonstrated that the noradrenergic phenotype of NB is due to PNMT downregulation.

RESULTS

Murine MNs are mainly found as glucuro conjugates forms

In this study, we used PDX derived from seven high-risk stage M NB patients (Table 1). Four NB-PDX models were previously published by our group [13]. In addition, we developed four novel NB-PDX models from either NB cells disseminated in the bone marrow (BM) (for three patients NB11, NB13, NB14) or from the primary tumor of the NB-1 patient (from which a NB-PDX derived from BM metastatic cells was previously described [13]) (Table 1). To validate our novel NB-PDX models, the histological phenotype and the genomic profiles of the xenografts were analyzed. H&E and IHC staining for Phox2b, TH, DBH, synaptophysin (SYP), and CD56 confirmed that our novel NB-PDX displayed a histological phenotype comparable to NB primary tumors and previously published NB-PDX (Supplementary Figure 1A). In addition, examination of genomic copy number alterations (CNA) by single-nucleotide polymorphism (SNP) array of the novel NB-PDX indicated that the overall genomic profile of segmental chromosomal alterations (SCA) was conserved between the primary tumor and the PDX generated from the corresponding patient, although several additional SCA were observed in 3 out of 4 PDX (Supplementary Table 1). These data indicated that genetically and phenotypically our NB-PDX mimic human NB and may represent relevant *in vivo* models for the study of CAT metabolism in NB.

We then investigated and compared the concentration of MNs in the plasma of NB patients and NB-PDX-bearing mice. We first measured the amounts of free, sulfonated and glucuronidated forms of plasma MNs as conjugation (sulfonation or glucuronidation) represents a major pathway for CAT and MNs inactivation and besides enabling renal clearance [14]. We observed in patients with NB ($n = 22$) a large proportion of sulfonated MNs compared with free and glucuronidated forms (Figure 1A), corresponding respectively to 94.1%, 4.4% and 1.5% of total MNs (sum of free, sulfonated and glucuronidated forms) (Figure 1B). This contrasts with MNs in murine plasma ($n = 5$) where MNs are found in majority as glucuronidated forms (Figure 1A), representing 81.5% of total MNs, while free MNs forms were less abundant (16.2%), and an even smaller proportion of sulfonated forms 2.3% was detected (Figure 1B). Considering the large differences in sulfonation and glucuronation, we thereafter quantified plasma total MNs in mice as the sum of free, sulfonated and glucuronidated forms. For the human samples, as plasma MNs concentrations described in this study for controls represent clinical values which lack measurement of glucuronidated forms of MNs, glucuronidated forms of MNs showed in Figure 1 were subsequently omitted for NB patients to ensure relevant comparisons of total MN, NMN and MT levels between patients and controls. This has however no impact as glucuronidated forms represent only 1.5% of total MNs in plasma. It is noteworthy that quantification of MNs in tissue represents free forms since no conjugated forms are produced within tumor tissues or control adrenal glands as described in PHEO/PGL ([5] and from our own observation during MNs quantification in NB tumors from patients and NB-PDX).

Table 1: Clinical and biologic characteristics of NB samples and indication of the analyses carried out for each NB-PDX in this study

Patient	Sex	Age at diagnosis	Risk group	Stage	MYCN status	Name	Source	IHC	genomic profile	CAT/MNs plasma	CAT/MNs tumor	mRNA for CAT genes	prot PNMT
		Primary tumors				**NB-PDX**			**Analyses performed with NB-PDX**				
NB1*	M	10 mo	HR	M	no amp	NB1-T-1	primary tumor	yes	yes	yes	yes	yes	yes
						NB1-BM-5	BM (diagn)*	yes	n.d.	n.d.**	yes	yes	n.d.
NB2*	F	44 mo	HR	M	no amp	NB2-BM-4	BM (diagn)*	yes	n.d.	n.d.**	yes	yes	n.d.
NB4*	M	143 mo	HR	M	no amp	NB4-BM-8	BM (relapse)*	yes	n.d.	yes	yes	n.d.	yes
NB5*	M	24 mo	HR	M	amp	NB5-BM-1	BM (diagn)*	yes	n.d.	n.d.**	yes	yes	n.d.
NB11	M	28 mo	HR	M	amp	NB11-BM-1	BM (diagn)	yes	yes	yes	yes	yes	yes
NB13	M	33 mo	HR	M	amp	NB13-BM-1	BM (diagn)	yes	yes	yes	yes	yes	yes
NB14	F	48 mo	HR	M	amp	NB14-BM-1	BM (diagn)	yes	yes	yes	yes	yes	yes

NB1 to NB14 correspond to NB patients. T, tumor; BM, bone marrow; F, female; M, male; mo, month; HR, high–risk group; amp, amplified MYCN locus; no amp, no amplification of MYCN locus, n.d., not done. NB cells were isolated from primary tumor (-T) or bone marrow aspirations (-BM) and cultured *in vitro* for few passages before subcutaneous injection into athymic Swiss nude mice. The number of *in vivo* passages in PDX are indicated at the end of the PDX name. *Published in [13]; **CAT/MNs evaluation in plasma not performed, as the plasma were not collected from these mouse models at the time at which we sacrificed the mice for the study described in [13].

MT and NMN represent NB biomarkers in the plasma of NB-PDX-bearing mice similarly to NB patients

Then we assessed whether our NB-PDX models were mimicking NB in patients regarding MNs concentration and profile in plasma. To note CAT (DA, NE and E in the order of synthesis) are transformed by COMT into MT, NMN and MN, respectively (Figure 2A) and NB are characterized by an elevated amount of MT and NMN in plasma and urine [5, 15]. As observed in patients affected by a NB compared to healthy human subject, MT and NMN plasma concentrations in PDX mice were significantly increased compared with healthy mice (geo. mean at 161.9 nmol/l vs 63.2 nmol/l and 55.4 nmol/l vs 29.1 nmol/l respectively, *$p = 0.0317$ for both comparison) (Figure 2B, left panel). As expected, MN concentration was not significantly different between NB-PDX-bearing mice and controls (7.1 nmol/l vs 10.6 nmol/l) (Figure 2B, left panel). Even though plasma CAT concentration does not represent a reliable biomarker for the presence of a NB, DA is clearly increased in PDX mice compared with control (8.4 nmol/l vs 2.6 nmol/l, but without reaching significance threshold $p = 0.07$), whereas no significant differences for E (14.8 nmol/l vs 17.2 nmol/l) were measured; however a trend was also observed for NE: 56.7 nmol/l vs 37.3 nmol/l $p = 0.2$ (Figure 2B, right panel). This is in agreement with CAT levels quantified in patients (Figure 2B, right panel). Interestingly, a deeper analysis of the plasma MNs profile in human and mice revealed that MN level is very low compared to MT and NMN both in NB patients (geo mean 4.83 nmol/l vs 42.14 and 127.9 and nmol/l, respectively) and NB-PDX-bearing mice (geo mean 7.05 nmol/l vs 160.8 and 54.30 nmol/l, respectively) (Figure 2C). This is consistent with the fact that both MT and NMN represent biomarkers of NB in both urine and plasma [11, 12].

NB-PDX and human primary NB displayed no differences for CAT and MNs tissue concentration

The intratumoral levels of CAT and MNs were then quantified in NB-PDX and NB biopsies (indicated in Table 1 and in Supplementary Table 2). Metabolites levels were present in low amounts in most of the tissues tested with concentrations close to the limit of quantification (0.01 nmol/g of tissue) for several samples and particularly for MN in NB-PDX. We detected comparable levels of each metabolite between both tumor groups without significant differences (Figure 3A), except for MN levels (geo mean at 0.02 and 0.01 nmol/g for respectively NB and NB-PDX for which most of the values were close or under the limit of quantification). We then compared MNs and CAT intratumoral profiles of NB primary tumors and NB-PDX relative to murine adrenal controls, as human adrenal samples were not available for this analysis. In the adrenal glands, the major forms of metabolites are E, NE, MN and NMN, while DA the early product of catecholamine metabolite synthesis and MT represent minor forms (Figure 3B). Interestingly, a profile distinct from the adrenal controls was observed in NB and in NB-PDX tumors, as weaker amounts of intratumoral E and MN were detected relative to NE and NMN (geo mean in nmol/g: E: 0.12 and MN: 0.02 vs NE: 3.63 and NMN: 0.21 for NB; and E: 0.19 and MN: 0.01 vs NE: 1.23 and NMN: 0.15 for NB-PDX) (Figure 3B). We refer to this profile as noradrenergic since E and MN synthesis are strongly reduced in NB tissues. This is consistent with the plasma MNs profile observed in the plasma of patients and mice (Figure 2C).

The noradrenergic phenotype of NB results from the downregulation of PNMT expression in NB

To validate further our murine NB-PDX models, we analyzed the expression levels of the main genes involved in catecholamine metabolism by real-time qPCR in NB-PDX and NB biopsies (indicated in Table 1 and Supplementary Table 2). Similar mRNA expression levels of TH, DBH, AADC, PNMT, MAOA, VMAT1 and NET were observed between human primary NB and NB-PDX, although a reduction of COMT and VMAT2 expression was measured in NB-PDX biopsies (Figure 4A). Using the R2: Genomics Analysis and Vizualization Platform (http://r2.amc.nl), we compared the expression levels of CAT genes between four datasets of NB primary tumors and a panel of adrenal glands (Supplementary Figure 2). TH was not significantly different between the two tissues, conversely to a strong upregulation for DBH, AADC, MAOA, VMAT2 and NET ($p < 0.0001$ for all comparison) in NB compared to adrenal glands (Supplementary Figure 2). On the other hand, COMT was downregulated in NB ($p < 0.0001$) without significant impact, considering that MNs are massively produced in the tumor (Supplementary Figure 2). In addition, PNMT, the enzyme that converts NE into E, was extensively downregulated in NB compared to normal tissue ($p < 0.0001$) (Supplementary Figure 2). This explains the noradrenergic profile observed in plasma and in NB tumor tissues.

PNMT protein expression was shown to be downregulated in NB cell lines [16]. Here we observed that PNMT mRNA expression level was detected at 3.7 to 73.6 fold lower level than other enzymes mRNA involved in catecholamine metabolism (Figure 4A). The scarce expression of PNMT compared with other CAT metabolism genes was confirmed by the analysis of the SEQC and Versteeg NB transcriptomic datasets [17, 18] using the R2 platform (Figure 4B). To confirm this data at the protein level, PNMT protein expression was analyzed in NB tissues from patients (Supplementary Table 2) and NB-PDX (Table 1) by immunoblotting. This revealed that PNMT protein was undetectable in the NB and NB-PDX tissues analyzed, as well as in one noradrenergic PHEO (P39, NE and E concentration in tissue: 14300 and 3 nmol/g respectively). As positive controls, PNMT was detected in an adrenergic PHEO (P53 with 737 and 901 nmol/g of NE and E) and in three samples of human adrenal medulla tissue containing chromaffin cells that produce PNMT (Figure 4C and 4D).

DISCUSSION

Studies on NB biopsies suffers from a lack of material due to the low number of patients that undergo surgery procedure before treatment with chemotherapies and the needs of biopsy materials for pathology and genetic work up. In this report, we established mice NB xenograft models and validated their relevancy for the study of CAT metabolism and MNs as biomarker for NB detection. For this study, we took advantage of 4 NB-PDX models previously published by our group [13]. In addition, we developed four novel NB-PDX from metastatic NB cells of three patients and from the primary tumor of the patient NB-1, from which we already published a PDX derived from metastatic bone marrow cells [13]. Tumors raised in mice displayed histological phenotype of human primary NB and similar
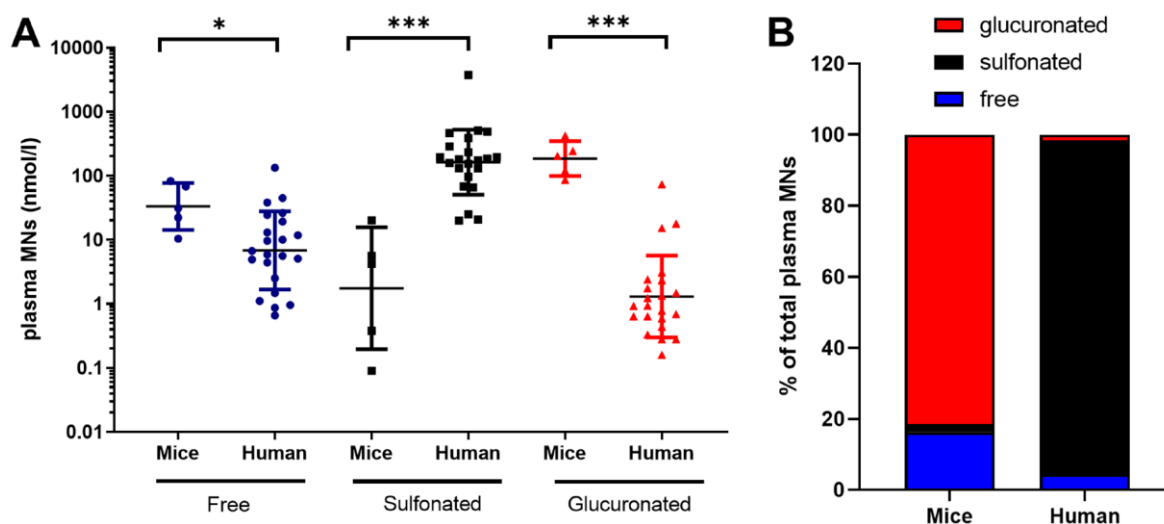
Figure 1: Free, sulfonated and glucuronidated forms of MNs (MT+NMN+MN) in plasma of mice with NB-PDX (n = 5) and NB patients (n = 22). (A) Values and geo mean ± geo SD are plotted on a logarithmic scale and analyzed with a non-parametric Mann Whitney test $^{***}p \leq 0.0001$, $^{*}p = 0.019$. Geo. mean in mice and human were respectively as follow: free MNs: 33.3 and 6.8 nmole/l, sulfonated MNs: 1.7 and 162.8 nmole/l, and glucuronidated MNs: 185.8 and 1.3 nmole/l; **(B)** The relative amount of free, sulfonated and glucuronidated forms of MNs shown in (a) were plotted in the graph as percent of total plasma MNs (MT+NMN+MN).

genomic profiles as their corresponding primary tumors. However, additional SCAs were identified in the NB-PDX, which may be explained by the fact that primary cells were cultivated for a short period *in vitro* before their subcutaneous injection in mice. In addition, the presence of chromosomal alterations differing from those identified in primary tumors were also described in disseminated NB cells in the bone marrow or using circulating tumoral DNA [19, 20].

The novelty of this study is the demonstration that NB-PDX are not only genetically and phenotypically similar to human primary NB, but they also recapitulated CAT metabolism observed in NB patients (Figure 5). Indeed, we demonstrated that the levels of plasma MNs of NB-PDX-bearing mice were increased as observed in NB affected patients compared to controls. In addition, intratumoral CAT and MNs were found in equivalent proportions in NB-PDX and in NB primary tumors. This may be explained by the fact that the expression levels of the main genes involved in CAT synthesis and metabolism were also equivalent, except for COMT and VMAT2/SLC18A2 genes, which displayed lower expression levels in NB-PDX. These genes encode for the protein responsible for MNs production from CAT and for the monoamine transporter that internalizes CAT

into neurosecretory vesicles in the cytoplasm, respectively. However, these differences are obviously of minor impact since MNs and CAT secretion profiles were conserved among the two types of tumors in both plasma and tumor biopsies.

Our data revealed that plasma MNs are mainly glucuronidated in mice, while sulfonation is a minor pathway, conversely to MNs in human plasma where sulfonation is by far the main process involved in MNs clearance in urine. Our observations are in accordance with a previous report describing in healthy rat a proportion of 63% of glucuronidated forms of NMN [21]. This implies that measurement of MNs in murine plasma requires a deconjugation step by glucuronidase to ensure a complete quantification (Figure 5).

Furthermore, we show in this report, that plasma and tumor tissues displayed a noradrenergic phenotype, as the synthesis of E and thus MN is limited in NB. This applies both in human and mouse NB models, reinforcing the validity of our NB-PDX models to mimic CAT metabolism found in patients. The noradrenergic catecholamine profile observed in NB is associated with the downregulation of PNMT expression, the enzyme responsible for E synthesis. Indeed, a very low amount of PNMT mRNA was detected in primary NB tumors
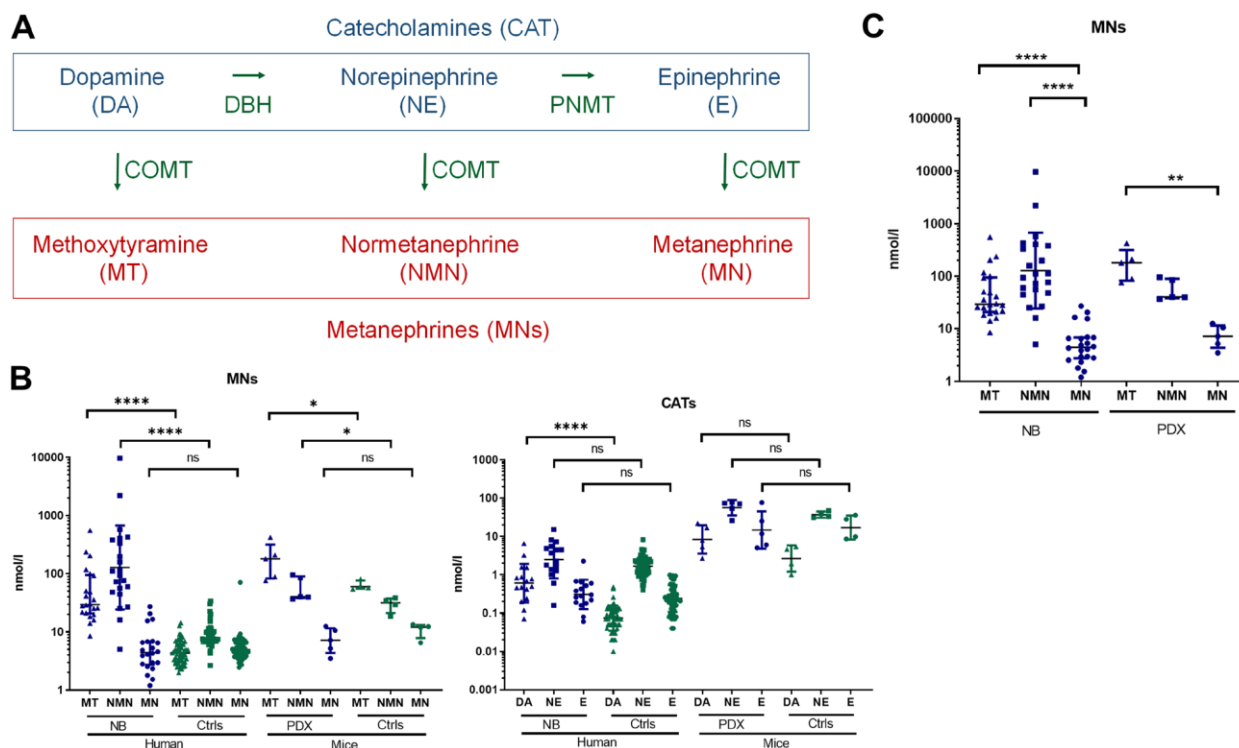
Figure 2: (**A**) Simplified scheme illustrating CAT and MNs metabolite biosynthesis. (**B**) Total plasma MNs (left panel) and CAT (right panel) in patients with NB ($n = 22$) compared with controls ($n = 55$) and in mice with NB-PDX ($n = 5$) compared with control mice ($n = 4$). Geo. mean for human samples in nmol/l for respectively MN, NMN and MT in NB patients: 4.83, 127.86 and 42.14; and for human controls: 5.17, 8.69 and 4.44. Mann Whitney test: $^{***}p \leq 0.0001$ for both NMN and MT (tumors compared with controls). PDX MNs levels are reported in the text, $^{*}p \leq 0.05$. (**C**) Illustration of total plasma MNs in patients NB ($n = 22$) and PDX NB mice ($n = 5$), value similar as in (B), to compare the relative amount each individual MNs. Kruskal-Wallis multiple comparison test: $^{****}p \leq 0.0001$, $^{**}p = 0.0027$.

and NB-PDX. Moreover, we demonstrated the lack of PNMT protein expression in NB tumor biopsies and in NB-PDX, as described only in NB cell lines in a previous report [16] (Figure 5). This is also in accordance with our former report showing that the downregulation of PNMT is responsible for the noradrenergic phenotype of a subset of PHEO compared with adrenergic PHEO [22]. In succinate dehydrogenase (SDH) and Von Hippel Lindau (VHL) related PHEO, PNMT mRNA downregulation has been demonstrated to arise from hypermethylation of the PNMT encoding gene [23, 24], similar mechanism may explain the noradrenergic phenotype of NB.

The limitations of this study are mainly due to the fact that our cohort of NB samples used for measurement of CAT and MNs in plasma, in tumor tissues and for the generation of NB-PDX are not overlapping. While NB biopsies used for intratumoral concentrations were

obtained from high-risk stage L2 and M NB, our murine NB models were derived only from patients with high-risk stage M NB, which represents metastatic tumors associated with unfavorable prognosis. This is because less aggressive NB cells are not tumorigenic in athymic Swiss nude mice, as observed from previous work from our laboratory [13]. In addition, the primary NB cells were cultivated for a low number of passages *in vitro* before xenotransplantation, and NB-PDX harbor several additional SCA alterations as compared to NB tumors derived from the corresponding patients, which may affect their phenotypic characteristics or biological properties. Moreover, these PDX models may not fully reflect the exact NB microenvironment, which would have been reproduced in a more appropriate manner though orthotopic injection into the adrenal glands and/or by using small fragments of NB primary tumors which contains the
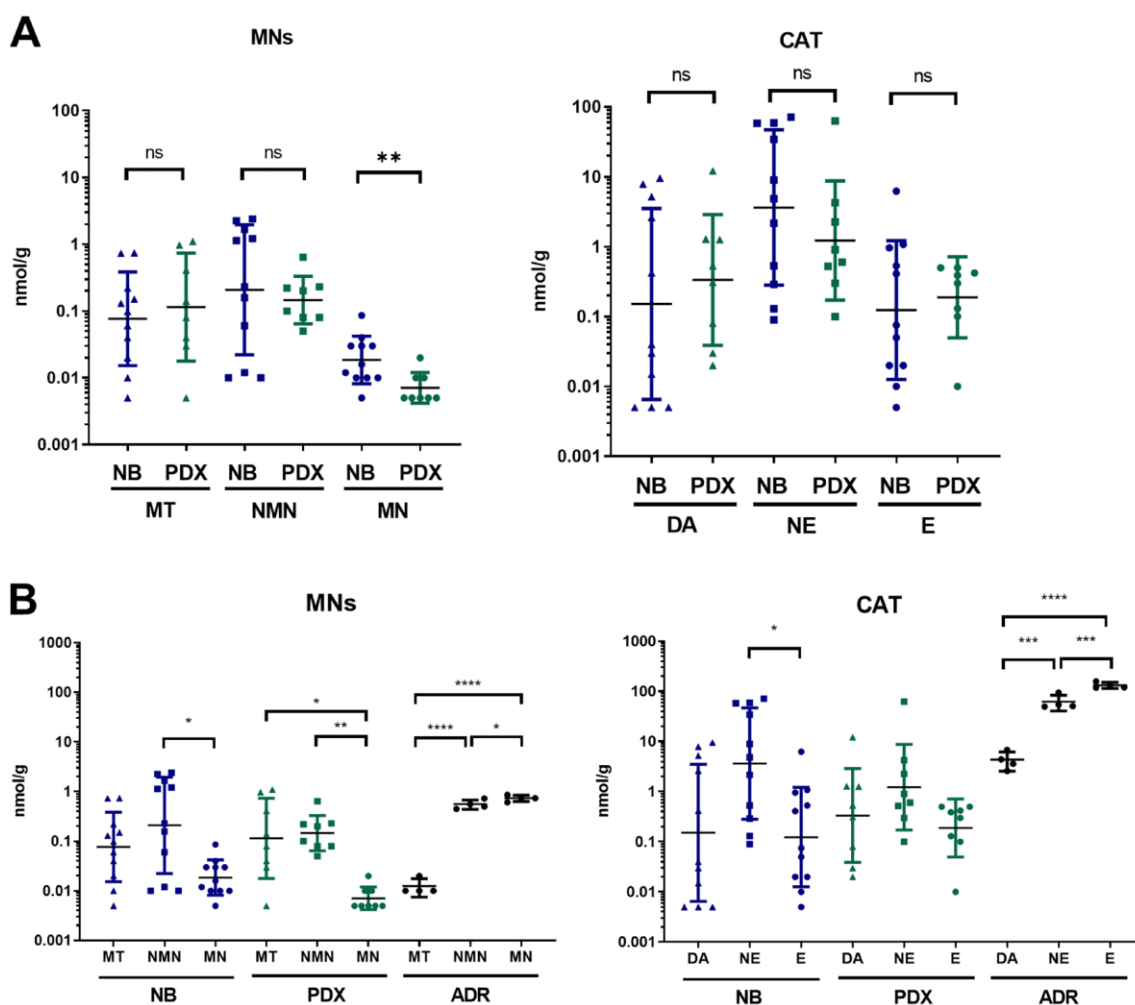
Figure 3: (**A**) Comparison of free MNs and CAT in tumor tissue of PDX mice ($n = 8$) and NB biopsy from patients ($n = 11$). Individual values (nmol/g) and geo mean ± geo SD are plotted on a logarithmic scale. Values under our limit of quantification were set at 0.005 nmol/g which represent half of the lower limit of quantification (LLOQ). Mann Whitney test: $^{**}p = 0.0078$; (**B**) Tissue concentration of free MNs and CAT in NB primary tumors ($n = 11$), NB-PDX ($n = 8$) compared with adrenal glands (ADR) of control mice ($n = 4$). Kruskal-Wallis multiple comparison test for NB and NB-PDX, Ordinary one-way ANOVA for ADR: $^{****}p \leq 0.0001$, $^{***}p \leq 0.0005$, $^{**}p \leq 0.005$, $^{*}p \leq 0.05$, ns comparison are not shown ($p > 0.05$).

additional stromal cells that represent key players in tumor progression [25–27]. However, despite these limitations, the NB-PDX models closely mimic the metabolism of catecholamine as observed in patients, regarding not only plasma levels of MNs, but also intratumoral CAT and MN concentrations, as well as mRNA expression levels of gene involved in CAT metabolism. Slight differences in gene expression were recorded for COMT and VMAT1, however without significant impact in terms of CAT and MNs production pattern. In addition, NB-PDX displayed a noradrenergic profile with reduced level of E and NM relative to NE and NMN, which was shown to correspond to the most frequent CAT profile in NB patients [16].

Plasma MNs quantification is on the rise to become the gold standard for NB diagnosis, since the test performance is better in terms of specificity and sensitivity than commonly used measurements of urinary CAT, VMA and HVA concentrations [11, 12, 28]. Plasma MNs level has been shown to correlate with tumor size in PHEO/PGL [29] and plasma MNs (totals forms) decrease within two days after PHEO/PGL resection [30]. Therefore, levels of MNs in mice models are also very likely to reflect the progression of tumor. Several models of NB in mice have been established [25, 27]. Apart from deciphering the molecular and genetic aspects of the tumors, as PNMT downregulation described in this report, NB preclinical models are also widely used

for the assessment of new treatment strategies [25, 27]. However, the evaluation of the effects of therapeutics is essentially based on the observation of the tumor's size through diverse monitoring methods (e.g., bioluminescence imaging, echography, micro-PET scan) requiring repeated anesthesia for a time-course follow-up. It would be interesting to evaluate if the measurement of plasma MNs may be relevant to monitor the therapeutic impact of drugs on NB-PDX models. Indeed, the low amount of plasma needed for MNs quantification by HPLC MS/MS (approx. 50 μl) is perfectly compatible with repeated blood collection in living mice without anesthesia. Thus, measuring plasma MNs at repeated time points (e.g., once a week) after the administration of drugs represents a less invasive method, which would allow implementing the principles of the 3Rs (Replacement, Reduction and Refinement) in animal experimentation.

To summarize, our NB-PDX model could represent a valuable tool for the study of catecholamine metabolism in NB and potentially for preclinical drug screening for NB therapy since previous studies have demonstrated a correlation between tumor size and metanephrine concentration. Blood testing of mice for metanephrine levels could therefore represent an option to monitor the growth of the tumors with limited impact on the animal welfare.
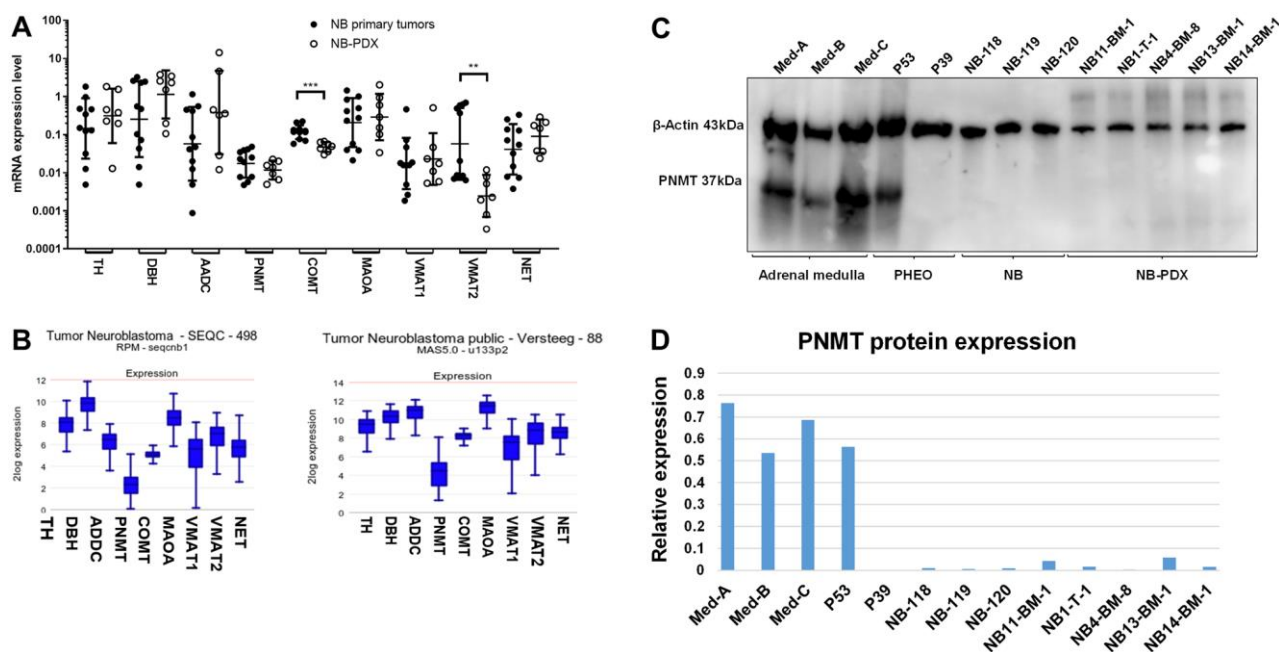
Figure 4: (**A**) mRNA expression levels of the main genes involved in CAT metabolism were analyzed by real-time qPCR in primary NB (n = 11) (black circles) and in NB-PDX (n = 7) (white circles). Data are plotted as mRNA expression level relative to the control genes TBP, GAPDH and EEIF1A1 with geo means ± geo SD (Mann Whitney test: COMT $p = 0.0003$, VMAT2 $p = 0.0041$, ns comparisons ($p > 0.05$) are not shown). qPCR analyses were performed in triplicats. (**B**) Illustration of the mRNA expression levels (normalized expression, in log2) of the indicated genes in two NB transcriptomic datasets analyzed by RNAseq (left) and microarrays (right). (**C**) Immunoblotting analysis of PNMT in representative tissues of three samples of adrenal gland tissue containing chromaffin cells, 2 PHEO, 3 NB and 5 NB-PDX. β-actin was used as loading control. (**D**) Densitometric quantification of immunoreactive band densities of Figure 4C using the Image J software (https://imagej.nih.gov/ij/download.html). The relative expression (PNMT/β-actin ratio) is plotted on the graph.

MATERIALS AND METHODS

NB, adrenal glands and PHEO/PGL tissues

PHEO/PGL samples were carefully chosen to be devoid of remaining healthy adrenal tissue by the surgeon or the pathologist. Similarly, healthy human adrenal glands were collected from the same procedure when healthy tissue was available and clearly distinct from the tumoral piece. The NB tumor material was collected from patients with stage L2 and M NB diagnosed at the Hemato-oncology Unit of the University Hospital of Lausanne (Switzerland) enrolled in the HR-NBL1 study from SIOPEN, after informed consent and in agreement with local institutional ethical regulations. This study was approved by the local ethics committee for the Canton de Vaud (Reference number: 2017-01865, 95/04 and 26/05). Of note the cohort of NB patients used for intratumoral CAT and MNs analyses and for the generation of NB-PDX are not overlapping.

NB primary cells were derived from high-risk stage M patients. Cells from the primary tumor of the NB1 patient were isolated as described [13]. Briefly, the tumor fragment was dissociated in a single-cell suspension by mechanical dissociation in phosphate-buffered saline containing 0.01 mg/ml collagenase II (Invitrogen, Carlsbad, CA, USA) and 0.1 mg/ml DNaseI (Roche Diagnostics, Basel, Switzerland) for 30 minutes at 37°C, followed by filtration through CellTricks (50 μm; Partek, Inc, St Louis, MO). NB primary cells derived from all other patients were isolated from involved BM. One volume (vol.) of BM was diluted with 3 vol. of Dubelco's modified Eagle's medium (D-MEM) (Life Technologies, Zug, Switzerland) and deposited on 2 vol. of Ficoll-Plaque Plus (GE Healthcare Europe) and centrifuged for 30 min at 1600 rpm. Then mononuclear cells were collected at the interphase, cells were washed twice in PBS and platted in neural basic medium (DMEM/F12 supplemented with penicillin/streptomycin, 2% B27 [Invitrogen], human recombinant basic fibroblast growth factor [FGF; 20 ng/ml; Peprotech, Rocky Hill, NJ], and EGF [20 ng/ml; Peprotech]). Once established, the purity of NB primary cells was then verified by performing anti-GD2 immunostaining. Primary NB cells NB1-T, NB1-BM and NB11-BM were also validated by IHC staining for Phox2b and SYP (Supplementary Figure 1B). The primary cells generated from the other patients were not evaluable by this method before implantation in mice.

NB xenografts

All *in vivo* procedures were performed under the guidelines of the Swiss Animal Protection Ordinance and the Animal Experimentation Ordinance of the Swiss Federal Veterinary Office (FVO). Animal experimentation protocols were approved by the Swiss FVO (authorization number: VD2995 and VD3372). All reasonable efforts were made to reduce suffering, including anesthesia for painful procedures.

All PDX were generated using NB cells isolated from either a primary tumor (NB1-T) or from bone marrow aspirations and maintained *in vitro* for a limited number
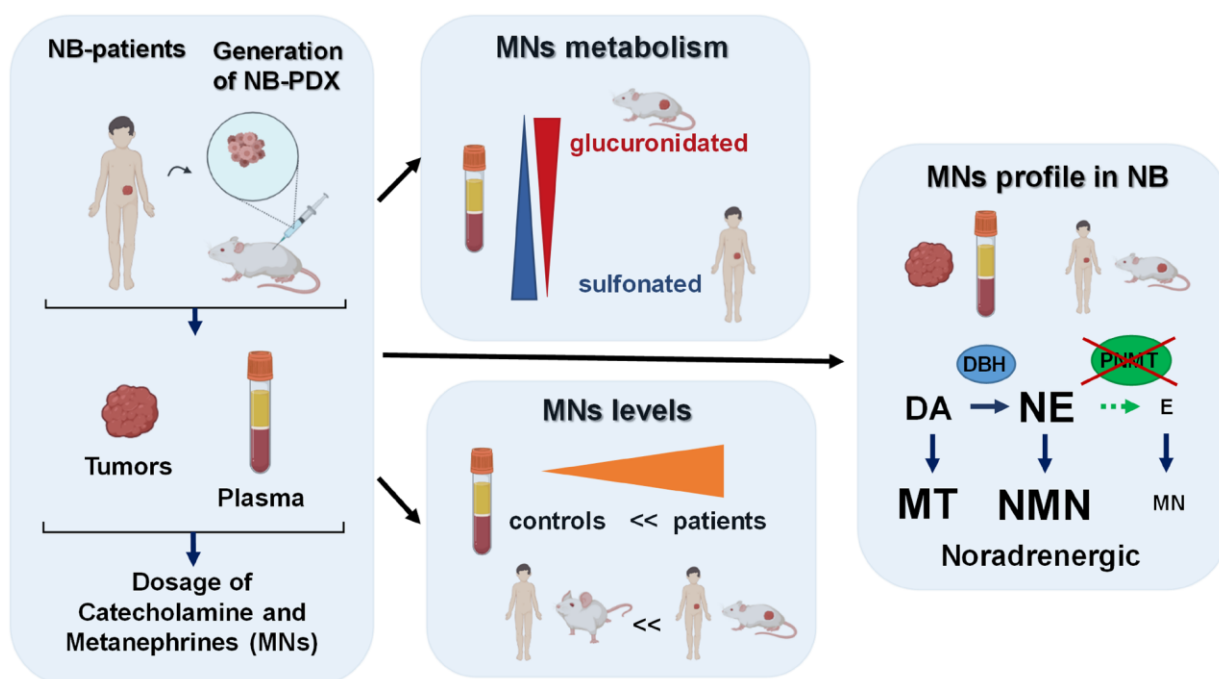
Figure 5: Graphical summary of our findings described in this report, as discussed in the results and discussion sections. This graphic was created using the software from Biorender (https://biorender.com/).

of passages (< 5). The only exception is the NB4-BM-8 PDX, which was generated from frozen cells dissociated from the seventh passage *in vivo* of the NB4-BM model (ie. NB4-BM-7). Primary NB cells (0.8×10^6 to 2×10^6) cells were suspended in 200 μl of Dulbecco modified Eagle medium DMEM (Invitrogen, Luzern, Switzerland) and BD Matrigel Basement Membrane matrix (1:1; BD Biosciences, San Diego, CA, USA) and implanted subcutaneously (s.c.) in the flanks of athymic Swiss nude mice (Charles River Laboratories, France). Tumor growth was followed up using calipers every 3 days. Mice were sacrificed once tumors reached a volume of approx. 900 mm3. NB-PDX were then maintained *in vivo* by serial subcutaneous transplantations. Tumor fragments were split into pieces for paraffin-embedded tissue formation, or collected in perchloric acid 0.1M for CAT and MNs quantification, or snap frozen in liquid nitrogen for protein or RNA extraction. NB xenograft fragments were also dissociated using the Tumor Dissociation kit Mouse (Miltenyi Biotec GmbH, Germany) according to manufacturer's instructions, followed by filtration through CellTricks (50 μm; Partek, Inc, St Louis, MO, USA) and dissociated cells were frozen in cryo-preservative medium (50% DMEM, 40% FCS and 10% DMSO).

Plasma collection

The control plasma were derived from 55 patients that were not affected by a NB, since the plasma MNs values were bellow upper reference limit. These patients were under 15 years of age, without previous MNs or CAT measurements request and none of them had MNs and CAT quantified ever since. For plasma from NB patients, a random set of 22 plasma was analyzed. The patients from which NB tissues were used to establish xenograft tumors (*n* = 7) were not part of this cohort of 22 patients. All blood samples were collected using a forearm venous cannula, with the patient kept supine for at least 15 min before sampling. Patients were instructed to fast and to abstain from caffeinated beverages for 24 hours before blood collection. All samples were collected onto ice and centrifuged within 30 min after puncture at 2500 g for 10 min at 4°C. Plasma was kept at −80°C until analysis. Total MNs and MT were desulfated using perchloric acid method or treated with sulfatase as described in a previous study [31]. Total and free MNs and MT were extracted on μElution plate and quantified by ultraperformance liquid chromatography-tandem mass spectrometry (UPLC-MS/MS) [32, 33]. The method used for free and total MNs quantification is identical after the deconjugation treatment applied to the sulfated MNs and MT [31].

For plasma collection from mice, immediately after mice sacrifice, blood was collected through heart puncture using 1 ml syringe (Omnifix-F, B.Braun, Melsungen, Germany) mounted with 25G5/8 needles (BD

Microlance™ 3, Becton Dickinson, France). Blood was transferred in EDTA collection tubes BD Microtainer® MAP (Becton Dickinson, USA). All samples were collected onto ice and centrifuged within 30 min after puncture at 2500 g for 10 min at 4°C. Plasma was kept at −80°C until analysis.

CAT and MNs quantification

Tumor tissues and murine adrenal glands were disrupted in perchloric acid 0.1M and were sonicated using a Branson Sonifier 450 (Branson, Danbury, CT, USA) at full power for 30 seconds. CAT from tissue or plasma were extracted using activated alumina in 0.5 ml microcentrifuge tubes and quantified by ultraperformance liquid chromatography-tandem mass spectrometry (UPLC-MS/MS) [34]. MNs were extracted in homogenized tumor tissue and plasma and quantified as previously published [32, 33].

Enzymatic hydrolysis of sulfates and glucuronides

Total MNs and MT were desulfated using perchloric acid method or treated with sulfatase as described in a previous study [31]. Glucuronides were removed enzymatically as follows: 10 μl of plasma samples were incubated with 90 μl of 10 mM ammonium acetate buffer pH 6.5 and 10 μl of beta-glucuronidase (Sigma-Aldrich, Buchs, Switzerland; previously dissolved in 2.5 M ammonium acetate buffer pH 5.5). Incubation time was 1 h at 37°C with agitation at 650 rpm. Samples were then diluted 2X in 10 mM ammonium acetate pH 6.5 and MNs were extracted as described above.

RNA extraction and real-time qPCR

RNA extraction was performed using Trizol (Invitrogen, Luzern, Switzerland) or RNAeasy kit with DNaseI treatment according to manufacturer's instructions (Qiagen, Hombrechtikon, Switzerland), and cDNA synthesis was performed using the PrimeScriptTM RT reagent Kit (Takara Bio Inc, Japan). Real time PCR assays were conducted in 384 wells using Sybergreen (Roche, Basel, Switzerland) with an Applied Biosystems 7900HT SDS (Thermo Fischer Scientific, Reinach, Switzerland). Negative controls were performed on the same amount of total RNA without adding the reverse transcriptase (NEC, no enzyme control). All primer pairs, chosen with the primer designing tool from the National Center for Biotechnology Information (NCBI) (Supplementary Table 3), were tested on a cDNA dilution series with efficiency comprised between 1.9 and 2.0. qPCR parameters were: 95°C 10 min, 40 cycles 95°C 15 sec. 60°C 1 min and melting curves were as expected in all cases. Normalization of gene expression was performed

on the three reference genes (RG) TBP, GAPDH and EEIF1A1 using the ΔCt method with Ct_RG = (Ct_TBP+Ct_GAPDH+Ct_EEIF1A1)/3 and mRNA expression level = $2^{-(Ct\_Gene-Ct\_RG)}$.

Immunoblotting

Adrenal glands remaining from PHEO surgery were used to obtain human adrenal medulla tissues. This was separated from the adrenal cortex using a scalpel by scraping off the brown interdigitated islets of chromaffin cells from adrenal glands. Tumor tissues and healthy parts of adrenal medulla were disrupted using a micro potter and lysed in a lysis buffer containing PBS with 0.5% triton X-100 and protease inhibitor (Complete™, Roche) to represent 20% w/v. Samples were then sonicated and clarified by a short centrifugation step of 2000 g for 30 seconds to discard the pellets. Samples were fractionated by SDS-PAGE under reducing conditions using precast gels (Bio-Rad, Reinach, Switzerland). Volumes loaded were 10 µl from a 20% wt/vol extract for biopsies and 5 µl from a 25 cm² plate of confluent cells lysed in 200 µl of lysis buffer. Proteins were electroblotted onto nitrocellulose membrane and probed with antibodies. Immunoreactive bands were revealed by chemiluminescence assay (PerkinElmer, Schwerzenbach, Switzerland). Anti-PNMT polyclonal antibody raised in rabbit was purchased from Abcam (Lucerna-Chem AG, Luzern, Switzerland, ab167427) and anti-β-actin monoclonal antibody (AC-15) was purchased from Sigma-Aldrich (Buchs, Switzerland). Secondary HRP conjugated anti-mouse and anti-rabbit antibodies were from Bio-Rad (cat. number 170-6516 and 170-6515, respectively). Quantification of PNMT and β-actin immunorevelation was performed using the Image J software from NIH, USA.

Immunohistochemistry and immunocytochemistry

The Hematoxylin and eosin (H&E) and immunohistochemistry (IHC) labeling were performed by the Lausanne Mouse Pathology Facility. IHC were performed on FFPE blocks of primary NB tumors, NB-PDX and cell pellets of the primary NB cells. IHC stainings were performed using anti-DBH Ab [9], anti-Phox2b (B11, # sc-376997, Santa Cruz Biotechnology, Dallas, USA), anti-TH (MAB318, MERCK KGaA, Darmstadt, Germany), and anti-SYP (NCL-L-SYPAP-299, Novocastra™, Leika Biosystems, Newcastle, UK) and polyclonal rabbit Ab anti-CD56/Ncam1 (14255-1-AP, Proteintech, USA).

For anti-GD2 immunocytochemistry, 200'000 cells were spin on cytospins with an Hettich (Hettich Zentrifugen, Tuttlingen, Germany) centrifuge at 700 rpm for 5 min. Slides were air-dried overnight, then fixed in 4% PBS-buffered paraformaldehyde for 10 min, washed in PBS, and incubated for 30 min at RT with monoclonal mouse anti-GD2 Ab (clone 7A4D8 [35]. After 3 washes in TBS 5 min., slides were incubated for 30 min at RT with rabbit anti-mouse antibody/AP (Dako, #D0314, Glostrup Denmark) diluted 1/30 in TBS, then with swine anti-rabbit Ig/AP (Dako, #D0306) diluted 1:20 in TBS for 30 min at RT, then with Fuchsin+ Substrate-Chromogene System (Dako, #K0625) for 10 min. After washing in running tape water for 5 min. slides were counterstained with hematoxylin (Sigma Aldrich, St Louis, MO, USA) and mounted with cover slip in buffered glycerine.

SNP array analysis

DNA was extracted from fresh or frozen NB (for NB-11, NB-13, and NB-14) and frozen NB-PDX tissues, with a tumor cell content superior to 50%, on a EZ1 advanced XL DNA extractor using DNA Tissue Kit (Qiagen Hombrechtikon, Switzerland) and quantified on a NanoDrop ND-2000 spectrophotometer (Thermo Fisher Scientific, Inc.; Waltham, MA, USA). SNP array analysis was performed using the Affymetrix CytoScan HD platform (Thermo Fisher Scientific, Inc.; Waltham, MA, USA) according to the manufacturer's protocol. Data analysis was performed using Chromosome analysis suite (ChAS) version 3.1.1.27 (r9436). CNA calling was performed by visual inspection.

Statistics

The measurement data were explored statistically and graphically using Prism (v. 8.0, GraphPad Software, Inc. La Jolla, CA, US). Non-parametric Mann Whitney test was used to compare two different conditions. Multiple comparisons were performed by one-way Anova or Kruskal-Wallis test depending on data distribution. Only comparisons with a p-value < 0.05 were considered as statistically significant.

Abbreviations

MNs: metanephrines; NMN: normetanephrine; MN: metanephrine; MT: methoxytyramine; NB: neuroblastoma; CAT: catecholamine; E: epinephrine; NE: norepinephrine; DA: dopamine; PDX: patient-derived xenograft; PNMT: phenylethanolamine N-methyltransferase; DOPA: dihydroxyphenylalanine; TH: tyrosine hydroxylase; AADC: aromatic L-amino acid decarboxylase; VMAT1, 2: vesicular monoamine transporters 1 and 2; DBH: dopamine beta-hydroxylase; COMT: catechol O-methyltransferase; VMA: vanillylmandelic acid; HVA: homovanillic acid; PHEO: pheochromocytoma; PGL: paraganglioma; H&E: hematoxylin and eosin; IHC: Immunohistochemistry; Phox2b: Paired-like homeobox 2b; SYP: synaptophysin; CNA: copy number alterations;

SNP: single-nucleotide polymorphism; SCA segmental chromosomal alterations; MAOA: monoamine oxidase A; NET: norepinephrine transporter; HR-NBL1: high risk neuroblastoma study 1; ChAS: chromosome analysis suite.

Author contributions

KA and JGG performed all major experimental work. KBB and AMM generated the NB-PDX models. JS performed the SNPa. AMM, KA, MBP, and EG designed the experiments, AMM and KA coordinated experiments, analyzed and interpreted the data, prepared figures and drafted the manuscript. MBP and EG edited the manuscript. EG provided laboratory resources and supervision. All authors have read and agreed to the published version of the manuscript.

CONFLICTS OF INTEREST

Authors have no conflicts of interest to declare.

REFERENCES

1. Maris JM. Recent Advances in Neuroblastoma. N Engl J Med. 2010; 362:2202–11. https://doi.org/10.1056/NEJMra0804577. [PubMed]

2. Colon NC, Chung DH. Neuroblastoma. Adv Pediatr. 2011; 58:297–311. https://doi.org/10.1016/j.yapd.2011.03.011. [PubMed]

3. Ritenour LE, Randall MP, Bosse KR, Diskin SJ. Genetic Susceptibility to Neuroblastoma: Current Knowledge and Future Directions. Cell Tissue Res. 2018; 372:287–307. https://doi.org/10.1007/s00441-018-2820-3. [PubMed]

4. Ara T, DeClerck YA. Mechanisms of Invasion and Metastasis in Human Neuroblastoma. Cancer Metastasis Rev. 2006; 25:645–57. https://doi.org/10.1007/s10555-006-9028-9. [PubMed]

5. Eisenhofer G, Kopin IJ, Goldstein DS. Catecholamine Metabolism: A Contemporary View with Implications for Physiology and Medicine. Pharmacol Rev. 2004; 56:331–49. https://doi.org/10.1124/pr.56.3.1. [PubMed]

6. Tank AW, Lee Wong D. Peripheral and Central Effects of Circulating Catecholamines. Compr Physiol. 2015; 5:1–15. https://doi.org/10.1002/cphy.c140007. [PubMed]

7. Trendelenburg U, Bönisch H, Graefe KH, Henseling M. The Rate Constants for the Efflux of Metabolites of Catecholamines and Phenethylamines. Pharmacological Reviews. 1979; 31:179–203. [PubMed]

8. Eisenhofer G, Lenders JW. Biochemical Diagnosis of Pheochromocytoma, a Rediscovered Catecholamine-Metabolizing Tumor. Clin Chem. 2018; 64:1780–81. https://doi.org/10.1373/clinchem.2018.290791. [PubMed]

9. Grouzmann E, Matter M, Bilz S, Herren A, Triponez F, Henzen C, Kim KS, Zulewski H, Buclin T, Brakch N, Abid K. Monoamine Oxidase a Down-Regulation Contributes to High Metanephrine Concentration in Pheochromocytoma. J Clin Endocrinol Metab. 2012; 97:2773–81. https://doi.org/10.1210/jc.2012-1557. [PubMed]

10. Lehnert H. Regulation of Catecholamine Synthesizing Enzyme Gene Expression in Human Pheochromocytoma. Eur J Endocrinol. 1998; 138:363–7. https://doi.org/10.1530/eje.0.1380363. [PubMed]

11. Franscini LC, Vazquez-Montes M, Buclin T, Perera R, Dunand M, Grouzmann E, Beck-Popovic M. Pediatric Reference Intervals for Plasma Free and Total Metanephrines Established with a Parametric Approach: Relevance to the Diagnosis of Neuroblastoma. Pediatr Blood Cancer. 2015; 62:587–93. https://doi.org/10.1002/pbc.25385. [PubMed]

12. Barco S, Verly I, Corrias MV, Sorrentino S, Conte M, Tripodi G, Tytgat G, van Kuilenburg A, van der Ham M, de Sain-van der Velden M, Garaventa A, Cangemi G. Plasma Free Metanephrines for Diagnosis of Neuroblastoma Patients. Clin Biochem. 2019; 66:57–62. https://doi.org/10.1016/j.clinbiochem.2019.02.012. [PubMed]

13. Coulon A, Flahaut M, Muhlethaler-Mottet A, Meier R, Liberman J, Balmas-Bourloud K, Nardou K, Yan P, Tercier S, Joseph JM, Sommer L, Gross N. Functional Sphere Profiling Reveals the Complexity of Neuroblastoma Tumor-Initiating Cell Model. Neoplasia. 2011; 13:991–1004. https://doi.org/10.1593/neo.11800. [PubMed]

14. Strott CA. Sulfonation and Molecular Action. Endocr Rev. 2002; 23:703–32. https://doi.org/10.1210/er.2001-0040. [PubMed]

15. Eisenhofer G, Siegert G, Kotzerke J, Bornstein SR, Pacak K. Current Progress and Future Challenges in the Biochemical Diagnosis and Treatment of Pheochromocytomas and Paragangliomas. Horm Metab Res. 2008; 40:329–37. https://doi.org/10.1055/s-2008-1073156. [PubMed]

16. Verly IR, Leen R, Meinsma JR, Hooijer GK, Savci-Heijink CD, van Nes J, Broekmans M, Wanders RJ, van Kuilenburg AB, Tytgat GA. Catecholamine Excretion Profiles Identify Clinical Subgroups of Neuroblastoma Patients. Eur J Cancer. 2019; 111:21–29. https://doi.org/10.1016/j.ejca.2019.01.014. [PubMed]

17. Molenaar JJ, Koster J, Zwijnenburg DA, van Sluis P, Valentijn LJ, van der Ploeg I, Hamdi M, van Nes J, Westerman BA, van Arkel J, Ebus ME, Haneveld F, Lakeman A, et al. Sequencing of Neuroblastoma Identifies

Chromothripsis and Defects in Neuritogenesis Genes. Nature. 2012; 483:589–93. https://doi.org/10.1038/nature10910. [PubMed]

18. Zhang W, Yu Y, Hertwig F, Thierry-Mieg J, Zhang W, Thierry-Mieg D, Wang J, Furlanello C, Devanarayan V, Cheng J, Deng Y, Hero B, Hong H, et al. Comparison of Rna-Seq and Microarray-Based Models for Clinical Endpoint Prediction. Genome Biol. 2015; 16:133. https://doi.org/10.1186/s13059-015-0694-1. [PubMed]

19. Abbasi MR, Rifatbegovic F, Brunner C, Mann G, Ziegler A, Potschger U, Crazzolara R, Ussowicz M, Benesch M, Ebetsberger-Dachs G, Chan GC, Jones N, Ladenstein R, et al. Impact of Disseminated Neuroblastoma Cells on the Identification of the Relapse-Seeding Clone. Clin Cancer Res. 2017; 23:4224–32. https://doi.org/10.1158/1078-0432.CCR-16-2082. [PubMed]

20. Chicard M, Boyault S, Colmet Daage L, Richer W, Gentien D, Pierron G, Lapouble E, Bellini A, Clement N, Iacono I, Brejon S, Carrere M, Reyes C, et al. Genomic Copy Number Profiling Using Circulating Free Tumor DNA Highlights Heterogeneity in Neuroblastoma. Clin Cancer Res. 2016; 22:5564–73. https://doi.org/10.1158/1078-0432.CCR-16-0500. [PubMed]

21. Yoneda S, Alexander N, Vlachakis ND. Conjugated Normetanephrine in Human and Rat Plasma and Erythrocytes. Biochemical Pharmacology. 1984; 33:2029–32. https://doi.org/https://doi.org/10.1016/0006-2952(84)90569-0. [PubMed]

22. Grouzmann E, Tschopp O, Triponez F, Matter M, Bilz S, Brandle M, Drechser T, Sigrist S, Zulewski H, Henzen C, Fischli S, Abid K. Catecholamine Metabolism in Paraganglioma and Pheochromocytoma: Similar Tumors in Different Sites? PLoS One. 2015; 10:e0125426. https://doi.org/10.1371/journal.pone.0125426. [PubMed]

23. Letouze E, Martinelli C, Loriot C, Burnichon N, Abermil N, Ottolenghi C, Janin M, Menara M, Nguyen AT, Benit P, Buffet A, Marcaillou C, Bertherat J, et al. Sdh Mutations Establish a Hypermethylator Phenotype in Paraganglioma. Cancer Cell. 2013; 23:739–52. https://doi.org/10.1016/j.ccr.2013.04.018. [PubMed]

24. Castro-Vega LJ, Letouze E, Burnichon N, Buffet A, Disderot PH, Khalifa E, Loriot C, Elarouci N, Morin A, Menara M, Lepoutre-Lussey C, Badoual C, Sibony M, et al. Multi-Omics Analysis Defines Core Genomic Alterations in Pheochromocytomas and Paragangliomas. Nat Commun. 2015; 6:6044. https://doi.org/10.1038/ncomms7044. [PubMed]

25. Braekeveldt N, Bexell D. Patient-Derived Xenografts as Preclinical Neuroblastoma Models. Cell Tissue Res. 2018; 372:233–43. https://doi.org/10.1007/s00441-017-2687-8. [PubMed]

26. Braekeveldt N, Wigerup C, Tadeo I, Beckman S, Sanden C, Jonsson J, Erjefalt JS, Berbegall AP, Borjesson A, Backman T, Ora I, Navarro S, Noguera R, et al. Neuroblastoma Patient-Derived Orthotopic Xenografts Reflect the Microenvironmental Hallmarks of Aggressive Patient Tumours. Cancer Lett. 2016; 375:384–89. https://doi.org/10.1016/j.canlet.2016.02.046. [PubMed]

27. Kamili A, Atkinson C, Trahair TN, Fletcher JI. Mouse Models of High-Risk Neuroblastoma. Cancer Metastasis Rev. 2020; 39:261–74. https://doi.org/10.1007/s10555-020-09855-0. [PubMed]

28. Peitzsch M, Mangelis A, Eisenhofer G, Huebner A. Age-Specific Pediatric Reference Intervals for Plasma Free Normetanephrine, Metanephrine, 3-Methoxytyramine and 3-O-Methyldopa: Particular Importance for Early Infancy. Clin Chim Acta. 2019; 494:100–05. https://doi.org/10.1016/j.cca.2019.03.1620. [PubMed]

29. Eisenhofer G, Lenders JW, Goldstein DS, Mannelli M, Csako G, Walther MM, Brouwers FM, Pacak K. Pheochromocytoma Catecholamine Phenotypes and Prediction of Tumor Size and Location by Use of Plasma Free Metanephrines. Clin Chem. 2005; 51:735–44. https://doi.org/10.1373/clinchem.2004.045484. [PubMed]

30. Grouzmann E, Fathi M, Gillet M, de Torrenté A, Cavadas C, Brunner H, Buclin T. Disappearance Rate of Catecholamines, Total Metanephrines, and Neuropeptide Y from the Plasma of Patients after Resection of Pheochromocytoma. Clin Chem. 2001; 47:1075–82. https://doi.org/10.1093/clinchem/47.6.1075. [PubMed]

31. Glauser M, Metrailler M, Gerber-Lemaire S, Centeno C, Seghezzi C, Dunand M, Abid K, Herren A, Grouzmann E. Enzyme and Acid Deconjugation of Plasma Sulfated Metanephrines. Clin Chim Acta. 2014; 430:125–8. https://doi.org/10.1016/j.cca.2013.12.044. [PubMed]

32. Dunand M, Donzelli M, Rickli A, Hysek CM, Liechti ME, Grouzmann E. Analytical Interference of 4-Hydroxy-3-Methoxymethamphetamine with the Measurement of Plasma Free Normetanephrine by Ultra-High Pressure Liquid Chromatography-Tandem Mass Spectrometry. Clin Biochem. 2014; 47:1121–3. https://doi.org/10.1016/j.clinbiochem.2014.04.003. [PubMed]

33. Peaston RT, Graham KS, Chambers E, van der Molen JC, Ball S. Performance of Plasma Free Metanephrines Measured by Liquid Chromatography-Tandem Mass Spectrometry in the Diagnosis of Pheochromocytoma. Clin Chim Acta. 2010; 411:546–52. https://doi.org/10.1016/j.cca.2010.01.012. [PubMed]

34. Dunand M, Gubian D, Stauffer M, Abid K, Grouzmann E. High-Throughput and Sensitive Quantitation of Plasma Catecholamines by Ultraperformance Liquid Chromatography-Tandem Mass Spectrometry Using a Solid Phase Microwell Extraction Plate. Anal Chem. 2013; 85:3539–44. https://doi.org/10.1021/ac4004584. [PubMed]

35. Gross N, Beck D, Portoukalian J, Favre S, Carrel S. New Anti-Gd2 Monoclonal Antibodies Produced from Gamma-Interferon-Treated Neuroblastoma Cells. Int J Cancer. 1989; 43:665–71. https://doi.org/10.1002/ijc.2910430421. [PubMed]

Bibliography

1.   Sung, H., et al., *Global Cancer Statistics 2020: GLOBOCAN Estimates of Incidence and Mortality Worldwide for 36 Cancers in 185 Countries.* CA Cancer J Clin, 2021. **71**(3): p. 209-249.

2.   Stratton, M.R., P.J. Campbell, and P.A. Futreal, *The cancer genome.* Nature, 2009. **458**(7239): p. 719-24.

3.   Hanahan, D. and R.A. Weinberg, *Hallmarks of cancer: the next generation.* Cell, 2011. **144**(5): p. 646-74.

4.   Patel, P. and K. Galoian, *Molecular challenges of neuroendocrine tumors.* Oncol Lett, 2018. **15**(3): p. 2715-2725.

5.   Bornstein, S.R., et al., *Chromaffin cells: the peripheral brain.* Mol Psychiatry, 2012. **17**(4): p. 354-8.

6.   Tank, A.W. and D. Lee Wong, *Peripheral and central effects of circulating catecholamines.* Compr Physiol, 2015. **5**(1): p. 1-15.

7.   Crona, J., D. Taieb, and K. Pacak, *New Perspectives on Pheochromocytoma and Paraganglioma: Toward a Molecular Classification.* Endocr Rev, 2017. **38**(6): p. 489-515.

8.   Pacak, K., G. Eisenhofer, and I. Ilias, *Diagnosis of pheochromocytoma with special emphasis on MEN2 syndrome.* Hormones (Athens), 2009. **8**(2): p. 111-6.

9.   Jimenez, C., W. Erwin, and B. Chasen, *Targeted Radionuclide Therapy for Patients with Metastatic Pheochromocytoma and Paraganglioma: From Low-Specific-Activity to High-Specific-Activity Iodine-131 Metaiodobenzylguanidine.* Cancers (Basel), 2019. **11**(7).

10.   Ajallé, R., et al., *Treatment of malignant pheochromocytoma.* Horm Metab Res, 2009. **41**(9): p. 687-96.

11.   Tsirlin, A., et al., *Pheochromocytoma: a review.* Maturitas, 2014. **77**(3): p. 229-38.

12.   Pacak, K., et al., *Recent advances in genetics, diagnosis, localization, and treatment of pheochromocytoma.* Annals of Internal Medicine, 2001. **134**(4): p. 315-329.

13.   Ajalle, R., et al., *Treatment of malignant pheochromocytoma.* Horm Metab Ress, 2009. **41**(9): p. 687-96.

14.   Martucci, V.L. and K. Pacak, *Pheochromocytoma and paraganglioma: diagnosis, genetics, management, and treatment.* Curr Probl Cancer, 2014. **38**(1): p. 7-41.

15.	Grouzmann, E., et al., *Catecholamine metabolism in paraganglioma and pheochromocytoma: similar tumors in different sites?* PLoS One, 2015. **10**(5): p. e0125426.

16.	Rednam, S.P., et al., *Von Hippel-Lindau and Hereditary Pheochromocytoma/Paraganglioma Syndromes: Clinical Features, Genetics, and Surveillance Recommendations in Childhood.* Clin Cancer Res, 2017. **23**(12): p. e68-e75.

17.	Opocher, G., et al., *Pheochromocytoma in von Hippel-Lindau disease and neurofibromatosis type 1.* Fam Cancer, 2005. **4**(1): p. 13-6.

18.	Rustin, P., A. Munnich, and A. Rotig, *Succinate dehydrogenase and human diseases: new insights into a well-known enzyme.* Eur J Hum Genet, 2002. **10**(5): p. 289-91.

19.	Kantorovich, V., K.S. King, and K. Pacak, *SDH-related pheochromocytoma and paraganglioma.* Best Pract Res Clin Endocrinol Metab, 2010. **24**(3): p. 415-24.

20.	Amodru, V., et al., *MEN2-related pheochromocytoma: current state of knowledge, specific characteristics in MEN2B, and perspectives.* Endocrine, 2020. **69**(3): p. 496-503.

21.	Fliedner, S.M., et al., *Hypoxia-Inducible Factor 2alpha Mutation-Related Paragangliomas Classify as Discrete Pseudohypoxic Subcluster.* Neoplasia, 2016. **18**(9): p. 567-76.

22.	Ritenour, L.E., et al., *Genetic susceptibility to neuroblastoma: current knowledge and future directions.* Cell Tissue Res, 2018. **372**(2): p. 287-307.

23.	Brodeur, G.M., *Spontaneous regression of neuroblastoma.* Cell Tissue Res, 2018. **372**(2): p. 277-286.

24.	Swift, C.C., et al., *Updates in Diagnosis, Management, and Treatment of Neuroblastoma.* Radiographics, 2018. **38**(2): p. 566-580.

25.	Huang, M. and W.A. Weiss, *Neuroblastoma and MYCN.* Cold Spring Harb Perspect Med, 2013. **3**(10): p. a014415.

26.	Tsubota, S. and K. Kadomatsu, *Origin and initiation mechanisms of neuroblastoma.* Cell Tissue Res, 2018. **372**(2): p. 211-221.

27.	Colon, N.C. and D.H. Chung, *Neuroblastoma.* Adv Pediatr, 2011. **58**(1): p. 297-311.

28.	Samim, A., et al., *Nuclear Medicine Imaging in Neuroblastoma: Current Status and New Developments.* J Pers Med, 2021. **11**(4).

29. Lee, E., et al., *Genomic profile of MYCN non-amplified neuroblastoma and potential for immunotherapeutic strategies in neuroblastoma.* BMC Med Genomics, 2020. **13**(1): p. 171.

30. Brodeur, G.M., et al., *International criteria for diagnosis, staging, and response to treatment in patients with neuroblastoma.* J Clin Oncol, 1988. **6**(12): p. 1874-81.

31. Pinto, N.R., et al., *Advances in Risk Classification and Treatment Strategies for Neuroblastoma.* J Clin Oncol, 2015. **33**(27): p. 3008-17.

32. Meany, H.J., *Non-High-Risk Neuroblastoma: Classification and Achievements in Therapy.* Children (Basel), 2019. **6**(1).

33. Smith, V. and J. Foster, *High-Risk Neuroblastoma Treatment Review.* Children (Basel), 2018. **5**(9).

34. Eisenhofer, G., I.J. Kopin, and D.S. Goldstein, *Catecholamine metabolism: a contemporary view with implications for physiology and medicine.* Pharmacol Rev, 2004. **56**(3): p. 331-49.

35. Kvetnansky, R., E.L. Sabban, and M. Palkovits, *Catecholaminergic systems in stress: structural and molecular genetic approaches.* Physiol Rev, 2009. **89**(2): p. 535-606.

36. Eisenhofer, G., et al., *Understanding Catecholamine Metabolism as a Guide to the Biochemical Diagnosis of Pheochromocytoma.* Reviews in Endocrine & Metabolic Disorders, 2001: p. 297-311.

37. Barco, S., et al., *Plasma free metanephrines for diagnosis of neuroblastoma patients.* Clin Biochem, 2019. **66**: p. 57-62.

38. Abid, K., et al., *The noradrenergic profile of plasma metanephrine in neuroblastoma patients is reproduced in xenograft mice models and arise from PNMT downregulation.* Oncotarget, 2021. **12**(1): p. 49-60.

39. Franscini, L.C., et al., *Pediatric reference intervals for plasma free and total metanephrines established with a parametric approach: relevance to the diagnosis of neuroblastoma.* Pediatr Blood Cancer, 2015. **62**(4): p. 587-93.

40. Cheng, M.H. and I. Bahar, *Monoamine transporters: structure, intrinsic dynamics and allosteric regulation.* Nat Struct Mol Biol, 2019. **26**(7): p. 545-556.

41. Aggarwal, S. and O.V. Mortensen, *Overview of Monoamine Transporters.* Curr Protoc Pharmacol, 2017. **79**: p. 12 16 1-12 16 17.

42. Benarroch, E.E., *Monoamine transporters: structure, regulation, and clinical implications.* Neurology, 2013. **81**(8): p. 761-8.

43. Duan, H. and J. Wang, *Selective transport of monoamine neurotransmitters by human plasma membrane monoamine transporter and organic cation transporter 3.* J Pharmacol Exp Ther, 2010. **335**(3): p. 743-53.

44. Courousse, T. and S. Gautron, *Role of organic cation transporters (OCTs) in the brain.* Pharmacol Ther, 2015. **146**: p. 94-103.

45. Zhou, J., *Norepinephrine transporter inhibitors and their therapeutic potential.* Drugs Future, 2004. **29**(12): p. 1235-1244.

46. Torres, G.E., R.R. Gainetdinov, and M.G. Caron, *Plasma membrane monoamine transporters: structure, regulation and function.* Nat Rev Neurosci, 2003. **4**(1): p. 13-25.

47. Kitayama, S. and T. Dohi, *Norepinephrine transporter splice variants and their interaction with substrates and blockers.* Eur J Pharmacol, 2003. **479**(1-3): p. 65-70.

48. Mandela, P. and G.A. Ordway, *The norepinephrine transporter and its regulation.* J Neurochem, 2006. **97**(2): p. 310-33.

49. Streby, K.A., et al., *Nothing but NET: a review of norepinephrine transporter expression and efficacy of 131I-mIBG therapy.* Pediatr Blood Cancer, 2015. **62**(1): p. 5-11.

50. Grouleff, J., et al., *Monoamine transporters: insights from molecular dynamics simulations.* Front Pharmacol, 2015. **6**: p. 235.

51. McHugh, P.C. and D.A. Buckley, *The structure and function of the dopamine transporter and its role in CNS diseases.* Vitam Horm, 2015. **98**: p. 339-69.

52. De Felice, L.J., *Chloride requirement for monoamine transporters.* Pflugers Arch, 2016. **468**(3): p. 503-11.

53. Henry, J.P., et al., *Biochemistry and molecular biology of the vesicular monoamine transporter from chromaffin granules.* J Exp Biol, 1994. **196**: p. 251-62.

54. Ciarimboli, G. and E. Schlatter, *Regulation of organic cation transport.* Pflugers Arch, 2005. **449**(5): p. 423-41.

55. Bayer, M., et al., *Uptake of mIBG and catecholamines in noradrenaline- and organic cation transporter-expressing cells: potential use of corticosterone for a preferred uptake in neuroblastoma- and pheochromocytoma cells.* Nucl Med Biol, 2009. **36**(3): p. 287-94.

56. Koepsell, H., K. Lips, and C. Volk, *Polyspecific organic cation transporters: structure, function, physiological roles, and biopharmaceutical implications.* Pharm Res, 2007. **24**(7): p. 1227-51.

57. Jonker, J.W. and A.H. Schinkel, *Pharmacological and physiological functions of the polyspecific organic cation transporters: OCT1, 2, and 3 (SLC22A1-3).* J Pharmacol Exp Ther, 2004. **308**(1): p. 2-9.

58. Wang, J., *The plasma membrane monoamine transporter (PMAT): Structure, function, and role in organic cation disposition.* Clin Pharmacol Ther, 2016. **100**(5): p. 489-499.

59. Desai, H., S. Borges-Neto, and T.Z. Wong, *Molecular Imaging and Therapy for Neuroendocrine Tumors.* Curr Treat Options Oncol, 2019. **20**(10): p. 78.

60. Rufini, V., M.L. Calcagni, and R.P. Baum, *Imaging of neuroendocrine tumors.* Semin Nucl Med, 2006. **36**(3): p. 228-47.

61. Olecki, E. and C.N. Grant, *MIBG in neuroblastoma diagnosis and treatment.* Semin Pediatr Surg, 2019. **28**(6): p. 150859.

62. Vallabhajosula, S. and A. Nikolopoulou, *Radioiodinated metaiodobenzylguanidine (MIBG): radiochemistry, biology, and pharmacology.* Semin Nucl Med, 2011. **41**(5): p. 324-33.

63. Rufini, V., et al., *The evolution in the use of MIBG scintigraphy in pheochromocytomas and paragangliomas.* Hormones (Athens), 2013. **12**(1): p. 58-68.

64. Agrawal, A., et al., *MIBG (metaiodobenzylguanidine) theranostics in pediatric and adult malignancies.* Br J Radiol, 2018. **91**(1091): p. 20180103.

65. Kayano, D. and S. Kinuya, *Current Consensus on I-131 MIBG Therapy.* Nucl Med Mol Imaging, 2018. **52**(4): p. 254-265.

66. Wiseman, G.A., et al., *Usefulness of 123I-MIBG scintigraphy in the evaluation of patients with known or suspected primary or metastatic pheochromocytoma or paraganglioma: results from a prospective multicenter trial.* J Nucl Med, 2009. **50**(9): p. 1448-54.

67. Kayano, D. and S. Kinuya, *Iodine-131 metaiodobenzylguanidine therapy for neuroblastoma: reports so far and future perspective.* ScientificWorldJournal, 2015. **2015**: p. 189135.

68. Ukon, N., et al., *Human dosimetry of free (211)At and meta-[(211)At]astatobenzylguanidine ((211)At-MABG) estimated using preclinical biodistribution from normal mice.* EJNMMI Phys, 2020. **7**(1): p. 58.

69. More, S.S., et al., *Vorinostat increases expression of functional norepinephrine transporter in neuroblastoma in vitro and in vivo model systems.* Clin Cancer Res, 2011. **17**(8): p. 2339-49.

70. Green, A.L., et al., *Epigenetic Regulation of Dopamine Transporter mRNA Expression in Human Neuroblastoma Cells.* Neurochem Res, 2015. **40**(7): p. 1372-8.

71. Mehnert, J.M. and W.K. Kelly, *Histone deacetylase inhibitors: biology and mechanism of action.* Cancer J, 2007. **13**(1): p. 23-9.

72. Kazantsev, A.G. and L.M. Thompson, *Therapeutic application of histone deacetylase inhibitors for central nervous system disorders.* Nat Rev Drug Discov, 2008. **7**(10): p. 854-68.

73. Kim, H.J. and S.C. Bae, *Histone deacetylase inhibitors: molecular mechanisms of action and clinical trials as anti-cancer drugs.* American Journal of Translational Research, 2011. **3**(2): p. 166-179.

74. Xu, W.S., R.B. Parmigiani, and P.A. Marks, *Histone deacetylase inhibitors: molecular mechanisms of action.* Oncogene, 2007. **26**(37): p. 5541-52.

75. Phimmachanh, M., et al., *Histone Deacetylases and Histone Deacetylase Inhibitors in Neuroblastoma.* Front Cell Dev Biol, 2020. **8**: p. 578770.

76. Dokmanovic, M., C. Clarke, and P.A. Marks, *Histone deacetylase inhibitors: overview and perspectives.* Mol Cancer Res, 2007. **5**(10): p. 981-9.

77. Green, A.L., et al., *Valproate increases dopamine transporter expression through histone acetylation and enhanced promoter binding of Nurr1.* Neuropharmacology, 2017. **125**: p. 189-196.

78. Martiniova, L., et al., *Increased uptake of [123I]meta-iodobenzylguanidine, [18F]fluorodopamine, and [3H]norepinephrine in mouse pheochromocytoma cells and tumors after treatment with the histone deacetylase inhibitors.* Endocr Relat Cancer, 2011. **18**(1): p. 143-57.

79. Gnyszka, A., Z. Jastrzebski, and S. Flis, *DNA Methyltransferase Inhibitors and Their Emerging Role in Epigenetic Therapy of Cancer.* Anticancer Research, 2013. **33**(8): p. 2989-2996.

80. Jin, B. and K.D. Robertson, *DNA methyltransferases, DNA damage repair, and cancer.* Adv Exp Med Biol, 2013. **754**: p. 3-29.

81. Taelman, V.F., et al., *Upregulation of Key Molecules for Targeted Imaging and Therapy.* J Nucl Med, 2016. **57**(11): p. 1805-1810.

82. Carnero, A., et al., *The PTEN/PI3K/AKT signalling pathway in cancer, therapeutic implications.* Curr Cancer Drug Targets, 2008. **8**(3): p. 187-98.

83. Rad, E., J.T. Murray, and A.R. Tee, *Oncogenic Signalling through Mechanistic Target of Rapamycin (mTOR): A Driver of Metabolic Transformation and Cancer Progression.* Cancers (Basel), 2018. **10**(1).

84. Chen, Y., et al., *VS-5584, a PI3K/mTOR dual inhibitor, exerts antitumor effects on neuroblastomas in vitro and in vivo.* J Pediatr Surg, 2020.

85. Dong, Y., et al., *Combination of Rapamycin and MK-2206 Induced Cell Death via Autophagy and Necroptosis in MYCN-Amplified Neuroblastoma Cell Lines.* Front Pharmacol, 2020. **11**: p. 31.

86. Lin, X., et al., *Rapamycin inhibits proliferation and induces autophagy in human neuroblastoma cells.* Biosci Rep, 2018. **38**(6).

87. Markman, B., et al., *Phase I safety, pharmacokinetic, and pharmacodynamic study of the oral phosphatidylinositol-3-kinase and mTOR inhibitor BGT226 in patients with advanced solid tumors.* Ann Oncol, 2012. **23**(9): p. 2399-2408.

88. Vassal, G., et al., *Therapeutic activity of CPT-11, a DNA-topoisomerase I inhibitor, against peripheral primitive neuroectodermal tumour and neuroblastoma xenografts.* Br J Cancer, 1996. **74**(4): p. 537-45.

89. Rao, X., et al., *An improvement of the 2^(–delta delta CT) method for quantitative real-time polymerase chain reaction data analysis.* Biostat Bioinforma Biomath, 2013. **3**(3): p. 71-85.

90. Glowniak, J.V., et al., *Evaluation of metaiodobenzylguanidine uptake by the norepinephrine, dopamine and serotonin transporters.* J Nucl Med, 1993. **34**(7): p. 1140-6.

91. Tolliver, B.K. and J.M. Carney, *Comparison of cocaine and GBR 12935: Effects of locomotor activity and stereotypy in two inbred mouse strains.* Pharmacology Biochemistry and Behavior, 1994. **48**(3): p. 733-739.

92. Croteau, N., J. Nuchtern, and M.P. LaQuaglia, *Management of Neuroblastoma in Pediatric Patients.* Surg Oncol Clin N Am, 2021. **30**(2): p. 291-304.

93. Bomanji, J., et al., *Uptake of iodine-123 MIBG by pheochromocytomas, paragangliomas, and neuroblastomas: a histopathological comparison.* J Nucl Med, 1987. **28**(6): p. 973-8.

94. van Berkel, A., et al., *Semiquantitative 123I-Metaiodobenzylguanidine Scintigraphy to Distinguish Pheochromocytoma and Paraganglioma from Physiologic Adrenal Uptake and Its Correlation with Genotype-Dependent Expression of Catecholamine Transporters.* J Nucl Med, 2015. **56**(6): p. 839-46.

95. **Eshleman, A.J.**, et al., *Characteristics of drug interactions with recombinant biogenic amine transporters expressed in the same cell type.* J Pharmacol Exp Ther, 1999. **289**(2): p. 877-885.

96. Wang, J., S.K. Michelhaugh, and M.J. Bannon, *Valproate robustly increases Sp transcription factor-mediated expression of the dopamine transporter gene within dopamine cells.* Eur J Neurosci, 2007. **25**(7): p. 1982-6.

97. Li, X., et al., *The HDAC and PI3K dual inhibitor CUDC-907 synergistically enhances the antileukemic activity of venetoclax in preclinical models of acute myeloid leukemia.* Haematologica, 2020.

98. Li, Z.J., et al., *CUDC-907 enhances TRAIL-induced apoptosis through upregulation of DR5 in breast cancer cells.* J Cell Commun Signal, 2020. **14**(4): p. 377-387.

99. Sun, K., et al., *Dual HDAC and PI3K Inhibitor CUDC-907 Downregulates MYC and Suppresses Growth of MYC-dependent Cancers.* Mol Cancer Ther, 2016. **16**(2): p. 285-299.

100. Clift-O'Grady, L., et al., *Biogenesis of synaptic vesicle-like structures in a pheochromocytoma cell line PC-12.* J Cell Biol, 1990. **110**(5): p. 1693-703.

101. Chung, H.W., et al., *131I-MIBG targeting of neuroblastoma cells is acutely enhanced by KCl stimulation through the calcium/calmodulin-dependent kinase pathway.* Cancer Biother Radiopharm, 2013. **28**(6): p. 488-93.

102. Kushner, B.H., et al., *A phase I/Ib trial targeting the Pi3k/Akt pathway using perifosine: Long-term progression-free survival of patients with resistant neuroblastoma.* Int J Cancer, 2017. **140**(2): p. 480-484.

103. Lee, M., et al., *Targeting PI3K/mTOR signaling exerts potent antitumor activity in pheochromocytoma in vivo.* Endocr Relat Cancer, 2017. **24**(1): p. 1-15.

104. Figlewicz, D.P., et al., *Insulin reduces norepinephrine transporter mRNA in vivo in rat locus coeruleus.* Brain Research, 1993. **602**(1): p. 161-164.

105. Apparsundaram, S., et al., *Trafficking-dependent and -independent pathways of neurotransmitter transporter regulation differentially involving p38 mitogen-activated protein kinase revealed in studies of insulin modulation of norepinephrine transport in SK-N-SH cells.* J Pharmacol Exp Ther, 2001. **299**(2): p. 666-77.

106. Robertson, S.D., et al., *Insulin Reveals Akt Signaling as a Novel Regulator of Norepinephrine Transporter Trafficking and Norepinephrine Homeostasis.* Journal of Neuroscience, 2010. **30**(34): p. 11305-11316.

107.	Siuta, M.A., et al., *Dysregulation of the norepinephrine transporter sustains cortical hypodopaminergia and schizophrenia-like behaviors in neuronal rictor null mice.* PLoS Biol, 2010. **8**(6): p. e1000393.

108.	DuBois, S.G., et al., *Randomized Phase II Trial of MIBG Versus MIBG, Vincristine, and Irinotecan Versus MIBG and Vorinostat for Patients With Relapsed or Refractory Neuroblastoma: A Report From NANT Consortium.* J Clin Oncol, 2021: p. JCO2100703.

109.	Hu, C., et al., *CUDC-907, a novel dual PI3K and HDAC inhibitor, in prostate cancer: Antitumour activity and molecular mechanism of action.* J Cell Mol Med, 2020. **24**(13): p. 7239-7253.

110.	Fu, X.-h., et al., *CUDC-907 displays potent antitumor activity against human pancreatic adenocarcinoma in vitro and in vivo through inhibition of HDAC6 to downregulate c-Myc expression.* Acta Pharmacologica Sinica, 2019. **40**(5): p. 677-688.

111.	Mondello, P., et al., *Dual inhibition of histone deacetylases and phosphoinositide 3-kinase enhances therapeutic activity against B cell lymphoma.* Oncotarget, 2017. **8**(8): p. 14017-14028.

112.	Kolby, L., et al., *Uptake of meta-iodobenzylguanidine in neuroendocrine tumours is mediated by vesicular monoamine transporters.* Br J Cancer, 2003. **89**(7): p. 1383-8.

113.	Weismann, D., et al., *Measurements of plasma metanephrines by immunoassay vs liquid chromatography with tandem mass spectrometry for diagnosis of pheochromocytoma.* Eur J Endocrinol, 2015. **172**(3): p. 251-60.

114.	Grouzmann, E. and F. Lamine, *Determination of catecholamines in plasma and urine.* Best Pract Res Clin Endocrinol Metab, 2013. **27**(5): p. 713-23.

115.	Eisenhofer, G. and J.W.M. Lenders, *Biochemical Diagnosis of Pheochromocytoma, a Rediscovered Catecholamine-Metabolizing Tumor.* Clin Chem, 2018. **64**(12): p. 1780-1781.

116.	Strott, C.A., *Sulfonation and molecular action.* Endocr Rev, 2002. **23**(5): p. 703-32.

Annexes

Annex 1

Table 7 – List of the different inhibitors used and respective references.

Inhibitors	Reference
ACY-1215	MedChem Express (HY-16026)
CUDC-101	Selleckchem (S1194)
CUDC-907	MedChem Express (HY-13522)
Entinostat	MedChem Express (HY-12163)
LMK-235	MedChem Express (HY-18998)
Mocetinostat	MedChem Express (HY-12164)
PCI-24781	MedChem Express (HY-10990)
Quisinostat	Selleckchem (S1096)
Romidepsin	MedChem Express (HY-15149)
Sodium-4-Penhylbutyrate	Sigma-Aldrich (567616)
Tacedinaline	Selleckchem (S2818)
Trichostatin A	Reagents Direct (62-K44)
Tubacin	MedChem Express (HY-13428)
Tucidinostat	MedChem Express (HY-109015)
Valproic acid	Sigma-Aldrich (676380)
Vorinostat	Sigma-Aldrich (SML0061)
BGT226	MedChem Express (HY-13334)
MK2206	MedChem Express (HY-108232)
VS-5584	MedChem Express (HY-16585)
Rapamycin	Sigma-Aldrich (553210)
DMI	Sigma-Aldrich (D3900)
GBR12935	Sigma-Aldrich (G9659)

HPLC-MS/MS method validation

Calibrants, QC Samples and internal standard

Two methods of mIBG extraction were performed: method A for higher levels of mIBG (used for HEK cells experiments) and method B for lower levels of mIBG (used for NB and PHEO cell lines). Calibrants and QC samples were prepared by serial dilutions of the 100 nM working concentration in DMSO. The stock solutions (1 mM) used to prepare the calibrants and QC samples were obtained from two different powders of mIBG and aliquots of 20 µL were stored at -80°C. Stock solutions were then diluted in DMSO to obtain the working solutions of 100 nM.

Two calibration curves were prepared: calibration A (for the method A) and calibration B (for the method B). Each calibration curve was composed of 8 calibrant samples (Table 8).

Table 8 – Calibration curve values for method A and method B.

Calibration A (nM)	Calibration B (nM)
0	0
0.02	0.005
0.1	0.02
0.4	0.1
1.6	0.4
6.4	1.6
25	6.4
100	25

The QC samples were prepared independently from calibrants, in DMSO. Three QC levels were prepared for method A and method B: QC high, QC medium and QC low (Table 9).

Table 9 – Quality control values for method A and method B.

QC	Method A (nM)	Method B (nM)
High	1.6	0.2
Medium	37.5	6.4
Lower	75	12.5

The internal standard stock solution (10 mM) was prepared in DMSO and working solution aliquots of 25 µL at 100 µM were stored at -80°C. For each extraction an internal standard were diluted at 2 nM in PBS tween.

Analytical Validation

To validate the method an intra- and inter-assay precision (Table 10) were performed.

Table 10 – Intra-assay precision using one single run of quintuplicates and inter-assay precision using five runs of triplicate per concentration level.

QC	Intra-assay precision, n=5 (CV%)	Inter-assay precision, n=5 (CV%)
High (12.5 nM)	1.1%	12.8%
Medium (6.3 nM)	6.6%	13.1%
Low (0.2 nM)	12.5%	12.7%